Spin Hall effects

Jairo Sinova

Institut für Physik, Johannes Gutenberg Universität Mainz, 55128 Mainz, Germany and Institute of Physics, Academy of Science of the Czech Republic, Cukrovarnická 10, 162 00 Praha 6, Czech Republic

Sergio O. Valenzuela

ICN2—Catalan Institute of Nanoscience and Nanotechnology, the Barcelona Institute of Science and Technology and CSIC, Campus UAB, Bellaterra, 08193 Barcelona, Spain, and ICREA—Institució Catalana de Recerca i Estudis Avançats, 08010 Barcelona, Spain

J. Wunderlich

Institute of Physics, Academy of Science of the Czech Republic, Cukrovarnická 10, 162 00 Praha 6, Czech Republic and Hitachi Cambridge Laboratory, Cambridge CB3 0HE, United Kingdom

C. H. Back

Universität Regensburg, Universitätstraße 31, 93040 Regensburg, Germany

T. Jungwirth

Institute of Physics, Academy of Science of the Czech Republic, Cukrovarnická 10, 162 00 Praha 6, Czech Republic and School of Physics and Astronomy, University of Nottingham, Nottingham NG7 2RD, United Kingdom

(published 27 October 2015)

Spin Hall effects are a collection of relativistic spin-orbit coupling phenomena in which electrical currents can generate transverse spin currents and vice versa. Despite being observed only a decade ago, these effects are already ubiquitous within spintronics, as standard spin-current generators and detectors. Here the theoretical and experimental results that have established this subfield of spintronics are reviewed. The focus is on the results that have converged to give us the current understanding of the phenomena, which has evolved from a qualitative to a more quantitative measurement of spin currents and their associated spin accumulation. Within the experimental framework, optical-, transport-, and magnetization-dynamics-based measurements are reviewed and linked to both phenomenological and microscopic theories of the effect. Within the theoretical framework, the basic mechanisms in both the extrinsic and intrinsic regimes are reviewed, which are linked to the mechanisms present in their closely related phenomenon in ferromagnets, the anomalous Hall effect. Also reviewed is the connection to the phenomenological treatment based on spin-diffusion equations applicable to certain regimes, as well as the spin-pumping theory of spin generation used in many measurements of the spin Hall angle. A further connection to the spin-current-generating spin Hall effect to the inverse spin galvanic effect is given, in which an electrical current induces a nonequilibrium spin polarization. This effect often accompanies the spin Hall effect since they share common microscopic origins. Both can exhibit the same symmetries when present in structures comprising ferromagnetic and nonmagnetic layers through their induced current-driven spin torques or induced voltages. Although a short chronological overview of the evolution of the spin Hall effect field and the resolution of some early controversies is given, the main body of this review is structured from a pedagogical point of view, focusing on well-established and accepted physics. In such a young field, there remains much to be understood and explored, hence some of the future challenges and opportunities of this rapidly evolving area of spintronics are outlined.

DOI: 10.1103/RevModPhys.87.1213 PACS numbers: 72.25.Ba, 75.76.+j, 72.25.Dc, 75.78.−n

CONTENTS

I. INTRODUCTION

Spintronics is a field that jointly utilizes the spin and charge degrees of freedom to control equilibrium and nonequilibrium properties of materials and devices (Wolf *et al.*, 2001; Zutic, Fabian, and Sarma, 2004; Bader and Parkin, 2010). The generation, manipulation, and detection of spin currents is one of the key aspects of the field of spintronics. Among the several possibilities to create and control spin currents, the spin Hall effect (SHE) has gained a distinct place since its first observation a decade ago (Kato *et al.*, 2004a; Wunderlich *et al.*, 2004; Day, 2005; Wunderlich *et al.*, 2005). In the direct SHE, an electrical current passing through a material can generate a transverse pure spin current polarized perpendicular to the plane defined by the charge and spin current. In its reciprocal effect, the inverse SHE (ISHE), a pure spin current through the material generates a transverse charge current. In both cases, the material must possess spin-orbit coupling.

The SHE borrows its concept from the well-established anomalous Hall effect (AHE), where relativistic spin-orbit coupling generates an asymmetric deflection of the charge carriers depending on their spin direction (Nagaosa *et al.*, 2010). The AHE can be detected electrically in a ferromagnet (FM) via a transverse voltage because of the difference in population of majority and minority carriers. The generalization of this effect to a pure spin current generated by the SHE in a nonmagnetic material (NM) was proposed over four decades ago (Dyakonov and Perel, 1971b) based on the idea of asymmetric Mott scattering (Mott, 1929). This so-called extrinsic SHE remained unexplored until recent proposals that put forward a similar prediction (Hirsch, 1999; Zhang, 2000) as well as the possibility of a strong intrinsic SHE (Murakami, Nagaosa, and Zhang, 2003; Sinova *et al.*, 2004).

The initial challenge for SHE detection was primarily the lack of direct electrical signals; therefore initial experiments detected it by optical means, in both the extrinsic regime (Kato *et al.*, 2004a) and the intrinsic regime (Wunderlich *et al.*, 2004, 2005). The ISHE was detected soon thereafter by Saitoh *et al.* (2006), Valenzuela and Tinkham (2006), and Zhao *et al.* (2006). Early measurements were mostly qualitative. However, more accurate quantitative measurements of spin Hall angles have been established in later experiments through the aid of FM detectors in static or dynamic magnetization regimes, and a much firmer situation has arisen in the field.

Adding to this flurry of activity and increased understanding, recent experiments in magnetic structures have aimed to use spin currents injected from an adjacent spin Hall NM for spin-transfer torque (STT) switching of a FM (Miron, Garello *et al.*, 2011; Liu, Pai, Li, *et al.*, 2012). In addition to this SHE-induced torque, there is also a spin-orbit torque (SOT) (Bernevig and Vafek, 2005; Chernyshov *et al.*, 2009), which is generated via the inverse spin galvanic effect (ISGE) (Belkov and Ganichev, 2008). In the ISGE, a charge current can generate a nonequilibrium uniform spin polarization via spin-orbit coupling and it is often a companion effect to the spin current generating SHE (Kato *et al.*, 2004a, 2004b; Wunderlich *et al.*, 2004, 2005). These results underscore the relevance of the SHE for applications.

As mentioned, the SHE borrows directly from the physics and mechanisms of the AHE and correspondingly much of their descriptions are parallel. The family of the AHE, SHE, and ISHE is illustrated in Fig. 1. The important caveat is that, unlike the AHE which correlates charge degrees of freedom via relativistic spin-orbit interaction, the SHE and ISHE correlate the charge degree of freedom, a conserved quantity, and the spin degree of freedom, a nonconserved quantity subject to decay and dephasing.

The aim of this review is to survey the rapid developments of the SHE field, to give an overview of its current experimental understanding, the basic theoretical tools that are being applied to describe it and their current level of success and limitations, the connection to important related phenomena, as well as the potential of the SHE for applications, particularly in the area of magnetization dynamics.

Given the enormous volume of work that has been published in just a decade, we can only highlight a selection

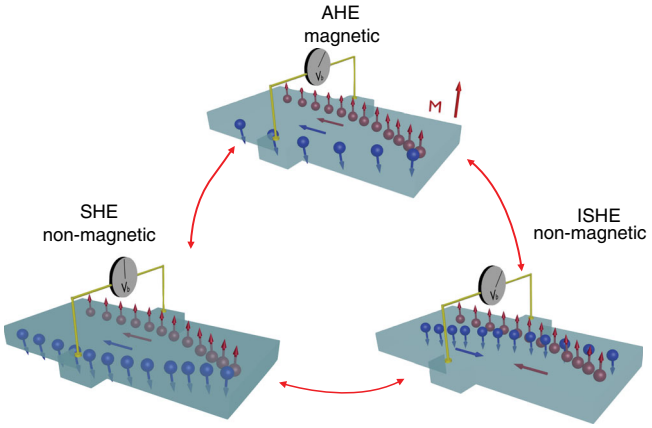

FIG. 1 (color online). An illustration of the connected family of the spin-dependent Hall effects. In the AHE, a charge current generates a polarized transverse charge current. In the SHE, an unpolarized charge current generates a transverse pure spin current. In the ISHE, a pure spin current generates a transverse charge current.

of reports that contributed significantly to the field. Our review covers most of the major aspects of the field. It surveys both metals and semiconductors, as well as optical, transport, and magnetization dynamics experiments. The theory survey covers most of the relevant microscopic and phenomenological modeling, as well as resolutions of earlier controversies.

The reader interested in this field should complement this reading with other recent reviews. Hoffmann (2013b) reviewed extensively the transport measurements in metallic systems. Other focused reviews published recently are Gradhand *et al.* (2012), Jungwirth, Wunderlich, and Olejník (2012), Maekawa and Takahashi (2012), Raimondi *et al.* (2012), Valenzuela and Kimura (2012).

II. OVERVIEW

In this section, we provide an overview that starts from the original seeds of the SHE field and connects afterwards to the broader context of the phenomenon within spintronics. The overview is organized as follows: First, we look back to how the Mott scattering of electron beams in vacuum and the skew scattering of electrons in FMs germinated into the prediction of the extrinsic SHE in NMs. Second, we discuss that in a solid-state system there is in addition an intrinsic spin-deflection, arising from the internal spin-orbit coupling forces in a perfect crystal. This key distinction from electrons in a vacuum makes the spin-dependent Hall physics in condensed matter systems much richer. We also note here the connection of this intrinsic mechanism to the quantum Hall effects. Third, we summarize studies of spin injection and detection in hybrid FM-NM structures, which were particularly impactful on the research of the SHE. Here, we highlight dc transport as well as ac ferromagnetic resonance (FMR) experiments. Finally, we connect the physics of the SHE, which considers pure spin currents and nonuniform spin accumulations, to the physics of the spin galvanic effects. The latter effects represent a seemingly distinct family of relativistic phenomena relating to the generation or detection of uniform nonequilibrium spin polarizations. However, as we point out, the spin Hall and spin galvanic effects can have common features in their microscopic physical origins and both can contribute to spin-charge conversion phenomena. These two relativistic effects are now at the forefront of current-induced magnetization dynamics research and both effects also contribute to the reciprocal conversion of magnetization dynamics into electrical signals.

A. Spin Hall, anomalous Hall, and Mott polarimetry

In their original work, Dyakonov and Perel (1971b) referred to the phenomena of Mott scattering (Mott, 1929) and of the AHE (Hall, 1881) to theoretically predict the extrinsic SHE. In particular, they pointed out the following: (i) spin-dependent asymmetric deflection is observed in electron beams in vacuum due to Mott scattering (Mott, 1929, 1932; Shull, Chase, and Myers, 1943; Gay and Dunning, 1992). (ii) Mott's skew scattering is regarded among the origins of the AHE of electron carriers in FMs (Karplus and Luttinger, 1954; Smit, 1955, 1958; Berger, 1970; Nagaosa *et al.*, 2010). The two points imply that under an applied electrical current, asymmetric spin-dependent deflection should occur in NMs. Unlike in FMs, NMs in equilibrium have the same number of spin-up and spin-down electrons and no transverse charge imbalance will occur. Instead, the SHE generates an edge spin accumulation that has opposite polarization at opposite edges.

We now explore the Mott scattering seed of the SHE in more detail. In 1925, the spin of the electron was inferred indirectly by atomic spectra (Uhlenbeck and Goudsmit, 1925). Based on the then recently derived Dirac equation (Dirac, 1928), Mott proposed his scattering experiment (Mott, 1929, 1932) to provide direct evidence that spin is an intrinsic property of a free electron. The ensuing quest for the experimental verification of Mott scattering (Shull, Chase, and Myers, 1943) was among the founding pillars of the entire relativistic quantum mechanics concept. Since Mott scattering of electron beams from heavy nuclei in a vacuum chamber can be regarded as the SHE in a non-solid-state environment, the seeds of the SHE date back to the very foundations of the electron spin and relativistic quantum mechanics.

Figure 2(a) shows the Mott (1929) double-scattering experiment proposal. First, an unpolarized beam of electrons is scattered from heavy nuclei in a target. Because of the relativistic spin-orbit coupling, large angle (~90°) scattering from the first target produces a polarized beam with the spin polarization transverse to the scattering plane. Scattering of these polarized electrons from the second target results, again due to the spin-orbit coupling, in a left-right scattering asymmetry that is proportional to the polarization induced by the first scattering.

In a complete analogy to the Mott double-scattering effect, but instead of vacuum now considering a solid-state system, Hankiewicz *et al.* (2004) proposed an H-bar microdevice schematically shown in Fig. 2(b). In the SHE part of the device, an unpolarized electrical current generates a transverse spin current due to an effective spin-orbit force F_{so} that acts on the carriers. The spin current injected into the second leg generates, via the ISHE, an electrical current, or in an open circuit geometry a voltage across the second leg. The first attempt to implement this H-bar SHE-ISHE experiment was carried out by Mihajlovic *et al.* (2009) in gold, but no signature of the spin

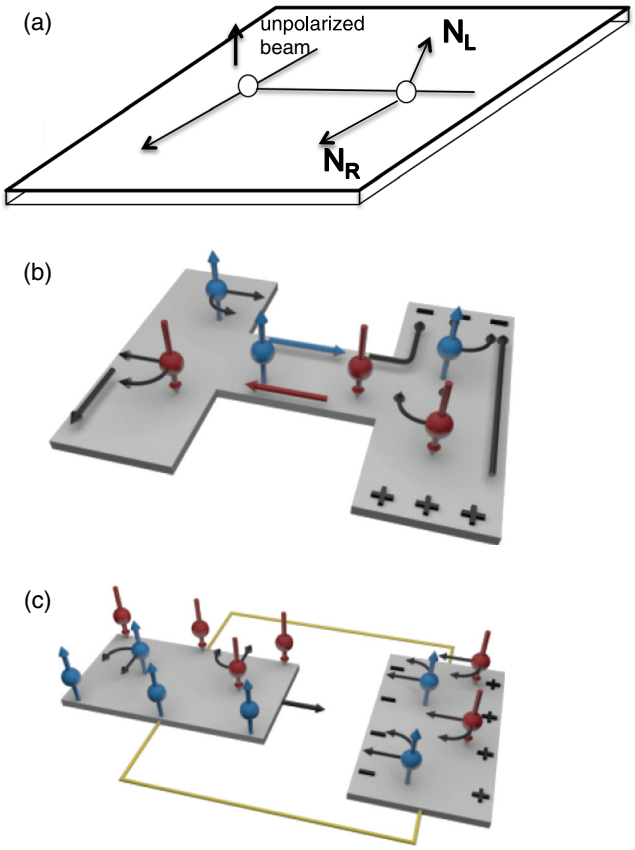

FIG. 2 (color online). (a) Schematics of the Mott (1929) original double-scattering proposal, (b) SHE-ISHE analog of Mott double scattering in Hankiewicz *et al.* (2004) H-bar device, (c) SHE (left) and ISHE (right) wired as proposed by Hirsch (1999). Instead of directly injecting a spin current generated in the SHE part of the experiment, as suggested by Mott and by Hankiewicz *et al.*, Hirsch considered that the pure spin current is generated from the opposite spin accumulations at the edges of the SHE part of the "double-scattering" device. The effective spin-orbit force that deflects the spins in the SHE-ISHE is represented by straight black arrows acting on the carriers. (a) Adapted from Gay and Dunning, 1992.

Hall effects was observed. The first successful experiment was realized in a NM semiconductor by Brüne *et al.* (2010).

In Fig. 2(c), we show an earlier variant of the double-scattering experiment proposed by Hirsch (1999) for observing the SHE-ISHE in a solid-state device. Instead of considering the spin current produced directly by the charge current via the SHE, Hirsch focused on the edges of the SHE part of the sample. Here, the transverse spin current accumulates, forming a nonequilibrium spin polarization of opposite sign at the two opposite edges. In NMs, the nonequilibrium spin polarization corresponds to a splitting of the spin-up and spin-down chemical potentials. When connecting the two edges, the gradient of the spin-dependent chemical potentials will generate a circulating spin current which is then detected by the ISHE spin current meter inserted into the closed spin-current circuit. The idea for the experiment was borrowed from the ordinary Hall effect (HE) in which opposite charge accumulates at opposite edges due to the Lorentz force, and the resulting electrochemical potential gradient generates a circulating charge current when the two edges are connected in the closed circuit geometry.

Realizing the Hirsch (1999) SHE-ISHE device remains a challenge. Similarly to the Hankiewicz *et al.* (2004) design directly copying the Mott double-scattering experiment, the wires connecting the SHE and ISHE parts of Hirsch's device have to be shorter than the characteristic spin-conserving length scale. The spin-orbit coupling required for the SHE-ISHE in the first place, however, tends to make the spin lifetime short. The additional complication is that the spin-orbit coupling also limits, again via the finite spin lifetime, the width of the sample edge with nonzero spin accumulation from which the spin current is extracted in Hirsch's device proposal.

While difficult to realize experimentally, Hirsch's concept is stimulating for comprehending the general key distinctions between charge and spin current. Electron charge is a conserved quantity but its spin direction is not conserved. In the charge HE, the difference between electrochemical potentials at the edges determines the uniform charge current which in steady-state flows through the closed circuit. In the SHE, on the other hand, the spin current in the connecting wire of Hirsch's device is not uniform and is not determined by the difference between the spin-dependent chemical potentials at the left and right edges. It is determined by the local gradient of the spin-dependent chemical potentials which vanishes (i.e., the spin current also vanishes) on the length scale given by the spin lifetime. As long as the connecting wire is longer than the characteristic spin-conserving length scale, there is no difference between a closed and an open spin-current circuit.

Hirsch's concept also points to the general applicability of the ISHE as an electrical spin detector. Even in electrically open circuits, the nonconserving, nonuniform spin current can still flow. It is then readily separated from the charge current and can be detected by the ISHE. The Mott polarimetry of electron beams in vacuum chambers and AHE polarimetry of charge currents in itinerant magnets is, therefore, complemented by the ISHE polarimetry of pure spin currents.

A spin current in a NM of any origin (not only of the SHE origin) can be detected by the ISHE. Indeed, ISHE detectors of pure spin currents became a standard measurement tool. They led to, e.g., the discovery of the spin Seebeck effect (Uchida *et al.*, 2008, 2010; Jaworski *et al.*, 2010) and helped establish the emerging field of spin caloritronics (Bauer, Saitoh, and van Wees, 2012).

Given the inherent challenges in realizing Hirsch's device, it is not surprising that experimentalists initially avoided attempts to perform the SHE-ISHE double-scattering experiments and that the first observations of the SHE (Kato *et al.*, 2004a; Wunderlich *et al.*, 2004, 2005) and ISHE (Saitoh *et al.*, 2006; Valenzuela and Tinkham, 2006; Zhao *et al.*, 2006) were made separately. When the Hankiewicz *et al.* (2004) H-bar microdevice was eventually realized in experiment by Brüne *et al.* (2010), both the SHE and ISHE had already been established independently.

B. Intrinsic spin Hall and quantum Hall effects

Remarkably, the H-bar experiment (Brüne *et al.*, 2010) discussed in the previous section was performed in a ballistic transport regime where the picture of Mott scattering, single or double, did not apply. A fundamental physics principle makes the SHE in solid-state systems richer than in the Mott electron

beams scattered from spin-orbit-coupled targets in vacuum chambers. For electrons moving in a crystal, a transverse spin-dependent velocity can be generated by the relativistic spin-orbit field of a perfect crystal even in the absence of scattering. The roots of this intrinsic SHE are clearly distinct from the Mott (skew) scattering AHE and from the Mott scattering of free electron beams.

The reactive term responsible for the intrinsic SHE is akin to the ordinary HE in which the transverse deflection of electrons is a reaction to the Lorentz force of the applied magnetic field acting on the moving carriers [see Fig. 3(a)]. In strong magnetic fields, the quantum Hall effect (QHE) provides a disorder-independent measure of the quantum conductance e^2/h. The integer multiples of e^2/h observed in the QHE correspond to the number of occupied dissipationless chiral edge states in the conductor [see Fig. 3(b)].

Besides the externally applied Lorentz force, electrons moving in a crystal can experience an internal spin-orbit force. The effect was first recognized in FMs where it generates the intrinsic AHE [see Fig. 3(a)] (Karplus and Luttinger, 1954; Jungwirth, Niu, and MacDonald, 2002; Onoda and Nagaosa, 2002). Murakami, Nagaosa, and Zhang (2003) and Sinova *et al.* (2004) predicted that the same spin-orbit force derived directly from the relativistic band structure of a NM can induce the SHE without involving Mott scattering [see Fig. 3(c)]. The first experimental observations confirmed that the SHE can indeed have the two distinct origins. While Wunderlich *et al.* (2004, 2005) ascribed the circularly polarized luminescence signal from the edge of the *p*-GaAs sample to the intrinsic SHE, Kato *et al.* (2004a) detected an edge Kerr rotation signal in *n*-GaAs due to the extrinsic, skew-scattering SHE.

Following the discovery of the phenomenon, SHE experiments in semiconductors using optical spin detection have explored the basic phenomenologies of the extrinsic and intrinsic SHEs (Kato *et al.*, 2004a; Wunderlich *et al.*, 2004, 2005; Nomura *et al.*, 2005; Sih *et al.*, 2005, 2006; Stern *et al.*, 2006, 2007; Chang *et al.*, 2007; Matsuzaka, Ohno, and Ohno, 2009). They also demonstrated the potential of the SHE as a spin-current source (Sih *et al.*, 2006). The experimental observation of the ISHE in a semiconductor was performed by a two-color optical excitation technique with perpendicular linear polarizations (Zhao *et al.*, 2006). The spin current produced by the laser excitation is transferred due to the ISHE into a transverse electrical current, resulting in a spatially dependent charge accumulation which was detected by the optical transmission signal of a probe laser beam. These all-optical measurements were eventually performed on time scales shorter than the scattering time and provided a direct demonstration of the intrinsic SHE signal (Werake, Ruzicka, and Zhao, 2011).

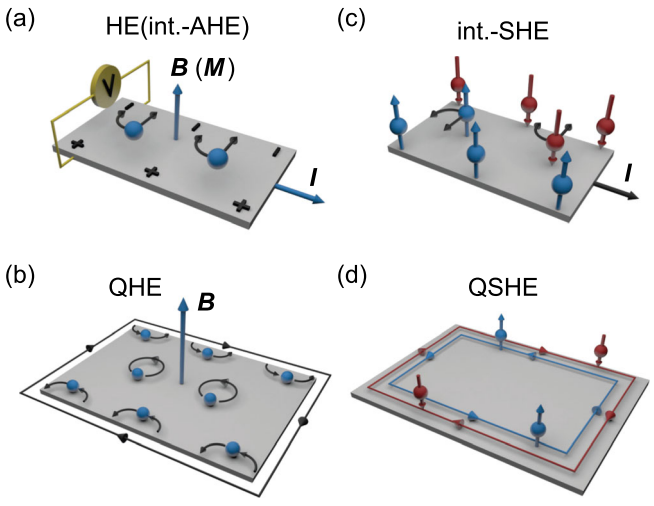

FIG. 3 (color online). Schematics of the HE and the AHE (a), the QHE (b), the SHE (c), and the QSHE (d). In the HE and QHE, the carrier deflection is a reaction to the Lorentz force. In the cases of the intrinsic AHE, SHE, and QSHE, the carriers experience an internal spin-orbit force.

The intrinsic SHE proposal triggered an intense theoretical debate which is summarized in several review articles (Murakami, 2006; Engel, Rasbha, and Halperin, 2006; Schliemann, 2006; Sinova *et al.*, 2006; Sinova and MacDonald, 2008; Culcer, 2009; Hankiewicz and Vignale, 2009; Vignale, 2010; Raimondi *et al.*, 2012). Combined with the established physics of the dissipationless QHE, the intrinsic SHE led to the prediction and subsequent experimental verification of the quantum spin Hall effect (QSHE) in a HgTe 2D system (Murakami, Nagaosa, and Zhang, 2004; Kane and Mele, 2005; Bernevig, Hughes, and Zhang, 2006; König *et al.*, 2007; Hasan and Kane, 2010). In the time-reversal symmetric QSHE, the chiral edge states of the QHE are replaced by pairs of helical spin-edge states [see Fig. 3(d)]. This leads to a $2e^2/h$ quantization of the observed transport signal (König *et al.*, 2007) and resistance values in nonlocal experiments that can be expressed as specific integer fractions of the inverse conductance quanta (Büttiker, 2009; Roth *et al.*, 2009). The QSHE initiated the new research field of topological insulators (Hasan and Kane, 2010; Moore, 2010). In this context, we also point out the connection of the spin Hall phenomena to the research of 2D systems with spin and pseudospin degrees of freedom, including graphene and layered transition-metal dichalcogenides (Avsar *et al.*, 2014; Qian *et al.*, 2014; Xu *et al.*, 2014).

C. Spin Hall effect and magnetic multilayers

Among the early SHE device proposals, Zhang (2000) suggested to electrically detect the edge spin accumulation produced by the SHE using an attached FM probe (Silsbee, 1980; Johnson and Silsbee, 1985). In a broader context, the idea of connecting the SHE with the more mature field which utilized FMs for injection and detection of spins in NMs fueled numerous studies of fundamental importance for the SHE field. Electrical spin injection from a FM contact and electrical observation of the ISHE on a Hall cross patterned in the NM was demonstrated by Valenzuela and Tinkham (2006).

The original proposal by Zhang (2000) was first demonstrated in metal spin Hall devices by Kimura *et al.* (2007). They showed that the same NM electrode attached to the FM can generate the SHE or the ISHE, i.e., can be used as an electrical spin injector or detector (Valenzuela and Tinkham, 2006; Kimura *et al.*, 2007; Vila, Kimura, and Otani, 2007; Seki *et al.*, 2008; Mihajlovic *et al.*, 2009).

Compared to metals, semiconductor spin transport devices with FM metal electrodes can suffer from the problem of the resistance mismatch, which hinders efficient spin transport across the interface (Schmidt *et al.*, 2000). The introduction of a highly resistive tunnel barrier between the FM metal electrode and the semiconductor channel solves this problem (Rasbha, 2000; Lou *et al.*, 2007) and FM tunnel contacts were successfully used to detect the SHE-induced spin-accumulation in a semiconductor (Garlid *et al.*, 2010). Similarly, an electrical spin injection from a FM-semiconductor tunnel contact was used to demonstrate, side by side, the electrical spin detection by the ISHE and by the FM electrode (Olejník *et al.*, 2012).

Using FMs contributed significantly to the basic understanding of the SHE. Apart from the transport measurements, NM-FM hybrid structures also allow one to combine the SHE physics with the field of magnetization dynamics. The ISHE and SHE can be investigated using spin pumping (SP) and other related dynamic methods in structures comprising FMs and NMs, as illustrated in Fig. 4 (Saitoh *et al.*, 2006; Ando *et al.*, 2008, 2009; Mosendz, Pearson *et al.*, 2010; Mosendz, Vlaminck *et al.*, 2010; Czeschka *et al.*, 2011; Liu *et al.*, 2011; Miron, Garello *et al.*, 2011; Liu, Pai, Li *et al.*, 2012; Saitoh and Ando, 2012; Bai *et al.*, 2013; Wei *et al.*, 2014). In return, the SHE was found to provide efficient means for injecting spin currents into the FM, generating the STT (Ralph and Stiles, 2008), and by this electrically controlling magnetization in FMs with potential applications in spintronic information technologies (Miron, Garello *et al.*, 2011; Miron *et al.*, 2011; Liu, Pai, Li *et al.*, 2012; Emori *et al.*, 2013; Ryu *et al.*, 2013). Moreover, the ISHE detection of pure spin currents did not remain limited to NMs but is now used also in FMs (Miao *et al.*, 2013; Azevedo *et al.*, 2014) and antiferromagnets (Freimuth, Blügel, and Mokrousov, 2010; Mendes *et al.*, 2014; Zhang *et al.*, 2014).

In general, when SHE-induced torques in the adjacent FM are considered in the description of the dynamic magnetization (the Landau-Lifshitz-Gilbert equation), two types of torques can occur. An (anti-)damping-like torque which has the same functional shape as the Gilbert damping term (and thus can manifest itself in an increased or decreased Gilbert damping) and a field-like term which alters the magnetic energy landscape and can be observed as a shift of the resonance line in a FMR experiment. FMR allows the determination of the total internal magnetic field in a sample as well as investigation of dissipation. Thus, in principle FMR-like techniques enable determination of field-like and (anti-)damping-like contributions of SHE-induced torques.

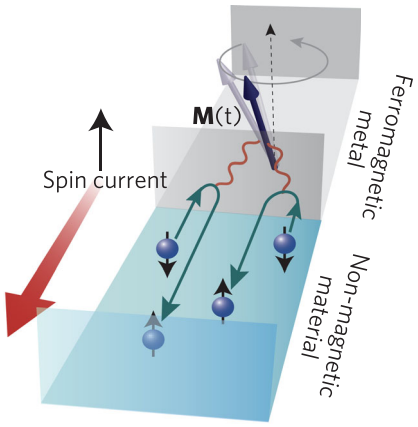

FIG. 4 (color online). Illustration of the SP spin-current generation by magnetization dynamics from a FM into a NM. From Ando *et al.*, 2011b.

If these current-induced torques arise only from the absorption of the spin current generated by the SHE in the NM, the analysis of field-symmetric and field-antisymmetric contributions of the detected dc output voltage at FMR allows for a quantitative determination of the strength and symmetry of the SHE-induced torques, as well as the spin Hall angle of the NM.

Note that the torque can induce not only the small-angle FMR precession but the lateral current along a NM-FM interface can also drive domain walls (Miron *et al.*, 2011; Emori *et al.*, 2013; Haazen *et al.*, 2013; Ryu *et al.*, 2013) or switch the magnetization in the FM (Miron, Garello *et al.*, 2011; Liu, Pai, Li *et al.*, 2012). This may have practical implications for designing domain-wall based memories or for three-terminal magnetic tunnel junction bits with the lateral writing current decoupled from the perpendicular readout current.

D. Spin Hall effect, spin galvanics, and spin torques

From the early experiments with the relativistic torques, it was realized that the SHE is not the only possible mechanism responsible for torques induced by the lateral current in the NM-FM bilayers (Manchon *et al.*, 2008). The interface breaks the structural inversion symmetry which implies that the SHE-STT can be accompanied by another microscopic mechanism. Its origin is in the so-called spin galvanic phenomena that were explored earlier in inversion-asymmetric NMs (Ivchenko and Ganichev, 2008). In the picture discussed in the previous section, the spin current generated in the NM via the relativistic SHE is absorbed in the FM and induces the STT. In the competing scenario, a nonequilibrium spin density of carriers is generated in inversion-asymmetric systems via the relativistic ISGE (Ganichev *et al.*, 2004; Kato *et al.*, 2004b; Silov *et al.*, 2004; Wunderlich *et al.*, 2004, 2005; Belkov and Ganichev, 2008; Ivchenko and Ganichev, 2008). A SOT is then directly induced if the carrier spins are exchange coupled to magnetic moments (Bernevig and Vafek, 2005; Manchon *et al.*, 2008; Chernyshov *et al.*, 2009; Miron *et al.*, 2010).

From the early observations in nonmagnetic semiconductors, SHE and ISGE are known as companion phenomena, both allowing for electrical alignment of spins in the same structure (Kato *et al.*, 2004a, 2004b; Wunderlich *et al.*, 2004, 2005). Hand in hand, SHE and ISGE evolved from subtle academic phenomena to efficient means for electrically reorienting magnets. Understanding the relation between the spin Hall and spin galvanic phenomena is, therefore, important not only from the basic physics perspective but has also practical implications for spintronic devices.

The term spin galvanic effect (SGE) is derived from the analogy to the galvanic (voltaic) cell. Instead of a chemical

reaction, however, it is the spin polarization that generates an electrical current (voltage) in the SGE. Inversely, an electrical current generates the spin polarization in the ISGE.

Following theoretical predictions of the phenomena (Ivchenko and Pikus, 1978; Aronov and Lyanda-Geller, 1989; Ivchenko, Lyanda-Geller, and Pikus, 1989; Edelstein, 1990; Malâshukov and Chao, 2002; Inoue, Bauer, and Molenkamp, 2003), it was the SGE that was initially observed in an asymmetrically confined two-dimensional electron gas (2DEG) in a GaAs quantum well (Ganichev *et al.*, 2002). The key signature of the SGE is the electrical current-induced by a nonequilibrium, but uniform, polarization of electron spins. The microscopic origin of the effect is illustrated in Fig. 5. In the nonequilibrium steady state, the spin-up and spin-down subbands have different populations, induced in the Ganichev *et al.* (2002) experiment by a circularly polarized light excitation. Simultaneously, the two subbands for spin-up and spin-down electrons are shifted in momentum space due to the inversion asymmetry of the semiconductor structure, which leads to an inherent asymmetry in the spin-flip scattering events between the two subbands. This results in the flow of the electrical current.

A microscopic picture of the ISGE is illustrated in Fig. 6. The uniform nonequilibrium spin density occurs as a consequence of an electric-field and scattering induced redistribution of carriers on the Fermi surface whose texture of spin expectation values has a broken inversion symmetry. For the Rashba spin-orbit coupling, illustrated in Fig. 6 for one chirality, the uniform in-plane spin polarization is perpendicular to the applied electrical current.

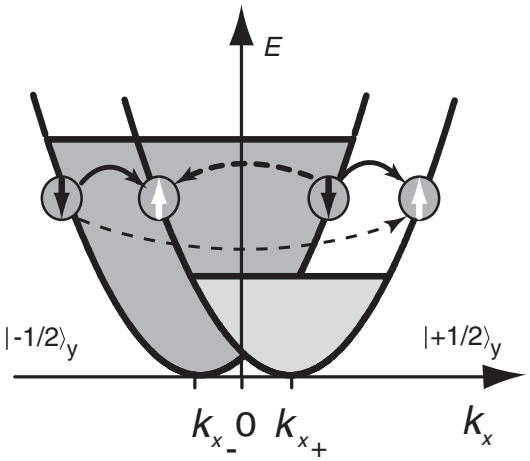

FIG. 5. Microscopic origin of the spin galvanic current in the presence of k-linear terms in the electron Hamiltonian. The $\sigma_y k_x$ term in the Hamiltonian splits the conduction band into two parabolas with the spin $\pm 1/2$ in the y direction. If one spin subband is preferentially occupied, for example, by spin injection (the $|-1/2\rangle_y$ states shown in the figure) asymmetric spin-flip scattering results in a current in the x direction. The rate of spin-flip scattering depends on the value of the initial and final k vectors. There are four distinct spin-flip scattering events possible, indicated by the arrows. The transitions sketched by dashed arrows yield an asymmetric occupation of both subbands and hence a current flow. If, instead of the spin-down subband, the spin-up subband is preferentially occupied the current direction is reversed. From Ganichev *et al.*, 2002.

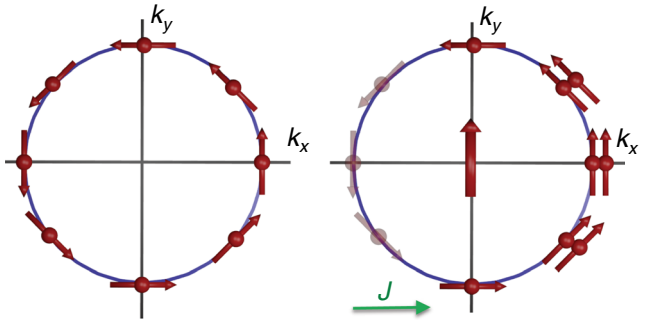

FIG. 6 (color online). Left panel: Rashba spin texture for one of the chiral states in equilibrium with zero net spin density. Right panel: nonequilibrium redistribution of eigenstates in an applied electric field resulting in a nonzero spin density due to broken inversion symmetry of the spin texture. The opposite chirality spin texture with lower Fermi wave vector is not drawn for clarity. This reversed chirality will give and opposite but lower contribution to the one shown, hence not changing the basic physics illustrated here.

Initial observations of the ISGE were made in parallel with the initial SHE experiments, in both cases employing the Kerr-Faraday magneto-optical detection methods or circularly polarized luminescence (Ganichev *et al.*, 2004; Kato *et al.*, 2004a, 2004b; Silov *et al.*, 2004; Wunderlich *et al.*, 2004, 2005; Belkov and Ganichev, 2008; Ivchenko and Ganichev, 2008). Kato *et al.* (2004a, 2004b) observed the SHE and ISGE in the same strained bulk n-InGaAs sample and Wunderlich *et al.* (2004, 2005) detected the two effects in the same asymmetrically confined 2D hole gas (2DHG) in a AlGaAs/GaAs heterostructure.

Subsequently, it was predicted (Bernevig and Vafek, 2005) and experimentally verified (Chernyshov *et al.*, 2009) that the ISGE can generate relativistic SOTs in a ferromagnetic semiconductor (Ga,Mn)As with broken inversion symmetry in the strained crystal structure of a thin film sample. The reciprocal relativistic effect converting magnetization dynamics into a charge signal has also been observed in this inversion-asymmetric (Ga,Mn)As material (Ciccarelli *et al.*, 2014).

In the NM-FM bilayers with broken structural inversion symmetry, both the SHE- and ISGE-based mechanisms have been found to contribute to the relativistic spin torques (Manchon *et al.*, 2008; Miron *et al.*, 2010; Pi *et al.*, 2010; Miron, Garello *et al.*, 2011; Suzuki *et al.*, 2011; Garello *et al.*, 2013; Kim *et al.*, 2013; Pai *et al.*, 2014). Similarly to the bulk inversion-asymmetric materials, in the structurally asymmetric NM-FM bilayers the reciprocal effects converting magnetization dynamics into charge signals have been observed and attributed to the ISHE and SGE (Saitoh *et al.*, 2006; Rojas-Sánchez, Vila *et al.*, 2013).

As mentioned, the SHE and the Mott scattering of free electron beams can have the same extrinsic skew-scattering origin (captured by the second-order Born approximation). Moreover, in condensed matter systems, the SHE can arise from the spin-dependent transverse deflection induced by the intrinsic spin-orbit coupling in a perfect crystal with no impurities. We also mentioned that this intrinsic SHE has its direct counterpart in systems with broken time-reversal symmetry in the intrinsic AHE.

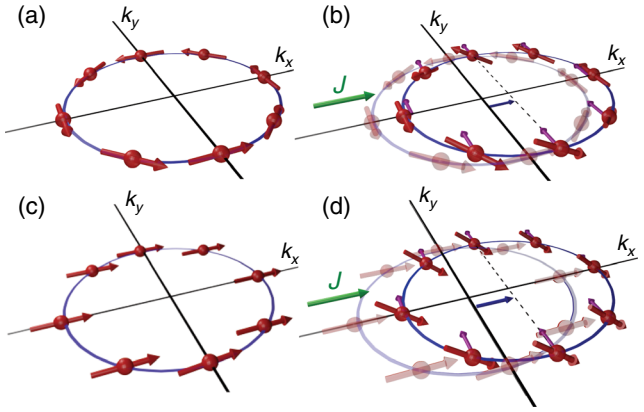

FIG. 7 (color online). (a) A model equilibrium spin texture in a 2D Rashba spin-orbit-coupled system with spins (thick arrows) pointing perpendicular to the momentum. (b) In the presence of an electrical current along the x direction the Fermi surface (circle) is displaced along the same direction. When moving in momentum space, electrons experience an additional spin-orbit field (thin arrows). In reaction to this nonequilibrium current-induced field, spins tilt up for $k_y > 0$ and down for $k_y < 0$, creating a spin current in the y direction. (c) A model equilibrium spin texture in a 2D Rashba spin-orbit-coupled system with an additional time-reversal symmetry breaking exchange field of a strength much larger than the spin-orbit field. In equilibrium, all spins in this case align approximately with the direction of the exchange field. (d) The same reactive mechanism as in (b) generates a uniform, nonequilibrium out-of-plane spin polarization. Adapted from Sinova *et al.*, 2004 and Kurebayashi *et al.*, 2014.

The spin galvanic phenomena, on the other hand, are traditionally considered to originate in NMs only from extrinsic origins (seen already in the first-order Born approximation scattering). Nevertheless, the physics of the SHE, AHE, spin galvanics, and relativistic spin torques can be entangled even when considering the intrinsic effects. In Fig. 7 we illustrate that the same current-induced reactive mechanism that generates the transverse spin current in the intrinsic SHE can induce a uniform spin polarization, i.e., a signature characteristic of the ISGE, in systems with broken space and time-reversal symmetry. Relativistic SOTs generated by the nonequilibrium uniform spin polarization of this intrinsic origin were identified in the FM semiconductor (Ga,Mn)As (Kurebayashi *et al.*, 2014).

Current-induced torques generated by the companion spin Hall and spin galvanic phenomena are not limited to magnets with FM order. In antiferromagnets, the SHE- or ISGE-induced effective fields can have a microscopically staggered nature, i.e., can alternate in sign between the antiferromagnetic spin sublattices, and by this couple strongly to the Néel magnetic order (Železný *et al.*, 2014). Since external magnetic fields couple weakly to antiferromagnetic moments, the electrically generated staggered fields are rather unique in providing efficient means for the manipulation of antiferromagnets (Wadley *et al.*, 2015).

III. THEORY OF THE SPIN HALL EFFECT

The SHE is a prime example of a field germinated directly from several key theoretical predictions and one which needed the correct timing to come to its full life. It all began with the seminal prediction of the extrinsic SHE by Dyakonov and Perel (1971b) based on a phenomenological theory that considered the consequences of chiral Mott scattering in a solid-state system. This prediction laid dormant for almost three decades until Hirsch (1999) and Zhang (2000) made a similar prediction, but at a time that the nascent field of spintronics could fully exploit the notion of the SHE.

Shortly after this, Murakami, Nagaosa, and Zhang (2003) and Sinova *et al.* (2004) predicted the intrinsic SHE based on linear response microscopic theories of strong spin-orbit-coupled materials. It is perhaps at this point that the field of SHE surged forward in a flurry of enormous theoretical activity, later on culminating in the parallel discoveries of the extrinsic (Kato *et al.*, 2004a) and intrinsic (Wunderlich *et al.*, 2004, 2005) SHE.

The theories of the SHE have naturally emerged from the theory of the AHE. However, the ever-present key difference between the SHE and the AHE is that spin, unlike charge, is not a conserved quantity in most cases. This makes the examination of experiments and predictions more involved in the case of the SHE.

In the initial predictions of the extrinsic SHE, this was dealt with by writing down phenomenological theories based on coupled spin-charge drift-diffusion equations derived from symmetry considerations. The approach is well justified in the weak spin-orbit-coupling regime (Dyakonov and Perel, 1971b; Hirsch, 1999; Zhang, 2000; Dyakonov and Khaetskii, 2008). However, within the strong spin-orbit-coupling regime, the dominant coherent effects of the intrinsic SHE are more difficult to couple to such phenomenological theories. This is particularly relevant for heavy transition metals.

It is within this strong spin-orbit-coupling regime that the AHE has made its furthest progress within the last decade. The intrinsic, skew-scattering, and side-jump mechanisms that give rise to the AHE were initially introduced and defined only through the nonsystematic semiclassical formalism. This did not allow for a direct application of fully microscopic computational approaches to calculate the effect in real materials. Over the last decade, a more systematic approach has been followed that aimed at reaching agreement in nontrivial models using different linear response formalisms. This has led to a better established, microscopic-theory description of the mechanisms that is applicable to *ab initio* computational techniques of complex materials (Sinitsyn *et al.*, 2007; Kovalev, Sinova, and Tserkovnyak, 2010; Nagaosa *et al.*, 2010).

We spend the first part of Sec. III.A defining and explaining each of the contributions and their origins in the more modern parsing of the spin-dependent Hall transport theory. We will try to clarify, in particular, the typical misconceptions that sometimes linger in the literature regarding which aspect of the spin-orbit coupling—within the crystal itself or within the disorder potential—contributes to each mechanism. We borrow in this part extensively from Nagaosa *et al.* (2010) and direct the interested reader to this previous review for detailed explanations of the different linear response theories and the resolution of some of the historical controversies.

We follow in Sec. III.B with a description of the phenomenological spin-charge drift-diffusion equations that are often

used to fit experiments. These equations are symmetry based and their phenomenological parameters are often extracted from fits to experiments.

Because of the challenge of merging the strong spin-orbit-coupled microscopic theories and the phenomenological weak spin-orbit-coupling theories, one of the more popular models that is used to describe the SHE is based on a simple Hamiltonian in which the spin-orbit coupling is only present in the disorder potential. We discuss such a model in Sec. III.C. This theory has the benefit of having a single parameter—the strength of the spin-orbit coupling of the disorder potential. The parameter can be fitted to the spin-diffusion length and from this the value of the SHE can be estimated (Zhang, 2000; Crépieux and Bruno, 2001; Engel, Halperin, and Rashba, 2005; Maekawa and Takahashi, 2012). However, as seen by comparing to experiment, this model gives sensible results in the weak spin-orbit-coupling regime but misses the coherent effects of the band structure in strongly spin-orbit-coupled materials.

In Sec. III.D, we discuss in detail the theory of SP and how it is utilized to measure the ISHE and the spin Hall angle. The theory of SP introduces the concept of the spin-mixing conductance (Tserkovnyak, Brataas, and Bauer, 2002a), another parameter borrowed from the weak spin-orbit-coupled systems, which is at present often used in analyzing magnetization-dynamics experiments in connection to the physics of the SHE (Saitoh *et al.*, 2006). Besides introducing the basic concepts of SP and its connection to the measurements of the ISHE, we discuss the range of assumptions and limits which are often used when analyzing experiments.

In Sec. III.E, we present the formalism primarily used in the strong spin-orbit-coupled systems. The formalism is based in the Kubo formula and exploited successfully in transition metals (Tanaka *et al.*, 2008; Freimuth, Blügel, and Mokrousov, 2010). Calculations seem to indicate that for these metals the principal contribution, as in the AHE, arises from the intrinsic deflection mechanism.

A. Mechanisms of the spin Hall effect

The spin-dependent Hall effects (AHE, SHE, and ISHE) originate from three distinct microscopic mechanisms that they all share: the skew, the side jump, and the intrinsic mechanisms. The mechanisms are caused by coherent band mixing effects induced by the external electric field and the disorder potential. This makes them more complex than the simpler single-band diagonal transport.

As with other coherent interference transport phenomena, they cannot be directly explained using traditional semiclassical Boltzmann theory. It is then not surprising that the original proposals based on semiclassical theory for the intrinsic, skew-scattering, and side-jump mechanisms brought insightful new concepts, as well as seeds for ensuing controversies in the debate over the quantum-mechanical microscopic origins of the AHE and SHE.

There exists now a more modern, stricter definition of the mechanisms within microscopic theories. However, to keep continuity and not create further confusion, this more modern approach has inherited the already established lexicon [see Nagaosa *et al.* (2010), Sec. IV].

The new parsing of the microscopic mechanisms is based on both experimental and microscopic-transport theory considerations, rather than on the identification of one particular effect within semiclassical theory. The justification here is, of course, primarily on the AHE, not the SHE. For the SHE, the spin Hall conductivity and its consequences have to be ultimately coupled to the spin accumulation that it induces and can therefore depend on the method of measurement. In other words, depending on the measurement, the spin accumulation induced by the SHE may vary, e.g., in nonlocal transport measurements versus FMR-based measurements.

As mentioned in the introduction of Sec. III, the key recent development that led to a better understanding of the mechanisms was linking directly the semiclassical and microscopic theory of spin-dependent Hall transport. This link between the semiclassically defined processes and their fully equivalent mutliband microscopic theories was established by fully generalizing the Boltzmann transport theory to take interband coherence effects into account (Sinitsyn *et al.*, 2007; Nagaosa *et al.*, 2010).

Based on what we have learned from the AHE, a very natural classification of contributions is to separate them according to their dependence on the transport lifetime τ. This classification is directly guided by experiment and by the microscopic theory of metals. Within the metallic regime, disorder is treated perturbatively and higher order terms vary with a higher power of the quasiparticle scattering rate τ^{-1}. As we discuss, it is relatively easy to identify contributions to the anomalous or spin Hall conductivity σ_{xy}^{H}, which vary as τ^{1} and as τ^{0}. In experiments of the AHE, a similar separation can sometimes be achieved by plotting σ_{xy} vs the longitudinal conductivity $\sigma_{xx} \propto \tau$, when τ is varied by altering disorder or varying temperature.

However, it is important to note that several microscopically distinct contributions can share the same τ dependence (Sinitsyn *et al.*, 2007; Sinitsyn, 2008). The contribution proportional to τ^{1} we define as the *skew-scattering* contribution, $\sigma_{xy}^{H-\mathrm{skew}}$. The second contribution proportional to τ^{0} (or independent of σ_{xx}) we further separate into two terms: *intrinsic* and *side jump*.

The first term arises from the evolution of spin-orbit-coupled quasiparticles as they are accelerated by an external electric field in the absence of disorder. The second term arises from scattering events from impurities that do not include the skew-scattering contribution. This then leaves a unique definition for the side-jump term, as $\sigma_{xy}^{H-\mathrm{sj}} \equiv \sigma_{xy}^{H} - \sigma_{xy}^{H-\mathrm{skew}} - \sigma_{xy}^{H-\mathrm{int}}$.

We further describe these contributions below. We note that the above definitions have not relied on linking the terms to semiclassical processes such as side-jump scattering (Berger, 1970) or skew scattering from asymmetric contributions to the semiclassical scattering rates (Smit, 1958), as was done in earlier theories.

The ideas explained briefly in this section are substantiated in the recent review by Nagaosa *et al.* (2010), which analyzes the tendencies in the AHE data of several material classes and extensively discusses the AHE theory. The extensions to the other spin-dependent Hall effects, such as SHE and ISHE, require the coupling of these spin-current generating mechanisms to spin-charge drift-diffusion transport equations that

are appropriate to describe the particular experiment, be it optical or electrical.

1. Intrinsic mechanism

Among the three contributions, the easiest to evaluate accurately and the one that has dominated most theoretical studies is the intrinsic contribution. There is a direct link of the intrinsic effect to the semiclassical theory in which the induced interband coherence is captured by an anomalous velocity arising from a momentum-space Berry phase.

In the context of the AHE, this contribution was first derived by Karplus and Luttinger (1954) but its topological nature was not fully appreciated until recently (Jungwirth, Niu, and MacDonald, 2002; Onoda and Nagaosa, 2002). The work of Jungwirth, Niu, and MacDonald (2002) was motivated by the experimental importance of the AHE in FM semiconductors and also by the analysis of the relationship between momentum-space Berry phases and anomalous transverse velocities in semiclassical transport theory (Sundaram and Niu, 1999; Xiao *et al.*, 2010). Its connection to the SHE was described by Murakami, Nagaosa, and Zhang (2003) and Sinova *et al.* (2004).

The intrinsic contribution to the spin Hall conductivity is dependent only on the band structure of the perfect crystal, hence its name. Pictorially, it can be seen to arise from the nonequilibrium electron dynamics of the Bloch electrons as they are accelerated in an electric field and undergo spin precession due to the induced momentum-dependent magnetic field, as illustrated in Sec. II.D, Fig. 7. Here the system is described by a 2D Rashba Hamiltonian,

$$H = \frac{p^2}{2m} - \frac{\lambda}{\hbar}\sigma \cdot (\hat{z} \times \mathbf{p}), \tag{3.1}$$

where $p = \hbar k$ is the 2D electron momentum, λ is the Rashba coupling constant, σ the Pauli matrices, m the electron effective mass, and $\hat{z}$ the unit vector perpendicular to the 2DEG plane.

For this example, the dynamics of an electron spin in the presence of time-dependent spin-orbit coupling is described by the Bloch equation (Sinova *et al.*, 2004),

$$\frac{\hbar d\hat{n}}{dt} = \hat{n} \times \mathbf{\Delta}(t) + \alpha \frac{\hbar d\hat{n}}{dt} \times \hat{n}, \tag{3.2}$$

where $\hat{n}$ is the direction of the spin and α is a damping parameter that we assume is small. In Eq. (3.2), the $\mathbf{p}$-dependent effective Zeeman coupling induced by the spin-orbit-coupling term is given by $-\mathbf{s} \cdot \mathbf{\Delta}/\hbar$, where $\mathbf{\Delta} = 2\lambda/\hbar(\hat{z} \times \mathbf{p})$. For a Rashba effective magnetic field with magnitude Δ_1 that initially points in the $\hat{x}_1$ direction, the effective field then tilts (arbitrarily slowly) slightly toward $\hat{x}_2$, where $\hat{x}_1$ and $\hat{x}_2$ are orthogonal in-plane directions. It follows from the linear response limit of Eq. (3.2) that

$$\begin{aligned} \frac{\hbar dn_2}{dt} &= n_z \Delta_1 + \alpha dn_z/dt, \\ \frac{\hbar dn_z}{dt} &= -\Delta_1 n_2 - \alpha dn_2/dt + \Delta_2, \end{aligned} \tag{3.3}$$

where $\Delta_2 = \mathbf{\Delta} \cdot \hat{x}_2$. By solving these inhomogeneous coupled equations, it follows that to leading order in the slow-time dependences $n_2(t) = \Delta_2(t)/\Delta_1$, i.e., the $\hat{x}_2$ component of the spin rotates to follow the direction of the spin-orbit field, and that

$$n_z(t) = \frac{1}{\Delta_1^2} \frac{\hbar d\Delta_2}{dt}. \tag{3.4}$$

The dynamics give rise to the spin current in the $\hat{y}$ direction,

$$j_{s,y} = \int_{\text{annulus}} \frac{d^2\mathbf{p}}{(2\pi\hbar)^2} \frac{\hbar n_{z,\mathbf{p}}}{2} \frac{p_y}{m} = \frac{-eE_x}{16\pi\lambda m}(p_{F+} - p_{F-}), \tag{3.5}$$

where p_{F+} and p_{F-} are the Fermi momenta of the majority and minority spin Rashba bands (Sinova *et al.*, 2004).

We choose the example based on the Rashba system because it is simple to see pictorially the intrinsic contribution. However, for this particular simple example, in a large range of Fermi energies the result for the intrinsic spin Hall conductivity turns out to be $\sigma_{xy}^{H-\text{int}} = -(e/\hbar) j_{s,y}/E_x = e^2/8\pi\hbar$. This contribution is eventually canceled by short-range disorder scattering because the induced spin current is proportional to the spin dynamics, which should vanish in the steady state (Inoue, Bauer, and Molenkamp, 2004; Dimitrova, 2005; Raimondi *et al.*, 2012). The issue of the cancellation between the intrinsic and side-jump contribution, the so-called vertex corrections, has been debated extensively and we discuss it briefly below. Here, we point out that the exact cancellation is only present in the parabolic 2D linear Rashba Hamiltonian and is not present in other spin-orbit-coupled Hamiltonians corresponding to realistic material systems (Shytov *et al.*, 2006; Sinova *et al.*, 2006; Raimondi *et al.*, 2012).

The above result, illustrated in a simple semiclassical form, is usually best evaluated directly from the Kubo formula for the spin Hall conductivity for an ideal lattice (Sinova *et al.*, 2004),

$$\begin{aligned} \sigma_{xy}^{H-\text{int}} = \frac{e^2}{V} \sum_{\mathbf{k}, n \neq n'} & (f_{n',k} - f_{n,k}) \\ & \times \frac{\text{Im}[\langle n'k|\hat{j}^z_{\text{spin}\,x}|nk\rangle\langle nk|v_y|n'k\rangle]}{(E_{nk} - E_{n'k})(E_{nk} - E_{n'k} - \hbar\omega - i\eta)}, \end{aligned} \tag{3.6}$$

where n, n' are band indices, $\mathbf{j}^z_{\text{spin}} = \frac{\hbar}{4}\{\sigma_z, \mathbf{v}\}$ is the spin-current operator, ω and η are set to zero in the dc clean limit, and the velocity operators at each $\mathbf{p}$ are given by $\hbar v_i = \hbar\partial H(\mathbf{p})/\partial p_i$. It is important to emphasize that the semiclassical derivation describing the time-dependent polarization of the Bloch states as they are accelerated and the Kubo formalism are entirely equivalent, as they should be from a correct treatment of linear response of this contribution. The intrinsic contribution to the AHE and SHE conductivity can also be obtained from the semiclassical theory of wave packet dynamics (Sundaram and Niu, 1999; Jungwirth, Niu, and MacDonald, 2002; Culcer *et al.*, 2004; Xiao *et al.*, 2010).

What makes the intrinsic contribution quite unique, particularly in the AHE, is that it is directly linked to the topological properties of the Bloch states. Specifically, it is

proportional to the integration over the Fermi sea of the Berry's curvature of each occupied band.

One of the motivations for identifying the intrinsic contribution $\sigma_{xy}^{H-\mathrm{int}}$ is that it can be evaluated accurately even for materials with relatively complex electronic band structure using microscopic *ab initio* theory techniques. In many materials which have strongly spin-orbit-coupled bands, the intrinsic contribution seems to dominate the SHE and AHE. The calculations have given semiquantitative predictions of the expected spin Hall angles, particularly in metals. This is illustrated in the density-functional calculation for Pt (Guo *et al.*, 2008), shown in Fig. 8, and in the microscopic tight-binding calculations for other 4*d* and 5*d* metals (Tanaka *et al.*, 2008), shown in Fig. 9. As is clear from Fig. 8, the largest contributions to the spin Hall conductivity arise, similar to AHE, whenever bands connected via spin-orbit coupling are near each other at the Fermi energy. The calculated spin Hall conductivities are predicted to be large in these transition metals, and, in particular, a sign change is predicted going

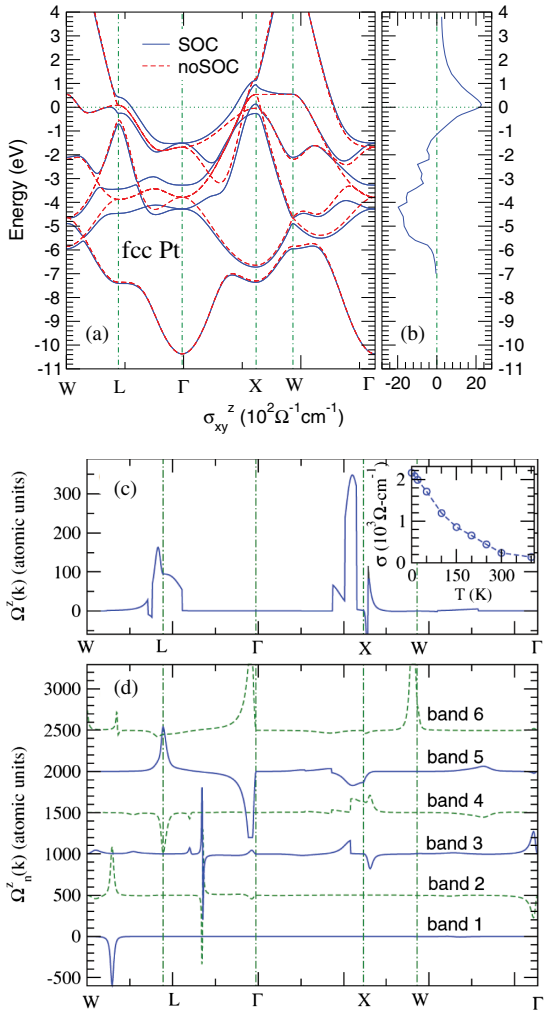

FIG. 8 (color online). Band structure (a) for Pt calculated with (solid lines) and without (dotted lines) spin-orbit coupling. The spin Hall conductivity (b) is shown calculated at each energy. In the lower figure, the Berry curvature is calculated (total) (c) as well as the one corresponding for each subband (d). From Guo *et al.*, 2008.

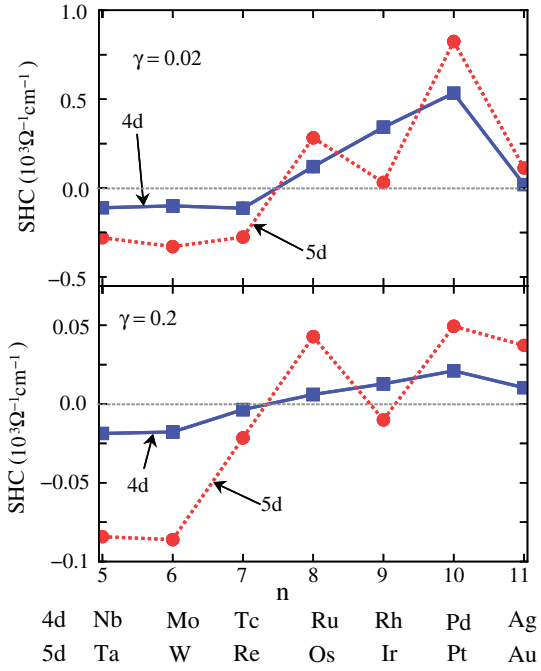

FIG. 9 (color online). Intrinsic spin Hall conductivity for 4*d* and 5*d* transition metals. A key feature is the change in sign from Pt to Ta. From Tanaka *et al.*, 2008.

from Pt to Ta which has been observed in experiments. More recent density-functional calculations on a range of hcp metals and antiferromagnetic Cr, show a strong anisotropy of the spin Hall conductivity (Freimuth, Blügel, and Mokrousov, 2010), as illustrated in Fig. 10.

2. Skew-scattering mechanism

The skew-scattering contribution to the SHE and the AHE is the mechanism proportional to the Bloch state transport lifetime τ. It will therefore tend to dominate in nearly perfect crystals. It is the only contribution to the SHE and AHE which appears in traditional Boltzmann transport theory where interband coherence effects are usually neglected. Skew scattering is due to chiral features which appear in the disorder scattering in the presence of spin-orbit coupling. This mechanism was first identified in FMs by Smit (1958) and has its origins in the Mott scattering in relativistic physics (Mott, 1929, 1932).

Typical treatments of semiclassical Boltzmann transport theory found in textbooks often appeal to the principle of detailed balance. This states that the transition probability $W_{n\to m}$ from state n to m is identical to the transition probability in the opposite direction ($W_{m\to n}$). In Fermi's golden-rule approximation, where $W_{n\to n'}=(2\pi/\hbar)|\langle n|V|n'\rangle|^2\delta(E_n-E_{n'})$, with V being the perturbation inducing the transition, the detailed balance indeed holds. However, detailed balance in the microscopic sense is not generic. In the presence of spin-orbit coupling, either in the Hamiltonian of the perfect crystal or in the disorder Hamiltonian, a transition which is right handed with respect to the magnetization direction has a different probability than the corresponding left-handed transition. When the transition rates are evaluated perturbatively, asymmetric chiral contributions appear at third order. In simple models, the

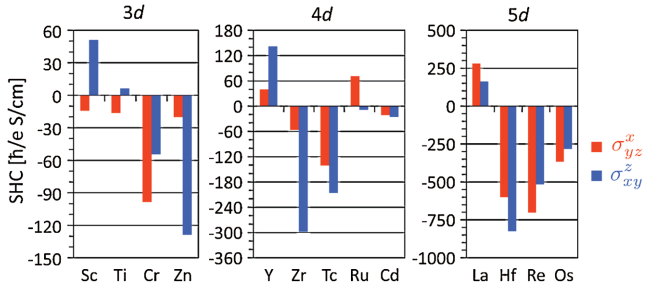

FIG. 10 (color online). Intrinsic spin Hall conductivity for hcp metals Sc, Ti, Zn, Y, Zr, Tc, Ru, Cd, La, Hf, Re, and Os and for antiferromagnetic Cr. From Freimuth, Blügel, and Mokrousov, 2010.

asymmetric chiral contribution to the transition probability of momenta $\mathbf{k}, \mathbf{k}'$ is often assumed to have the form

$$W^A_{\mathbf{k}\mathbf{k}'} \sim (\mathbf{k} \times \mathbf{k}') \cdot \mathbf{M}. \tag{3.7}$$

Inserting this asymmetry into the Boltzmann equation leads to a current proportional to the longitudinal current driven by the electric field $\mathbf{E}$ and perpendicular to both $\mathbf{E}$ and $\mathbf{M}$, where $\mathbf{M}$ is the magnetization direction in case of the AHE and the direction of the polarization of the spin current in case of the SHE. The corresponding contribution to the Hall conductivity $\sigma^{H-\text{skew}}_{xy}$ and the conductivity σ_{xx} are proportional to the transport lifetime τ. Therefore, the spin or anomalous Hall resistivity is proportional to the longitudinal resistivity ρ_{xx}, whenever this contribution dominates, since $\rho^{H-\text{skew}}_{xy} \approx \sigma^{H-\text{skew}}_{xy}\rho^2_{xx} \sim \rho_{xx}$.

There are several specific mechanisms for skew scattering [see Sec. IV.B and Sec. V.A. in Nagaosa *et al.* (2010)]. To evaluate the skew-scattering contribution to the Hall conductivity, one needs an accurate solution of the chiral part to the collision integral of Boltzmann equation. In practice, our ability to accurately estimate the skew-scattering contribution to the SHE and AHE of a real material is limited only by the accuracy of the characterization of its disorder.

In simple models, the skew-scattering contributions to the SHE or AHE are considered to arise only from the spin-orbit coupling in the disorder potential. This is only valid when the typical disorder broadening is larger than the splitting of the bands due to the spin-orbit coupling. In systems with strong spin-orbit coupling in the bands, such as heavy transition metals, considering the spin-orbit coupling only in the disorder potential would be incorrect. The reason is because, in this case, a strong contribution to the skew scattering also arises from the scattering of the spin-orbit-coupled quasiparticle from the scalar potential. In fact, the spin-orbit coupling of the disorder potential is typically strongly renormalized by the other nearby subbands as well, and therefore the effect of the multiband character can never be ignored in these materials.

Studies focused on the skew scattering from an *ab initio* perspective were started by Gradhand *et al.* (2010). Further recent studies of skew scattering based on *ab initio* electronic structure and the Boltzmann equation in systems with impurities of Cr, Mn, Fe, Co, and Ni in Pt, Au, and Pd hosts have yielded contributions to the spin Hall angle of a fraction of a percent (Long *et al.*, 2014; Zimmermann *et al.*, 2014). Results

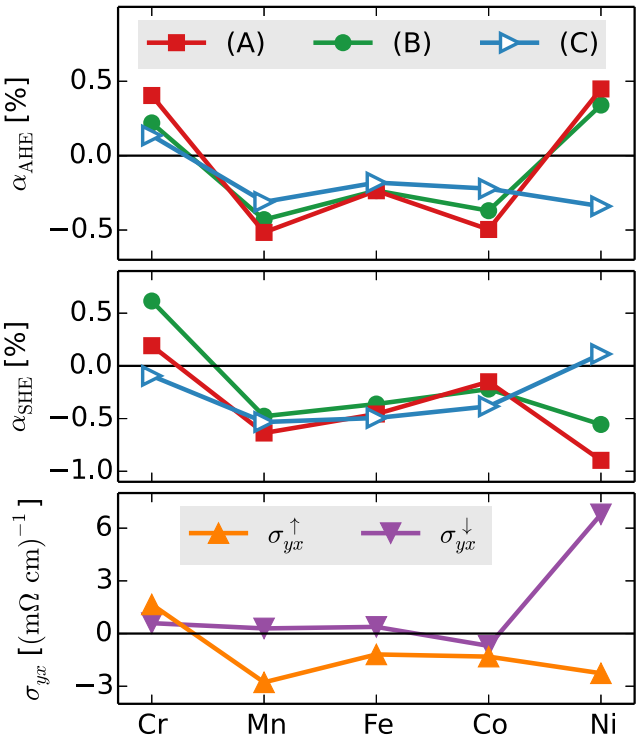

FIG. 11 (color online). Skew-scattering spin Hall angle in a Pt host with 1% level of impurities. From Zimmermann *et al.*, 2014.

related to 1% doping of impurities to a Pt host are shown in Fig. 11.

An additional contribution, not considered often, can arise from the variation of the spin-orbit coupling in real space. This possibility exists in certain semiconductor devices with 2D-Rashba spin-orbit coupling. Such variations have been shown to yield a contribution to the spin Hall effect in these 2D systems (Dugaev *et al.*, 2010).

We end this section with a note directed to the interested reader who is more versed in the latest development of the links between the full semiclassical and the microscopic theory of the SHE and AHE. We have been careful above not to define the skew-scattering contribution as the sum of all the contributions arising from the asymmetric scattering rate present in the collision term of the Boltzmann transport equation. We know from microscopic theory that this asymmetry also makes an AHE contribution of order τ^0 (Sinitsyn *et al.*, 2007). There exists a contribution from this asymmetry which is present in the microscopic theory treatment associated with the so-called ladder-diagram corrections to the conductivity, and therefore of order τ^0. In the more modern parsing of the contributions to the SHE and AHE, we do not associate this contribution with skew scattering but place it under the umbrella of side-jump scattering even though it does not physically originate from any side-step type of scattering.

3. Side-jump mechanism

Given the sharp definition we have provided for the intrinsic and skew-scattering contributions to the SHE and AHE conductivity, the equation

$$\sigma_{xy}^{H} = \sigma_{xy}^{H-\mathrm{int}} + \sigma_{xy}^{H-\mathrm{skew}} + \sigma_{xy}^{H-\mathrm{sj}} \tag{3.8}$$

defines unambiguously the side-jump contribution as the difference between the full SHE-AHE conductivity and the skew and intrinsic contributions. In using the term side jump for the remaining contribution, we are appealing to the historically established taxonomy outlined in the previous section. Establishing this connection rigorously has been the most controversial aspect of the AHE theory and, not surprisingly, some confusion has spilled over to the discussion of the SHE.

The basic semiclassical argument for a side-jump contribution can be stated straightforwardly: when considering the scattering of a Gaussian wave packet from a spherical impurity with spin-orbit interaction $[H_{\mathrm{so}}=(1/2m^2c^2)(r^{-1}\partial V/\partial r)S_zL_z]$, a wave packet with incident wave vector $\mathbf{k}$ will undergo a displacement transverse to $\mathbf{k}$ equal to $\frac{1}{6}k\hbar^2/m^2c^2$. This type of contribution was first noticed, but discarded, by Smit (1955, 1958) and reintroduced by Berger (1964) who argued that it was the key contribution to the AHE. Most of the earlier developments were based on physical arguments of how to incorporate this physics in a semiclassical Boltzmann formalism. Because this cannot be done systematically, errors ensued (Nagaosa *et al.*, 2010).

A common misconception is that the side jump can be generally computed by taking only into account the spin-orbit-coupling interaction of the disorder scattering potential. This can only be justified in a weak spin-orbit-coupled system, e.g., *n*-doped GaAs, where indeed this is likely to be the case. This is the consideration in the Crépieux-Bruno model (Crépieux and Bruno, 2001), where the spin-orbit coupling is only present in the disorder potential and which has been subsequently used by others to model the extrinsic SHE (Engel, Halperin, and Rashba, 2005; Maekawa and Takahashi, 2012). However, when addressing materials with strong spin-orbit coupling, it is important to remember that there are always two sources of side-jump scattering:

(1) Extrinsic side jump: the contribution arising from the non-spin-orbit-coupled part of the wave-packet scattering off the spin-orbit-coupled disorder.
(2) Intrinsic side jump: the contribution arising from the spin-orbit-coupled part of the wave packet formed by the Bloch electrons scattering off the scalar potential alone without spin-orbit coupling.

Both can be important and independent of each other, depending on the crystalline environment and the type of scattering impurity. In heavy-element materials, such as Pt and Ta, the dominant contribution is likely to be the second type of contribution. In FMs, it has been demonstrated that the second type of contribution, termed here *intrinsic side jump* to distinguish them clearly, can be very large. Both of these side-jump contributions add to the scattering-independent mechanisms, i.e., they are independent of τ (Weischenberg *et al.*, 2011).

The intrinsic SHE-AHE contribution and the side-jump contribution, which we further separated into the extrinsic side jump and the intrinsic side jump, have all quite different dependences on specific material parameters, particularly in systems with complex band structures. [For a detailed review on these delicate issues, see Sinitsyn (2008)]. Most of the prior mistakes surrounding the theory of side jump can be traced back to the physical meaning ascribed to quantities which were gauge dependent, like Berry's connection, which is typically identified as the definition of the side step upon scattering. Studies of simplified models, e.g., semiconductor conduction bands, also gave results in which the intrinsic-side-jump contribution seemed to be of the same magnitude but opposite in sign compared to the intrinsic contribution (Nozieres and Lewiner, 1973). It is well understood now that these cancellations are unlikely in more complex models (Sinitsyn *et al.*, 2007; Weischenberg *et al.*, 2011). The prior cancellations can be traced back to the fact that, in these very simple band structures, Berry's curvature of the Bloch electrons is a constant independent of momentum. One is reminded in this case of the famous quote attributed to Albert Einstein, "Things should be made as simple as possible but not simpler."

It is only through a careful comparison between different fully microscopic linear response theory calculations, based on equivalently valid microscopic formalisms such as Keldysh (nonequilibrium Green's function), the Kubo formalisms, and the systematically developed semiclassical theory, that the specific contributions due to the side-jump mechanism can be identified with confidence (Sinitsyn *et al.*, 2007; Nagaosa *et al.*, 2010).

Recently, there have been major steps forward in the theory of the AHE in developing full theories with predictive power to calculate all the AHE contributions in FM materials with a complex band structure (Freimuth, Blügel, and Mokrousov, 2010; Kovalev, Sinova, and Tserkovnyak, 2010; Lowitzer, Ködderitzsch, and Ebert, 2010; Weischenberg *et al.*, 2011; Czaja *et al.*, 2014). In the theory of the SHE, on the other hand, such progress still remains to be undertaken fully. The reason is perhaps because of the complexity of the measurements, the dephasing of spin, and the lack of practical general theories that can bring one from a weak to a strong spin-orbit-coupled regime.

4. Cancellation of mechanisms in model systems

We mentioned earlier that in certain simplified models there exist relative cancellations, either total or partial, between the contributions that depend to zeroth order on the scattering lifetime. This is a topic that has entertained the research community of the AHE and the SHE for quite some time.

The reader familiar with the early history of the AHE and with the early history of the intrinsic SHE will have seen many works debating these issues. Some simplified models that allow for an analytical treatment show such cancellations. The two key ones are the linear wave vector 2D Rashba model (with parabolic dispersion) and the direct gap conduction band III-V semiconductor model (Kane model).

In the 2D Rashba model, the intrinsic contribution and the intrinsic-side-jump contribution cancel each other directly in the presence of short-range disorder scattering. The easiest way to see this is by noticing that the spin dynamics is directly proportional in this model to the spin current generated. Therefore, in the steady state, the spin current must vanish (Inoue, Bauer, and Molenkamp, 2004; Dimitrova, 2005;

Shytov *et al.*, 2006; Sinova *et al.*, 2006). For an extensive discussion of the issues of this particular model, see Raimondi *et al.* (2012). When one incorporates to the model higher dimensions or a nonparabolic dispersion, such cancellations do not occur. For example, a graphene-like model (linear dispersion) does not exhibit such cancellations and provides a useful model to study the relative dependence of the mechanisms (Sinitsyn *et al.*, 2007).

Also, as mentioned, another extensively studied model is the Kane model (Nozieres and Lewiner, 1973). In this model, the relative cancellation is a 2 to 1 ratio. The fact that the intrinsic contribution and the intrinsic-side-jump contribution have the same dependence on the parameters (up to the factor of -2) can be traced back to Berry's curvature being constant (independent of momentum) in such a model.

For most other spin-orbit-coupled Hamiltonians, corresponding to a realistic materials system, these exact cancellations do not seem to arise. This has been verified primarily by comparison to experiments. Nevertheless, this remains an important topic in the SHE field which will continue to be refined as better approximations are created to treat the effects of disorder.

B. Phenomenological drift-diffusion theory

Dyakonov and Perel (1971a, 1971b) considered the phenomenological theory of the SHE by coupling the usual drift-diffusion equation for charge transport to the spin-current drift-diffusion equations. Hence, the spin-charge drift-diffusion equations applicable to electrical transport measurements can be written from symmetry considerations as (Dyakonov and Khaetskii, 2008)

$$\mathbf{j}^c = e\mu n\mathbf{E} + D\nabla n + e\alpha_{\mathrm{SH}}\mu(\mathbf{E}\times\mathbf{P}) + e\alpha_{\mathrm{SH}}D(\nabla\times\mathbf{P}), \quad (3.9)$$

$$\mathbf{j}^s_{ij} = -\hbar\mu n E_i P_j + D\frac{\partial P_j}{\partial x_i} - \hbar\alpha_{\mathrm{SH}}\epsilon_{ijk}\left(\mu n E_k + D\frac{\partial n}{\partial x_k}\right), \quad (3.10)$$

where the first two terms of Eqs. (3.9) and (3.10) correspond to the definition of the uncoupled charge and spin currents. Here $\mathbf{P}$ corresponds to the spin polarization, D is the electron diffusion constant, μ is the spin-independent electron mobility, n is the electron density, $\mathbf{E}$ is the electric field, and α_{SH} is the spin Hall angle defined by the ratio of the spin Hall conductivity to the diagonal charge conductivity.

In Eq. (3.9), the third term corresponds to the AHE. The fourth term describes the ISHE if a charged diffusive current is absent, i.e., in the case of the pure spin current in the system. We distinguish this from the situation in which a polarized charge diffusive current, e.g., generated by optical excitation (Bakun *et al.*, 1984), leads to a charge transverse current which we associate here with a regime closer to the AHE. This distinction is made more clear by the fact that the SHE has a precise definition of a pure spin current being generated by a charge current, and therefore its inverse is associated with a pure spin current generating a transverse charge current. In Eq. (3.10), the third term represents the SHE from an electric field, while the fourth term represents its diffusion-driven counterpart. The equations are written to first order in the spin Hall angle.

Equations (3.9) and (3.10) can be directly extended to include junctions (Johnson and Silsbee, 1987). Recently, there has been also an extension of these equations to incorporate thermal SHEs within the emerging field of spin caloritronics (Bauer, MacDonald, and Maekawa, 2010; Bauer, Saitoh, and van Wees, 2012). The treatment, for the most part, remains phenomenological with connections, in particular, to the Onsager relations between the thermodynamic forces and their corresponding entropy fluxes. Within this emerging subfield of spintronics, many theoretical challenges remain, not least a better treatment of scattering coherent effects driven by statistical forces and the ability of going beyond the simple adiabatic frozen phonon approximations.

A connection has also been made between the diffusion regime treated by the above equations and the microscopic treatment considering the specific boundary conditions in 2D Rashba systems (Adagideli and Bauer, 2005). In this case, the spin accumulation at the edges remains in a diffusive system even though no spin current exists in the bulk for this model. The results are also relevant when connecting the drift-diffusion equations to the indirect detection of the SHE by ferromagnetic contacts (Adagideli, Bauer, and Halperin, 2006).

C. Crépieux-Bruno model of extrinsic side jump and skew scattering

We discuss here the Crépieux and Bruno (2001) model that incorporates spin-orbit coupling only through the disorder potential, i.e., there is no spin-orbit coupling present directly in the Bloch electron bands at the Fermi surface. This model has been applied to weak spin-orbit-coupled materials, such as *n*-GaAs, to explain the extrinsic origin of their SHE (Engel, Halperin, and Rashba, 2005), schematically illustrated in Fig. 12, and has also been applied to weakly spin-orbit-coupled metals (Maekawa and Takahashi, 2012). The model builds on the influential work of Nozieres and Lewiner (1973), where they studied the AHE in semiconductors with a simple band structure. In particular, they focused on how to account for the effects of the spin-orbit coupling by projecting multiband systems to an effective two-band model. There are many subtle issues in such treatment already at the level of this simple model. However, extrapolating some of its results to generalities, e.g., specific cancellations, is dangerous since

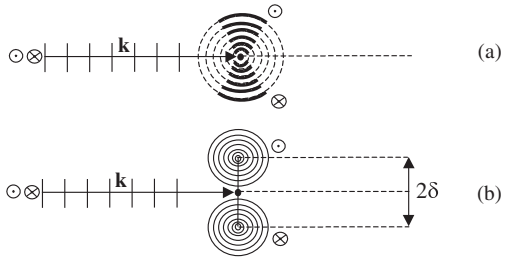

FIG. 12. Schematic of the (a) skew-scattering and the (b) extrinsic-side-jump mechanisms from a quantum point of view (⊙ corresponds to spin up and ⊗ to spin down). The bold curves represent the anisotropic enhancement of the amplitude of the wave packet due to spin-orbit coupling. Here the electrons themselves contain no spin-orbit coupling. From Crépieux and Bruno, 2001.

"the side-jump is no longer given by the simple expression" derived in these works, as they themselves state (Nozieres and Lewiner, 1973).

The two-band model Hamiltonian is given by

$$H = \frac{\hbar^2 k^2}{2m^*} + V(\mathbf{r}) + \lambda_{e-\mathrm{so}}\sigma \cdot (\mathbf{k} \times \nabla V) = H_0 + W. \quad (3.11)$$

Here m^* is the effective mass of the Bloch electron, $V(\mathbf{r})$ is the disorder potential, σ are the Pauli matrices, and $\lambda_{e-\mathrm{so}}$ is the effective spin-orbit coupling parameter. For a free electron, $\lambda_{e-\mathrm{so}}^2 = \hbar^2/2m^2c^2$ is an extremely small parameter ($\sim 10^{-12}$ Å^2), but in a solid-state environment it is strongly renormalized by nearby bands. For the effective two-band model of conduction electrons, obtained from the 8×8 Kane description of the semiconductor band structure, $\lambda_{e-\mathrm{so}} = (P^2/3)[1/E_g^2 - 1/(E_g + \Delta_{\mathrm{so}})]$, with E_g being the gap, P the s-p dipole matrix element, and Δ_{so} the spin-orbit splitting of the valence band. For n-GaAs, for example, this value is 5.3 Å^2. The total scattering potential is W.

In this model, the velocity operator is modified by the spin-orbit-coupled term to read

$$\hat{\mathbf{v}} = \frac{\hat{\mathbf{p}}}{m^*} + \frac{\lambda_{e-\mathrm{so}}}{\hbar}[\sigma \times \nabla V], \quad (3.12)$$

and the scattering amplitude due to the disorder potential from state $|\mathbf{k}, s\rangle$ to $|\mathbf{k}', s'\rangle$ is given by

$$\langle k', s'|W|k, s\rangle = \tilde{V}_{\mathbf{k}\mathbf{k}'}[\delta_{ss'} + i\lambda_{e-\mathrm{so}}(\boldsymbol{\sigma}_{s's} \times \mathbf{k}') \cdot \mathbf{k}], \quad (3.13)$$

where $\tilde{V}_{\mathbf{k}\mathbf{k}'}$ is the Fourier transform of V. The disorder potential is considered to be short ranged for simplicity [for ionic scattering, see Engel, Halperin, and Rashba (2005)] such that $V(\mathbf{r}) = u_i \sum_j \delta(\mathbf{r} - \mathbf{r}_j)$ and $\tilde{V}_{\mathbf{k}\mathbf{k}'} = u_i \delta_{\mathbf{k},\mathbf{k}'}$. One can then connect this procedure with the Boltzmann equation, which will also yield the spin-diffusion equation (Zhang, 2000). Microscopically, the scattering from this disorder potential induces a collision integral in the Boltzmann formalism of the form

$$\left(\frac{\partial f_{\mathbf{k},s}}{\partial t}\right)_{\mathrm{coll}} = \sum_{\mathbf{k}',s'}[P_{\mathbf{k}s,\mathbf{k}'s'} f_{\mathbf{k}'s'} - P_{\mathbf{k}'s',\mathbf{k}s} f_{\mathbf{k}s}], \quad (3.14)$$

with the transition scattering probabilities available from the T matrix, which yields a symmetric and antisymmetric contribution,

$$P^{\mathrm{sym}}_{\mathbf{k}'s',\mathbf{k}s} = \frac{2\pi n_i}{\hbar}\frac{}{V} u_i^2[\delta_{s,s'} + \lambda_{e-\mathrm{so}}^2 |(\mathbf{k}' \times \mathbf{k}) \cdot \sigma_{s,s'}]\delta(\epsilon_{\mathbf{k}'} - \epsilon_{\mathbf{k}}), \quad (3.15)$$

$$P^{\mathrm{ant}}_{\mathbf{k}'s',\mathbf{k}s} = -\frac{(2\pi)^2}{\hbar}\lambda_{e-\mathrm{so}}\frac{n_i}{V}u_i^3[N(0)\delta_{s,s'}(\mathbf{k}' \times \mathbf{k}) \cdot \sigma_{s,s'}] \times \delta(\epsilon_{\mathbf{k}'} - \epsilon_{\mathbf{k}}). \quad (3.16)$$

Here, n_i is the density of impurities and $N(0)$ is the density of states at the Fermi level. Within the framework of the semiclassical Boltzmann equation, one then writes (Zhang, 2000; Maekawa and Takahashi, 2012)

$$\mathbf{v}_{\mathbf{k}} \cdot \boldsymbol{\nabla} f_{\mathbf{k}s} + \frac{e\mathbf{E}}{\hbar} \cdot \nabla_{\mathbf{k}} f_{\mathbf{k}s} = -\frac{\delta f_{\mathbf{k}s}}{\tau_{\mathrm{tr}}} - \frac{f^0_{\mathbf{k}s} - f^0_{\mathbf{k}'s}}{\tau_{\mathrm{sf}}(\theta)}, \quad (3.17)$$

where

$$\tau_{\mathrm{tr}}^{-1} = \sum_{\mathbf{k}',s'} P^{\mathrm{sym}}_{\mathbf{k}s,\mathbf{k}'s'} = \frac{1}{\tau^0_{\mathrm{tr}}}(1 + 2k_F^4\lambda_{e-\mathrm{so}}^2/3) \quad (3.18)$$

and

$$\tau_{\mathrm{sf}}^{-1} = \sum_{\mathbf{k}'} P^{\mathrm{sym}}_{\mathbf{k}1,\mathbf{k}'-1} = \frac{k_F^4\lambda_{e-\mathrm{so}}^2}{3\tau^0_{\mathrm{tr}}}[1 + \cos^2(\theta)]. \quad (3.19)$$

Here τ_{tr} is the transport lifetime, τ^0_{tr} is the transport lifetime when neglecting the spin-orbit coupling part of the disorder potential, and τ_{sf} is the spin-flip time. Further expanding the equilibrium and nonequilibrium distribution functions yields the spin-diffusion equation,

$$\nabla^2(\mu_1 - \mu_{-1}) = \frac{1}{\lambda_{\mathrm{sd}}^2}(\mu_1 - \mu_{-1}), \quad (3.20)$$

with $\lambda_{\mathrm{sd}}^2 = D\tau_{\mathrm{sf}}/2$, $D = (1/3)\tau_{\mathrm{tr}}v_F^2$, and μ_s representing the spin-dependent chemical potentials ($s = \pm 1$ is the spin index). Averaging over the scattering angle, one obtains that the ratio of spin-flip time and transport time for this particular model is

$$\frac{\tau_{\mathrm{tr}}}{\tau_{\mathrm{sf}}} \approx \frac{1}{2}k_F^4\lambda_{e-\mathrm{so}}^2. \quad (3.21)$$

This is one of the key aspects that has made this model appealing. The model provides a means to obtain its effective spin-orbit-coupling parameter $\lambda_{e-\mathrm{so}}$ by measuring the spin-diffusion length, independently of the spin Hall angle. At this point, it should be emphasized that the model is applicable to the weak spin-orbit-coupling regime, i.e., when $\tau_{\mathrm{tr}}/\tau_{\mathrm{sf}} \ll 1$.

From either a microscopic or Boltzmann-like analysis, the result for this model for the extrinsic-side-jump contribution to the spin Hall angle is (Crépieux and Bruno, 2001; Engel, Halperin, and Rashba, 2005)

$$\alpha^{\mathrm{sj}}_{\mathrm{SH}} \equiv \frac{\sigma^{H-\mathrm{sj}}_{xy}}{\sigma_{xx}} = -\frac{2\lambda_{e-\mathrm{so}}m^*}{\tau_{\mathrm{tr}}} = -\frac{2k_F^2\lambda_{e-\mathrm{so}}}{k_F l}. \quad (3.22)$$

Here, $l = \tau_{\mathrm{tr}}k_F/m^*$ is the mean free path. The skew-scattering contribution is given by

$$\alpha^{\mathrm{sk}}_{\mathrm{SH}} = \frac{4\pi}{3}k_F^2\lambda_{e-\mathrm{so}}N(0)u_i. \quad (3.23)$$

In the SHE experiments in n-GaAs, the spin Hall angle is dominated by the skew-scattering contribution versus the extrinsic-side-jump contribution by a factor of 2, $\sigma^{H-\mathrm{skew}}_{xy}/\sigma^{H-\mathrm{sj}}_{xy} \sim -1.7/0.8$ (Engel, Halperin, and Rashba, 2005).

When this simplified model is used for metals, it yields a mixture of results and inconsistencies. This can be seen in Table I, where we show for a series of metals the experimental SHE angles and the independently experimentally inferred

TABLE I. Experimental spin Hall angles and effective spin-orbit-coupling parameters, $k_F^2\lambda_{e-\mathrm{so}}$. The values marked by an asterisk are not measured but taken from the literature. The Fermi momenta are taken to be $k_F = 1.75 \times 10^8$ cm^{-1} (Al), 1.21×10^8 cm^{-1} (Au), 1.18×10^8 cm^{-1} (Nb), and 1.0×10^8 cm^{-1} (Mo, Pd, Ta, Pt). Here, $k_F l = (3\pi/2)\sigma/k_F(h/e^2)$. References: (1) Valenzuela and Tinkham (2006, 2007); (2) Seki *et al.* (2008); (3) Mosendz *et al.* (2010b); (4) Niimi *et al.* (2011); (5) Morota *et al.* (2009); (6) Morota *et al.* (2011); (7) Ando and Saitoh (2010); (8) Kimura *et al.* (2007); (9) Vila, Kimura, and Otani (2007); (10) Ando *et al.* (2008); and (11) Liu *et al.* (2011).

	λ_{sd} (nm)	$k_F l$	$k_F^2\lambda_{e-\mathrm{so}}$	α_{SH} (%)	$\lvert\alpha_{\mathrm{SH}}^{\mathrm{sj}}/\alpha_{\mathrm{SH}}\rvert$	Refs. (see caption)
Al (4.2 K)	455 ± 15	73	0.0079	0.032 ± 0.006	0.67	1 NL
Al (4.2 K)	705 ± 30	118	0.0083	0.016 ± 0.004	0.88	1 NL
Au (295 K)	86 ± 10	371	0.3	11.3	0.014	2 NL
Au (295 K)	$35 \pm 3^*$	253	0.52	0.35 ± 0.03	1.17	3 SP
CuIr (10 K)	5–30			2.1 ± 0.6		4 NL
Mo (10 K)	10	36.8	0.32	-0.20	8.7	5 NL
Mo (10 K)	10	8.11	0.07	-0.075	23	5 NL
Mo (10 K)	8.6 ± 1.3	34.1	0.34	$-(0.8 \pm 0.18)$	2.5	6 NL
Mo (295 K)	$35 \pm 3^*$	56.7	0.14	$-(0.05 \pm 0.01)$	9.9	3 SP
Nb (10 K)	5.9 ± 0.3	11.3	0.14	$-(0.87 \pm 0.20)$	2.9	6 NL
Pd (295 K)	9^*	24.0	0.23	1.0	1.9	7 SP
Pd (10 K)	13 ± 2	26.8	0.18	1.2 ± 0.4	1.1	6 NL
Pd (295 K)	$15 \pm 4^*$	48.6	0.28	0.64 ± 0.10	1.8	3 SP
Pt (295 K)		77.9	0.74	0.37	5.1	8 NL
Pt (5 K)	14	97.3	0.61	0.44	2.9	9 NL
Pt (295 K)	10	67.6	0.58	0.9	1.9	9 NL
Pt (10 K)	11 ± 2	98.5	0.77	2.1 ± 0.5	0.74	5 NL
Pt (295 K)	7^*	77.8	0.97	8.0	0.31	10 SP
Pt (295 K)	3–6	60.8	0.88–1.75	$7.6^{+8.4}_{-2.0}$	0.57	11 SP
Pt (295 K)	$10 \pm 2^*$	29.2	0.25	1.3 ± 0.2	1.31	3 SP
Ta (10 K)	2.7 ± 0.4	3.90	0.17	$-(0.37 \pm 0.11)$	24	6 NL

effective spin-orbit-coupling parameters $k_F^2\lambda_{e-\mathrm{so}}$. It is not possible to estimate the skew scattering from the model expression (3.23) without knowing the specific value for u_i. However, we know from the AHE that skew scattering has only been seen to dominate for extremely conductive metals, so it is neglected in the discussion of Table I. When comparing the extrinsic-side-jump contribution estimates to the measured values of α_{SH}, the results vary extensively. In some cases, like Ta, the theoretical extrinsic-side-jump contribution is 24 times larger than the measured α_{SH}. The failure of Eq. (3.22) is not surprising here, since it was derived assuming the weak spin-orbit-coupling regime and Ta is a $5d$ heavy transition metal. In others, like in Pt, Eq. (3.22) gives a value that is smaller than the measured α_{SH}, in some cases approaching the experimental value. However, even in this case, ascribing the measured spin Hall angle to the extrinsic-side-jump contribution of Eq. (3.22) is questionable because the independently inferred parameter $k_F^2\lambda_{e-\mathrm{so}}$ is close to 1. This is inconsistent with $\tau_{\mathrm{tr}}/\tau_{\mathrm{sf}} \ll 1$, i.e., with the weak spin-orbit-coupling regime assumed in the model. In the heavy-element materials, the intrinsic SHE estimates have had much more success. Hence, the simple expression arising from the model [see Eq. (3.22)], although illustrative and appealing, should only be considered as such, not as a quantitative predictive theory of the SHE.

Beyond this simplified model based on the spin-orbit coupling scattering which ignores interband coherent effects in strongly spin-orbit-coupled metals, an even more simplified model was put forward based a classical treatment (Drude model) of the equations of motions of the Bloch electrons (Chudnovsky, 2007, 2009). For a cubic crystal it predicts a spin Hall angle of $h\sigma_{xx}/2mc^2$ which disagrees with experimental observations (Hoffmann, 2013a). Although the theory has also been questioned (Kravchenko, 2008; Chudnovsky, 2009), it is nonetheless popular, particularly in the treatment of the spin-motive force in ferromagnetic systems. The symmetry being built directly into the theory, it will always give a parameter to which experiment can be fitted, similar to the model presented.

D. Theory of the inverse spin Hall effect induced by spin pumping

To measure the ISHE, it is necessary to generate a spin current that flows into the NM whose spin Hall angle is being measured. In the nonlocal transport schemes, this is achieved indirectly by spin diffusion into the NM.

A key alternative to generating spin currents is to exploit SP in a FM-NM bilayer system. This phenomenon was observed experimentally in early 2000s (Mizukami, Ando, and Miyazaki, 2001, 2002; Urban, Woltersdorf, and Heinrich, 2001). The experiments showed an enhanced Gilbert damping in FMR measurements associated with the loss of angular momentum by a spin current flowing from the FM to the NM. In this setup, the NM served as a spin sink.

The associated SP theory based on the scattering formalism was developed by Tserkovnyak, Brataas, and Bauer (2002a, 2002b) and Tserkovnyak, Brataas, and Halperin (2005). It extends the theory of adiabatic quantum pumping (Büttiker, Thomas, and Prêtre, 1993; Brouwer, 1998) by incorporating the spin degrees of freedom. It can be shown that the precessing magnetization in the FM generates a time-dependent spin current at the FM-NM interface that flows into the NM given by

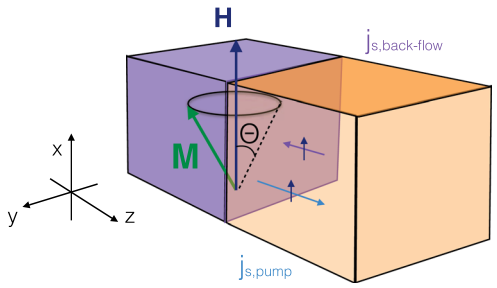

FIG. 13 (color online). Schematic of SP comprising a spin-pump current flowing from the FM to the NM and a backflow current that depends on the thickness of the NM.

$$j_{s,\mathrm{pump}}\boldsymbol{\sigma}(t) = \frac{\hbar}{4\pi} A_r \hat{\mathbf{m}} \times \frac{d\hat{\mathbf{m}}}{dt}. \tag{3.24}$$

Here $\hat{\mathbf{m}}(t)$ is the unit vector of the magnetization, $\boldsymbol{\sigma}$ is the unit vector of the spin-current polarization, $j_{s,\mathrm{pump}}$ its magnitude, and A_r is defined as the SP conductance of the particular sample. The spin current generated at the interface which propagates into the NM decays on a length scale connected to the effective spin-diffusion length λ_{sd} of the NM. A sketch of the physics is shown in Fig. 13. Note that in systems with strong spin-orbit coupling, this length scale can be difficult to define since it can be as short as several atomic layers. Also, proximity effects as well as roughness at the interface with the NM can blur the sharpness of such an interface.

The scattering-matrix theory introduces the concept of a complex spin-mixing conductance at the interface based on spin-conserving channels and no spin losses at the interface. Theoretical *ab initio* calculations and phase randomization at the scattering interface seem to indicate that only the real part of the mixing conductance dominates the physics. In the diffusive regime, this will be approximately the Sharvin conductance given by the number of conducting channels. In this approximation (Tserkovnyak, Brataas, and Bauer, 2002b),

$$A_r \approx \mathrm{Re}[g^{\uparrow\downarrow}] = \frac{k_F^2}{4\pi} \approx \frac{1}{4\pi}(3\pi^2 n)^{2/3}, \tag{3.25}$$

where k_F and n are the Fermi wave vector and electron density in the NM, respectively. Direct *ab initio* calculations of the mixing conductance (Xia *et al.*, 2002; Zwierzycki *et al.*, 2005; Carva and Turek, 2007) have verified that, for a FM-NM interface with moderate spin-orbit coupling, the spin-mixing conductance is of this order of magnitude.

As the magnetization rotates, the spin current injected from the FM into the NM is time dependent, but the ac spin current when averaged over time has a nonzero dc component, which is given by

$$j_{s,\mathrm{dc}} = \frac{\hbar\omega}{4\pi} A_r \sin^2\Theta. \tag{3.26}$$

Here ω is the driving radio frequency (rf) and Θ is the cone angle of precession (see Fig. 13). Under the assumption of the NM being a perfect spin sink, the SP conductance will be the spin-mixing conductance. However, in systems where the NM has a finite thickness of the order of the spin-diffusion length, the induced spin accumulation in the NM due to the pumped spin current from the FM will create a spin accumulation, which in turn will generate a spin-current backflow (Tserkovnyak, Brataas, and Bauer, 2002a; Costache, Sladkov, van der Wal, van Wees, 2006; Wang *et al.*, 2006). The spin accumulation in the NM within the spin-diffusive regime $\mu_s \equiv \mu_\uparrow - \mu_\downarrow$ is governed by

$$\frac{d\mu_s}{dt} = D\partial_z^2\mu_s - \frac{\mu_s}{\tau_{\mathrm{sf}}}, \tag{3.27}$$

with the boundary conditions

$$\begin{aligned} z = 0&: \ \partial_z\mu_s = -\frac{4e^2\rho}{\hbar} j_{s,0}, \\ z = t_{\mathrm{NM}}&: \ \partial_z\mu_s = 0, \end{aligned} \tag{3.28}$$

where ρ is the NM resistance and t_{NM} is the thickness of the NM. In the NM, the spin current decays away from the FM-NM interface due to the combination of spin-diffusion and spin-flip scattering. The z-dependent spin-current density $j_s(z)$ in the NM (Mosendz, Pearson *et al.*, 2010; Azevedo *et al.*, 2011) with the above boundary conditions reads

$$j_s(z) = -\frac{\hbar}{4e^2\rho}\partial_z\mu_s(z) = j_{s,0}\frac{\sinh\left[(t_{\mathrm{NM}} - z)/\lambda_{\mathrm{sd}}\right]}{\sinh\left(t_{\mathrm{NM}}/\lambda_{\mathrm{sd}}\right)}. \tag{3.29}$$

The backflow current density $j_{s,\mathrm{back}}$ at the interface can be taken into account with $j_{s,\mathrm{back}}(0) \approx 2\mathrm{Re}[g^{\uparrow\downarrow}]\mu_s(0)$. This allows the following expression to be solved for the total spin current crossing the interface:

$$j_{s,0}\boldsymbol{\sigma}(t) = (j_{s,\mathrm{pump}} - j_{s,\mathrm{back}})\boldsymbol{\sigma}(t) = \frac{\hbar}{4\pi}\tilde{A}_r \hat{\mathbf{m}} \times \frac{d\hat{\mathbf{m}}}{dt}. \tag{3.30}$$

The result is that the effective spin-mixing conductance gets reduced due to a backflow factor given by (Tserkovnyak, Brataas, and Bauer, 2002b)

$$\beta \equiv \frac{\tau_{\mathrm{sf}}\delta_{\mathrm{sd}}/h}{\tanh\left(t_{\mathrm{NM}}/\lambda_{\mathrm{sd}}\right)}, \tag{3.31}$$

where δ_{sd} is an effective spin-flip scattering energy obtained by the inverse of the product of the volume defined by the scattering cross section and spin-diffusion length and the density of states. This then gives the result (Tserkovnyak, Brataas, and Bauer, 2002b)

$$\tilde{A}_r \approx g^{\uparrow\downarrow}\frac{1}{1 + \beta g^{\uparrow\downarrow}}, \tag{3.32}$$

$$\tilde{A}_r \approx g^{\uparrow\downarrow}\frac{1}{1 + 1/4\sqrt{\frac{e}{3}}\tanh\left(t_{\mathrm{NM}}/\lambda_{\mathrm{sd}}\right)} \approx g_{\mathrm{eff}}^{\uparrow\downarrow}, \tag{3.33}$$

where $g^{\uparrow\downarrow}$ is now the real part of the spin-mixing conductance. The last approximation assumes a weak spin-orbit-coupling

limit. More explicitly, it assumes $\epsilon = \tau_{\rm tr}/\tau_{\rm sf} \ll 1$ (see Sec. III.C). Hence, the larger ϵ, the more efficiently the injected spin current is relaxed in the NM and the smaller is the amount of backflow (Tserkovnyak, Brataas, and Bauer, 2002b). However, one has to be aware of the limitations of the approximation since in the strongly spin-orbit-coupled systems many of these assumptions fail.

The detection of the net spin current flowing into the NM can be done electrically via the ISHE, as was demonstrated by Saitoh *et al.* (2006). Earlier experiments by Azevedo *et al.* (2005) showed similar results in trilayer FM-NM-FM thin films, although they were not identified with the ISHE. By measuring the Hall voltage induced by the spin current, one can infer the spin Hall angle of the material,

$$\mathbf{j}_c = \alpha_{\rm SH}\frac{2e}{\hbar}\mathbf{j}_s \times \boldsymbol{\sigma}(t). \tag{3.34}$$

Here the vector of the spin-current density $\mathbf{j}_s$ points perpendicular to the NM-FM interface. Note that the vector of the spin current polarization $\boldsymbol{\sigma}(t)$ is a time varying quantity. In the geometry sketched in Fig. 13 the propagation direction of the spin current is along z and its polarization is along the x axis. For the detection of a dc voltage along the y direction, one has to consider the charge current

$$j_c\hat{y} = \alpha_{\rm SH}\frac{2e}{\hbar}(1/t_{\rm NM})\int_0^{t_{\rm NM}} j_s(z)\hat{z}\times\hat{x}$$

with magnitude (Azevedo *et al.*, 2011)

$$j_c = \alpha_{\rm SH}\frac{2e}{\hbar}j_{s,0}\frac{\lambda_{\rm sd}}{t_{\rm NM}}\tanh\left(\frac{t_{\rm NM}}{2\lambda_{\rm sd}}\right). \tag{3.35}$$

To convert this charge current density into the actual measured voltage, one has to take into account the details of the measurement geometry and the resistivity of the bilayer. This will be discussed in Sec. IV.D. In addition, as described as well in Sec. IV.D, the ac component can be directly measured. An extension of the above theory to incorporate the ac component has been done by Jiao and Bauer (2013), with the result that backflow is important to distinguish between the measured voltages for both the ac and dc configurations.

We conclude this section with a discussion regarding the assumptions of the SP theory. In the derivations, whenever $\epsilon \sim 1$, the approximations do not hold anymore since for the given boundary conditions and for the use of the spin-diffusion equation (and the spin-resolved spin-mixing conductance) one assumes $\epsilon \ll 1$ (Tserkovnyak, Brataas, and Bauer, 2002b). However, for $\epsilon > 0.1$, most of the spin scattering occurs right at the interface and consequently the films are almost perfect sinks. Hence, in this case there is no dependence on the thickness of the film. Since in such films the interface plays the prominent role and scattering occurs at or near the interface, many issues regarding proximity effects, the induced spin-accumulation, and the spin Hall angle inferred from the measurements should be taken as phenomenological parameters rather than direct connections to a quantitative value of the bulk spin Hall angles.

E. Kubo formalism

The Kubo formalism provides a fully quantum-mechanical formally exact expression for the spin and anomalous Hall conductivity in linear response theory (Mahan, 2000). In this section, we review how it is employed in the calculations of the intrinsic SHE. The key approximation within the formalism is how disorder is treated. For most studies, it is incorporated through a simple finite quasiparticle lifetime, but can also have more sophisticated treatments, such as coherent potential approximations when treating metal alloys. Here we emphasize the key issues in studying the SHE within this formalism and how it relates to the semiclassical formalism described in the previous sections.

For the purpose of studying the SHE and AHE, it is best to reformulate the current-current Kubo formula for the conductivity in the form of the Bastin formula [see Appendix A in Crépieux and Bruno (2001)], which can be manipulated into the more familiar form for the conductivity of the Kubo-Streda formula for the zero-temperature Hall conductivity, $\sigma_{xy}^{H} = \sigma_{xy}^{I(a)} + \sigma_{xy}^{I(b)} + \sigma_{xy}^{II}$, where

$$\sigma_{xy}^{I(a)} = \frac{e^2}{2\pi V}{\rm Tr}\langle\{\hat{s}_z,\hat{v}\}_x G^R(\epsilon_F)\hat{v}_y G^A(\epsilon_F)\rangle_c, \tag{3.36}$$

$$\sigma_{xy}^{I(b)} = -\frac{e^2}{4\pi V}{\rm Tr}\langle\{\hat{s}_z,\hat{v}\}_x G^R(\epsilon_F)\hat{v}_y G^R(\epsilon_F) + {\rm c.c.}\rangle_c, \tag{3.37}$$

$$\sigma_{xy}^{II} = \frac{e^2}{4\pi V}\int_{-\infty}^{+\infty} d\epsilon f(\epsilon){\rm Tr}\left[\{\hat{s}_z,\hat{v}\}_x G^R(\epsilon)v_y\frac{G^R(\epsilon)}{d\epsilon} - \{\hat{s}_z,\hat{v}\}_x\frac{G^R(\epsilon)}{d\epsilon}v_y G^R(\epsilon) + {\rm c.c.}\right]. \tag{3.38}$$

Here the subscript c indicates a disorder configuration average. The last contribution σ_{xy}^{II} was originally derived by Streda in the context of the QHE (Streda, 1982). In these equations $G^{R/A}(\epsilon_F) = (\epsilon_F - H \pm i\delta)^{-1}$ are the retarded and advanced Green's functions evaluated at the Fermi energy of the total Hamiltonian.

Looking more closely at σ_{xy}^{II} we notice that every term depends on products of retarded Green's functions only, or on products of advanced Green's functions only. It can be shown that only the disorder free part of σ_{xy}^{II} is important in the weak disorder limit, i.e., this contribution is zeroth order in the parameter $1/k_F l$. The only effect of disorder on this contribution (for metals) is to broaden the Green's functions (see below) through the introduction of a finite lifetime (Sinitsyn *et al.*, 2007). By a similar argument, σ_{xy}^{Ib} is of order $1/k_F l$ and can be neglected in the weak scattering limit (Mahan, 2000). Thus, important disorder effects beyond a simple quasiparticle lifetime broadening are contained only in σ_{xy}^{Ia}. For these reasons, it is standard within the Kubo formalism to neglect σ_{xy}^{Ib} and evaluate the σ_{xy}^{II} contribution with a simple lifetime broadening approximation to the Green's function.

In this formalism, the effect of the disorder-configuration averaged Green's function is often captured by the use of the T matrix, defined by the integral equation $T = W + WG_0T$, where $W = \sum_i V_0\delta(r - r_i)$ and G_0 are the Green's function of the pure lattice. From this, one obtains

$$\bar{G} = G_0 + G_0 T G_0 = G_0 + G_0 \Sigma \bar{G}. \tag{3.39}$$

Upon disorder averaging, we obtain

$$\Sigma = \langle W \rangle_c + \langle W G_0 W \rangle_c + \langle W G_0 W G_0 W \rangle_c + \cdots. \tag{3.40}$$

To linear order in the impurity concentration n_i this translates to

$$\Sigma(z, \mathbf{k}) = n_i V_{\mathbf{k},\mathbf{k}} + \frac{n_i}{V} \sum_{\mathbf{k}} V_{\mathbf{k},\mathbf{k}'} G_0(\mathbf{k}', z) V_{\mathbf{k}',\mathbf{k}} + \cdots, \tag{3.41}$$

with $V_{\mathbf{k},\mathbf{k}'} = V(\mathbf{k} - \mathbf{k}')$ being the Fourier transform of the single impurity potential, which in the case of delta scatterers is simply V_0. Note that $\bar{G}$ and G_0 are diagonal in momentum but, due to the presence of spin-orbit coupling, nondiagonal in spin index in the Pauli spin basis.

One effect of disorder on the spin and anomalous Hall conductivity is taken into account by inserting the disorder averaged Green's function $\bar{G}^{R/A}$ directly into Eqs. (3.36) and (3.38) for σ_{xy}^{Ia} and σ_{xy}^{II}, respectively. This step captures the effect of disorder on the intrinsic contribution to the SHE and AHE, which is generally weak in metallic systems.

The so-called ladder diagram vertex corrections contribute to the AHE and SHE at the same order in $1/k_F l$ as the intrinsic contribution. To capture their effect, we define a ladder-diagram corrected velocity vertex $\tilde{v}_\alpha(\epsilon_F) \equiv v_\alpha + \delta\tilde{v}_\alpha(\epsilon_F)$, where

$$\delta\tilde{v}_\alpha(\epsilon_F) = \frac{n_i V_0^2}{V} \sum_{\mathbf{k}} \bar{G}^R(\epsilon_F)[v_\alpha + \delta\tilde{v}_\alpha(\epsilon_F)]\bar{G}^A(\epsilon_F). \tag{3.42}$$

Note again that $\tilde{v}_\alpha(\epsilon_F)$ and $v_\alpha = \partial\hat{H}_0/\partial\hbar k_\alpha$ are matrices in the spin-orbit-coupled band basis. The skew-scattering contributions are obtained by evaluating third order processes in the disorder scattering, without doing an infinite partial sum as in the case of the ladder diagrams.

As may seem obvious from the above machinery, calculating the intrinsic contribution is not very difficult. However, calculating the full effects of the disorder in a systematic way (beyond calculating a few diagrams) is challenging for any disorder model beyond the simple delta-scattering model.

An important recent development has taken place within the theory of the AHE, which we expect will have a direct analogy to the spin Hall conductivity. Assuming uncorrelated Gaussian noise disorder, i.e., ignoring any skew-scattering contribution, it has been shown that all the scattering-independent contributions (side-jump and intrinsic) can be formulated in terms of the band structure of the crystal alone (Kovalev, Sinova, and Tserkovnyak, 2010; Weischenberg *et al.*, 2011). Note that spin-orbit coupling is not included in the scattering potential W in the microscopic theories we discuss in this section and, therefore, the side-jump contribution is given by the intrinsic side jump only.

For the short-range scattering disorder model, the starting point to calculate the scattering-independent intrinsic-side-jump contribution is the retarded Green's function in equilibrium and the Hamiltonian H of a general multiband noninteracting system. The first step in the calculation is to expand the self-energy of the system Σ_{eq} in powers of the potential V_0, which describes scattering off impurities. One then inserts the expression for the self-energy into the equations for the current densities (spin or charge) derived following the Kubo-Středa formalism mentioned earlier. The next step is to rotate into the chiral eigenstate representation (eigenstates with spin-orbit coupling) and keeping only the leading order terms in the limit of vanishing disorder parameter V_0. Having done this, the scattering-independent part of the AHE conductivity may be written as $\sigma_{xy}^{H-(0)} = \sigma_{xy}^{H-\text{int}} + \sigma_{xy}^{H-\text{sj}}$, where

$$\sigma_{ij}^{H-\text{int}} = \frac{2e^2}{\hbar} \int \frac{d^3k}{(2\pi)^3} \text{Im} \sum_{n \neq m} (f_n - f_m) \frac{v_{nm,i}(\mathbf{k}) v_{mn,j}(\mathbf{k})}{(\omega_n - \omega_m)^2} \tag{3.43}$$

is the intrinsic contribution. In this expression, the band indices n and m run from 1 to N, $v_{nm,i}$ are the matrix elements of the velocity operator $\hat{v}_i = \partial_{\hbar k_i}\hat{H}$, and $\omega_n(\mathbf{k}) = \varepsilon_n(\mathbf{k})/\hbar$. The scattering-independent intrinsic-side-jump contribution to the AHE conductivity for inversion-symmetric systems reads

$$\sigma_{ij}^{H-\text{sj}} = \frac{e^2}{\hbar} \sum_{n=1}^{N} \int \frac{d^3k}{(2\pi)^3} \text{ReTr} \Big\{ \delta(\varepsilon_F - \varepsilon_n) \frac{\gamma_c}{[\gamma_c]_{nn}} \times \Big[S_n A_{k_i} (1 - S_n) \frac{\partial \varepsilon_n}{\partial k_j} - S_\eta A_{k_j} (1 - S_n) \frac{\partial \varepsilon_n}{\partial k_i} \Big] \Big\}. \tag{3.44}$$

Here the imaginary part of the self-energy $\text{Im}[\Sigma_{\text{eq}}] = -\hbar V_0 \gamma$ is taken to be in the eigenstate representation, i.e., $\gamma_c = U^\dagger \gamma U$, with

$$\gamma = \frac{1}{2} \sum_{n=1}^{N} \int \frac{d^3k}{(2\pi)^2} U S_n U^\dagger \delta(\omega_F - \omega_n), \tag{3.45}$$

U as the unitary matrix that diagonalizes the Hamiltonian at point $\mathbf{k}$,

$$[U^\dagger H(\mathbf{k}) U]_{nm} = \varepsilon_n(\mathbf{k}) \delta_{nm}. \tag{3.46}$$

Here S_n is a $N \times N$ matrix that is diagonal in the band indices, $[S_n]_{ij} = \delta_{ij}\delta_{in}$, and the so-called Berry connection matrix is given by $A_{\mathbf{k}} = iU^\dagger \partial_{\mathbf{k}} U$. Not included in Eq. (3.44) are the

TABLE II. AHE conductivities for bcc Fe and hcp Co in S/cm for selected high-symmetry orientations of the magnetization. $\sigma_{xy}^{H-\text{int}}$, $\sigma_{xy}^{H-\text{sj}}$ and $\sigma_{xy}^{H-\text{int+sj}}$ stand for intrinsic contribution, intrinsic-side-jump contribution, and their sum, respectively. The experimental values are for the scattering-independent conductivity. From Weischenberg *et al.*, 2011.

Fe	[001]	[111]	[110]	Co	[001]	[100]
$\sigma_{xy}^{H-\text{int}}$	767	842	810	$\sigma_{xy}^{H-\text{int}}$	477	100
$\sigma_{xy}^{H-\text{sj}}$	111	178	141	$\sigma_{xy}^{H-\text{sj}}$	217	−45
$\sigma_{xy}^{H-\text{int+sj}}$	878	1020	951	$\sigma_{xy}^{H-\text{int+sj}}$	694	55
Exp.	1032			Exp.	813	150

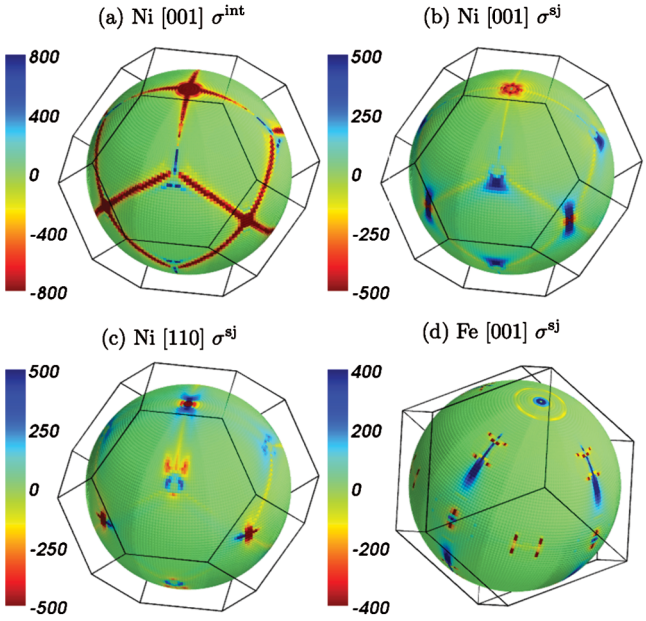

FIG. 14 (color online). Angular distribution of the (a) intrinsic-side-jump contribution for Ni [001], (b) intrinsic-side-jump contribution for Ni [110], (c) intrinsic contribution for Ni [001], and (d) intrinsic-side-jump contribution for Fe [001] on a sphere in the Brillouin zone. The dark regions correspond to large contributions. The color code of each surface point corresponds to the sum of all contributions along the path from the origin to the particular surface point. From Weischenberg *et al.*, 2011.

vertex corrections, which vanish for an inversion-symmetric system in the Gaussian disorder model. For an inversion-asymmetric system, the vertex corrected velocity operator would have to be explicitly calculated. Because the intrinsic-side-jump contribution in the short-range disorder model is solely determined by the electronic structure of the pristine crystal, it is thus directly accessible by *ab initio* methods.

Table II shows a comparison of the improvement in predictive power of the AHE theory when including the intrinsic-side-jump term. Figure 14 shows the nontrivial angular dependence, within the Fermi surface, of the intrinsic-side-jump contribution and the intrinsic contribution. This is reminiscent of the spin-hot spots observed previously in the theory of spin dephasing, and emphasizes the importance of anisotropies induced by the band structure itself.

Finally we note that a study that incorporates the intrinsic contribution as well as the skew-scattering contribution within *ab initio* calculations has shown a good semiquantitative agreement within certain simple alloys (Lowitzer *et al.*, 2011).

IV. EXPERIMENTAL STUDIES OF SPIN HALL EFFECT

Several experimental schemes to detect the SHE were outlined by Dyakonov and Perel (1971b) in their seminal theory work. They proposed to use paramagnetic resonance for detecting the edge spin polarization, to measure the nuclear magnetization resulting from the Overhauser effect, to exploit the gyrotropy, i.e., the difference in the propagation of electromagnetic waves with opposite helicities through the spin-polarized edges, or, in semiconductors, to detect circular polarization of the luminescence excited by an unpolarized light.

Variants of the two latter schemes, namely, the Kerr magneto-optical microscopy and circularly polarized electroluminescence from the sample edges, were indeed employed in the pioneering SHE experiments (Kato *et al.*, 2004a; Wunderlich *et al.*, 2004, 2005). These were, however, performed more than 30 years after the original proposal by Dyakonov and Perel (1971b). Within these three decades, the interest in the phenomenon was scarce. The experimental SHE research only picked up momentum after the theoretical work by Hirsch (1999) who rediscovered the phenomenology of the extrinsic SHE, and after the prediction of the intrinsic SHE (Murakami, Nagaosa, and Zhang, 2003; Sinova *et al.*, 2004).

The renewed theoretical interest occurred in the midst of an extraordinary growth of the nascent field of spintronics (Zutic, Fabian, and Sarma, 2004), which had already found important applications in the hard-disk-drive industry and promised revolutionary concepts for memory and logic devices. In this setting, the theoretical SHE proposals not only ignited an extensive theoretical debate for their inherent fundamental interest but also attracted significant attention due to the potential of spin Hall phenomena as new spin injection and detection tools. The proposals started to materialize shortly thereafter with the observations of the SHE in *n*-doped semiconductors (Kato *et al.*, 2004a) and in the 2DHG (Wunderlich *et al.*, 2004, 2005), and of the ISHE in metallic systems (Saitoh *et al.*, 2006; Valenzuela and Tinkham, 2006, 2007).

In this section, we review the experimental studies of the spin Hall phenomena. In Sec. IV.A, we summarize AHE experiments in nonferromagnetic materials that were performed within the three decades separating the first theoretical proposal and the experimental observations of the SHE. The rest of the section is devoted to modern experiments divided according to the techniques used to generate, detect, and manipulate the SHE and ISHE in experimental samples (Secs. IV.B–IV.D). The overall understanding of the experiments is still incomplete regarding some materials and structures, in particular, when trying to quantify the magnitude of the SHE. Therefore, in those cases, we attempt to provide an overview of the current status of the field while stressing the strengths and weaknesses of the different techniques and methods employed.

Apart from the basic research interest in this relativistic quantum-mechanical phenomenon, Sec. IV.D provides an illustration of the application potential of the SHE in spintronic devices. This prompted detailed studies of the SHE efficiency for the charge-spin conversion in a variety of materials. Measurements of the corresponding spin Hall angles are summarized in Sec. IV.E.

A. Early experiments of anomalous Hall effect in paramagnets

Chazalviel and Solomon (1972) reported a pioneering work on a spin-dependent Hall effect in nonmagnetic semiconductors. They detected the AHE in InSb and *n*-doped Ge at low temperatures (<25 K), where the spin polarization was

created by the application of a magnetic field and the spin-dependent Hall effect was separated from the larger ordinary HE by magnetic resonance of the conduction electrons (Chazalviel and Solomon, 1972; Chazalviel, 1975). The magnitude of the measured anomalous Hall angles was of the order of 10^{-4} for InSb, and of 10^{-5} for Ge, while its sign was observed to change depending on the degree of carrier compensation (InSb) and temperature (Ge). The change in sign was associated with competing contributions from the side-jump and skew-scattering mechanisms. The former was expected to be favored in low mobility samples, which was confirmed in the experiment.

In the early 1980s, Fert and collaborators studied diluted magnetic alloys based on nonmagnetic hosts, such as Au and Cu, and magnetic impurities such as Mn, Fe, or Cr (Fert, Friederich, and Hamzic, 1981). They found that CuMn showed negligible skew-scattering effects, but that the exchange scattering by polarized Mn impurities created a spin-polarized current. They also noted that the addition of nonmagnetic impurities to CuMn gave rise to skew scattering of the polarized current by the unpolarized impurities. By analyzing variations of the Hall coefficient, they were able to extract the Hall angle for the nonmagnetic impurities. They found that they varied from -1.4×10^{-2} for Lu to -2.6×10^{-2} for Ir.

In another type of AHE measurement, a circularly polarized beam at the normal incidence to the surface of a bulk semiconductor was used to excite spin-polarized photoelectrons (Bakun *et al.*, 1984; Miah, 2007). These electrons diffused in the vertical direction from the surface and after aligning their spins along an axis parallel to the surface by an applied magnetic field (via Hanle precession), an electrical voltage was detected in the transverse in-plane direction (Bakun *et al.*, 1984). Alternatively, the vertically spin-polarized electrons can be accelerated in the in-plane direction by an applied electrical bias yielding also a transverse in-plane voltage (Miah, 2007). Since in these experiments the source spin current is accompanied by a diffusive or drift charge current, the geometry corresponds to the AHE (see Sec. III.B).

B. Optical tools in spin Hall experiments

1. Optical detection of the spin Hall effect

The experimental discovery of the SHE was prompted by the intrinsic SHE proposals (Murakami, Nagaosa, and Zhang, 2003; Sinova *et al.*, 2004) which focused on semiconductors and suggested to utilize the optical activity of these materials for detecting the SHE. Similar to the original work by Dyakonov and Perel (1971b), Murakami, Nagaosa, and Zhang (2003), and Sinova *et al.* (2004) proposed a circularly polarized electroluminescence or a spatially resolved magneto-optical Faraday and Kerr effects. These methods were indeed used in the first measurements of the phenomenon. Kato *et al.* (2004a) employed a magneto-optical Kerr microscope to scan the spin polarization across the channel while Wunderlich *et al.* (2004, 2005) used coplanar *p-n* diodes to detect circularly polarized electroluminescence at opposite edges of the spin Hall channel. Wunderlich *et al.* (2004, 2005) ascribed the observed signal to the intrinsic SHE while Kato *et al.* (2004a) to the extrinsic SHE.

Kato *et al.* (2004a) performed the experiments in *n*-GaAs and *n*-$In_{0.07}Ga_{0.93}As$ films grown by molecular-beam epitaxy on (001) semi-insulating GaAs substrates. The films were doped with Si with $n = 3 \times 10^{16}$ cm^{-3} in order to obtain long spin relaxation lifetimes of $\tau_s \sim 10$ ns, which result in spin-diffusion lengths $\lambda_{sd} = \sqrt{D\tau_s} \sim 10$ μm. The unstrained GaAs sample consisted of 2 μm of *n*-GaAs grown on 2 μm of undoped $Al_{0.4}Ga_{0.6}As$, whereas the strained InGaAs sample had 0.5 μm of *n*-$In_{0.07}Ga_{0.93}As$ and 0.1 μm of undoped GaAs. Static Kerr rotation measurements were performed at 30 K with a pulsed Ti:sapphire laser tuned to the absorption edge of the semiconductor with normal incidence to the sample. In this technique, the laser beam is linearly polarized and the polarization axis of the reflected beam is determined. The rotation angle is proportional to the net magnetization along the beam direction.

Figure 15(a) shows a schematic of the experimental geometry. The epilayers were patterned into 300×77 μm^2 (GaAs) and *n*-InGaAs 300×33 μm^2 (InGaAs) channels. An electric field was applied along the channel while a magnetic field B could be applied perpendicular to it in the film plane. Figure 15(b) shows a two-dimensional scan of the GaAs sample, which demonstrates the existence of spin accumulation close to the edges. The amplitude of the measured edge spin polarizations reaches ~0.1%. The polarization has opposite sign at the two edges and decreases rapidly with the distance from the edge as expected for the SHE. This is clearly seen in the one-dimensional profile in Fig. 15(c). Further experiments demonstrated the effect of spin (Hanle)

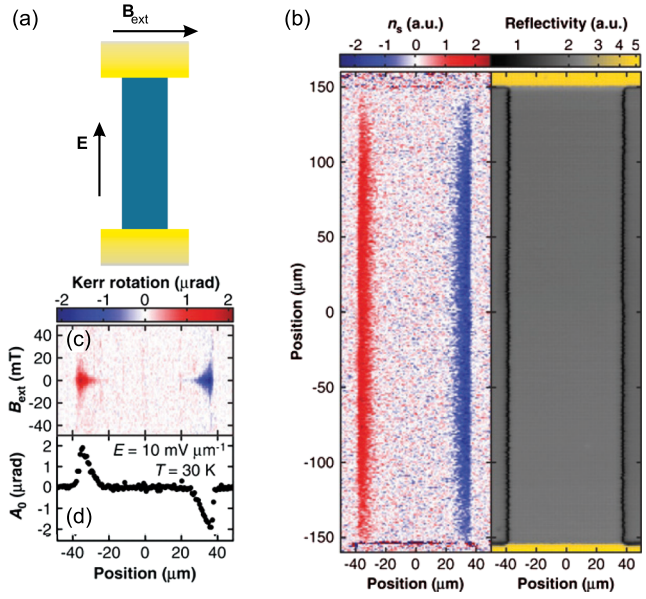

FIG. 15 (color online). Observation of the SHE by the magneto-optical Kerr microscope. (a) Schematics of the GaAs sample. (b) Two-dimensional images of the spin density n_s (left) and reflectivity R (right) for an unstrained GaAs sample measured at temperature 30 K and applied driving electric field $E = 10$ mV μm^{-1}. (c) Kerr rotation as a function of x and external magnetic field B_{ext} for $E = 10$ mV μm^{-1}. (d) Spatial dependence of the peak Kerr rotation A_0 across the GaAs channel. From Kato *et al.*, 2004a.

precession, and associated suppression of the observed signal to the applied magnetic field, as predicted by Dyakonov and Perel (1971a) and Hirsch (1999).

Zhang (2000) showed, by solving the spin-dependent drift-diffusion equations for a finite width channel, that the spin-diffusion length λ_{sd} defines the length scale of the edge spin accumulation. By fitting to the spin-drift-diffusion equation, Kato *et al.* (2004a) extracted the transverse spin current and the spin Hall resistivity ρ^H. This analysis, which assumes well-resolved spin-up and spin-down transport channels (Hirsch, 1999; Zhang, 2000), is valid in the weak spin-orbit limit, which is verified by noting that $\Delta_{so}\tau/\hbar \sim 10^{-3} \ll 1$, where Δ_{so} is the spin-orbit coupling energy and τ is the momentum scattering time. The measured value of $\rho^H \sim 2\ \Omega$m is consistent with that obtained from modeling based on scattering by screened and short-range impurities (Engel, Rasbha, and Halperin, 2006; Tse and Das Sarma, 2006). Noting that the charge resistivity $\rho \sim 4 \times 10^{-6}\ \Omega$m, this corresponds to a spin Hall angle of $\sim 10^{-4}$. In the weak spin-orbit coupling regime, the spin-orbit splitting of the quasiparticle bands is smeared out by disorder which favors the extrinsic SHE interpretation of the measured signal. The absence of the intrinsic SHE was confirmed by measurements in the strained InGaAs sample which showed no dependence of the SHE signal on the strain induced anisotropies of the spin-orbit-coupled band structure.

Experiments in 2DHG devices (Fig. 16) were carried out in the strong spin-orbit coupling limit, $\Delta_{so}\tau/\hbar \sim 4$, which favors the intrinsic mechanism (Wunderlich *et al.*, 2004, 2005; Nomura *et al.*, 2005). The device comprised coplanar *p-n* junction light emitting diodes (LEDs) that were patterned in (Al, Ga)As/GaAs heterostructures grown by molecular-beam epitaxy and using modulation donor (Si) and acceptor (Be) doping in (Al,Ga)As barrier materials. The heterostructure consisted of an *n*-doped AlGaAs/GaAs heterojunction, followed by the growth of 90 nm of intrinsic GaAs and a *p*-doped AlGaAs/GaAs heterojunction. The coplanar *p-n* junctions were created by removing the *p*-doped layer of the wafer and thus creating a hole channel, with a carrier density 2×10^{12} cm^{-2}. The 2DEG at the bottom heterojunction was almost depleted. The removal of *p*-doped surface layer populated the 2DEG, forming the *n*-side of the coplanar *p-n* junction.

A current I_p was applied to drive the electroluminescence at the edge of the channel due to recombination near *p-n* junctions. The detection of spin polarization in the 2DHG was done by measuring the circular polarization of the emitted light, shown in Figs. 16(d) and 16(e). The magnitude of the signal reached $\sim 1\%$ at 4 K. Consistent with the SHE phenomenology, the experiments demonstrated that the spin accumulation was opposite at opposite sides of the channel and that it reversed sign following current reversal.

Calculations of the SHE conductivity showed that the SHE originating from the spin-orbit-coupled quasiparticle bands of the 2DHG is only weakly affected by disorder for the parameters of the studied system (Wunderlich *et al.*, 2005). A quantitative microscopic description of the measured edge spin-accumulation signal was developed and further experimentally tested by Nomura *et al.* (2005). The theory analysis pointed out that the length scale of the edge spin accumulation

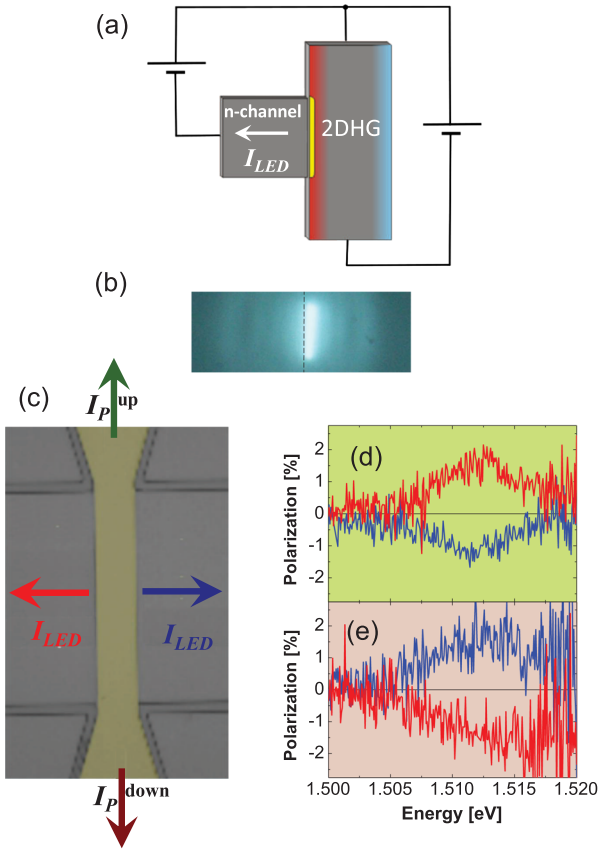

FIG. 16 (color online). Observation of the SHE by the circularly polarized electroluminescence of coplanar *p-n* diodes. (a) Schematic configuration of the lateral *p-n* junction to detect spin accumulation. (b) Light emission from the *p-n* junction recorded by a charged-couple device camera. (c) Electron microscope image of the microdevice with symmetrically placed *p-n* diodes at both edges of the 2DHG channel. (d),(e) Emitted light polarization of recombined light in the *p-n* junction for the current flow indicated in (c) at 4 K. From Nomura *et al.*, 2005.

is defined in the strong spin-orbit coupling regime by the spin-orbit precession length $L_{so} = v_F\tau_{so}$, where $\tau_{so} = \hbar\pi/\Delta_{so}$ is the precession time of the spin in the internal spin-orbit field and v_F is the Fermi velocity. With increasing strength of the spin-orbit coupling, the edge spin-accumulation region narrows down and, simultaneously, the amplitude of the spin polarization increases. For the experimental parameters of the studied 2DHG, $L_{so} \sim 10$ nm and the calculated amplitude of the edge spin polarization was 8%, in good agreement with the 1% polarization of the measured electroluminescence signal which was averaged over a ~ 100 nm sensitivity range of the coplanar light emitting diode. A comparison between measurements in devices with 1.5 and 10 μm wide channels confirmed the expectation that the SHE signal is independent of the channel width.

Subsequent magneto-optical measurements of the SHE in the *n*-GaAs 3D epilayers have experimentally demonstrated that the SHE-induced spin accumulation is due to a transverse spin current which can drive spin polarization tens of microns into a region in which there is minimal electric field (Sih *et al.*, 2006). The work proved experimentally that the SHE can be used as a source of spin current generated in a NM.

A systematic doping dependence of the SHE angle was studied in *n*-GaAs 3D epilayers with electron densities $n = 1.8 \times 10^{16}$–3.3×10^{17} cm^{-3} and the results were found consistent with theory predictions for the extrinsic SHE (Matsuzaka, Ohno, and Ohno, 2009). The measured SHE angles of $\sim 5 \times 10^{-4}$–5×10^{-3} increase with increasing doping with a tendency to saturate at the high doping end of the studied set of samples at a value corresponding to ~1% edge spin polarization. It was concluded from this systematic analysis that the spin accumulation is reduced by an enhanced spin relaxation due to the Dyakonov-Perel mechanism, while the spin current induced by the SHE is enhanced with increasing *n* (Matsuzaka, Ohno, and Ohno, 2009). The SHE was observed also in other semiconductor systems including *n*-ZnSe 3D epilayers (Stern *et al.*, 2006) and InGaN/GaN superlattices (Chang *et al.*, 2007).

2. Optical generation of the inverse spin Hall effect

A traditional way of generating spin-polarized photocarriers in semiconductors is by absorption of circularly polarized light (Meier and Zakharchenya, 1984). Because of the optical selection rules, the out-of-plane spin polarization of photocarriers is determined in this technique by the sense and degree of the circular polarization of vertically incident light. This technique was used to observe the AHE in semiconductors (Bakun *et al.*, 1984; Miah, 2007), which was discussed in Sec. IV.A, and eventually led also to the detection of the ISHE generated by the pure spin current.

Ando *et al.* (2010) reported an experiment in a NM-semiconductor hybrid structure in which they demonstrated the conversion of circularly polarized light absorbed in a semiconductor to an electrical signal in the attached NM ISHE sensor (Fig. 17). The photoinduced ISHE was observed in a Pt/GaAs hybrid structure. In the GaAs layer, circularly polarized light generates spin-polarized carriers, inducing a pure spin current into the Pt layer through the interface. This pure spin current is converted into an electrical voltage due to the ISHE in Pt. Systematic changes of the ISHE signal were observed upon changing the direction and ellipticity of the circularly polarized light, consistent with the expected phenomenology of the photoinduced ISHE. The observed phenomenon allows the direct conversion of circular-polarization information into the electrical voltage and can be used as a spin photodetector.

Using a similar detector configuration, Kampfrath *et al.* (2013) demonstrated the control of the transmission of terahertz spin current pulses. The samples consisted of Fe/Au and Fe/Ru heterostructures. The absorption of a femtosecond laser pulse in the Fe layer generates a nonequilibrium electron distribution and associated spin current, dominated by the majority-spin *sp*-like electrons, that flow into the Au(Ru) nonmagnetic layer. The transport dynamics is different in the Fe/Au and Fe/Ru heterostructures because of the much larger electron mobility of Au; the flow of the nonequilibrium electrons occur much more slowly in Ru than in Au, and are accompanied by significantly more spin accumulation. The nonmagnetic layer can thus be used to either trap or transmit electrons, and thus engineer ultrafast spin pulses, which change in temporal shape and delay.

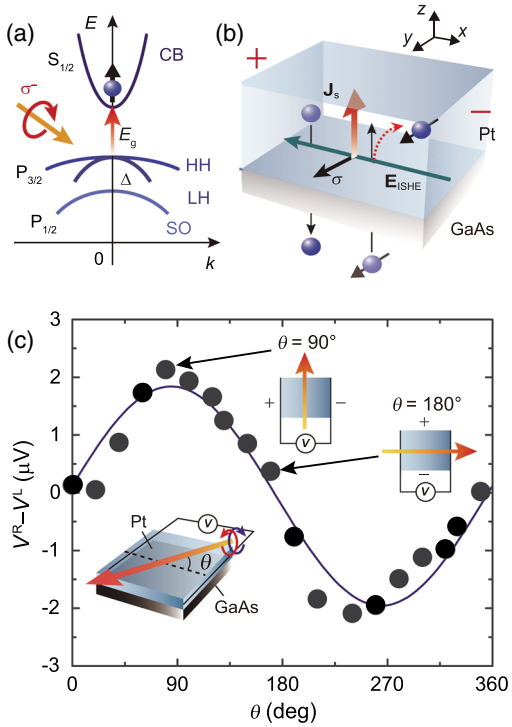

FIG. 17 (color online). (a) Schematic illustration of the band structure of GaAs and spin-polarized electrons generated by the absorption of circularly polarized light. (b) Schematic illustration of the ISHE induced by photoexcited pure spin currents in the Pt/GaAs system. (c) The illumination angle θ dependence of $V^R - V^L$ measured for the Pt/GaAs hybrid structure. θ is the in-plane angle between the incident direction of the illumination and the direction across the electrodes attached to the edges of the Pt layer as shown in the inset. $V^R - V^L$ is the difference in the electromotive force for illumination with right and left circularly polarized light. The filled circles are the experimental data. The solid curve shows a fitting result using a function proportional to $\sin\theta$. From Ref Ando *et al.*, 2010.

The detection of the spin-current pulses used by Kampfrath *et al.* (2013) relied on the ISHE.

While in the static experiments by Ando *et al.* (2010) the resulting charge current is measured as a voltage, Kampfrath *et al.* (2013) detected the electromagnetic pulse emitted by the charge current burst by electro-optical sampling using a GaP crystal. The feasibility of the experiment demonstrated the operation of the ISHE as a spin-current detector up to frequencies as high as 20 THz.

Wunderlich *et al.* (2009, 2010), using the same type of lateral *p*-*n* diodes as in Nomura *et al.* (2005) and Wunderlich *et al.* (2005), exploited optical spin injection by a circularly polarized laser beam to observe the ISHE and to fabricate experimental optospintronic and spin-transistor devices. In the SHE measurements in Nomura *et al.* (2005) and Wunderlich *et al.* (2005), the *p*-*n* junctions were fabricated along the edges of the 2DHG channel and under forward bias could sense the spin state of recombining electrons and holes through polarized electroluminescence. In Wunderlich *et al.* (2009, 2010), on the other hand, the spin Hall channel was fabricated in the etched part of the epilayer with the 2DEG, the channel was oriented perpendicular to the *p*-*n* junction, and

the diode was under zero or reverse bias, operating as a photocell as shown in Fig. 18. The optical activity of the lateral diode confined to a submicron depletion region, combined with a focused (∼1 μm) laser beam, allowed for a well localized injection of spin-polarized photoelectrons into the planar 2DEG channel.

The Hall signals were detected electrically on multiple Hall crosses patterned along the channel. Two regimes of operation of the device are distinguished: One corresponds to an AHE regime, in which the reverse-bias charge current is drained behind the Hall crosses at the opposite end of the channel from the *p*-*n* junction injection point [Fig. 18(a)]. The other regime corresponds to the ISHE measurement since in this case the charge current is drained before the Hall crosses, allowing only the pure spin current to diffuse further in the channel [Fig. 18(b)]. In both cases, the measured transverse electrical signals were consistent with the phenomenology of the spin-dependent Hall phenomena (Wunderlich *et al.*, 2009, 2010). The sign of the voltage was opposite for opposite helicities of the incident light, i.e., opposite spin polarizations of injected photoelectrons. Moreover, the amplitude of the electrical signals was found to depend linearly on the degree of circular

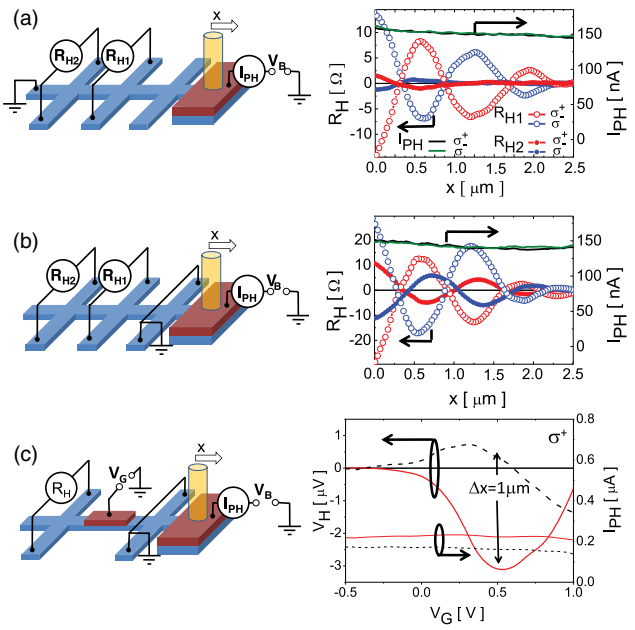

FIG. 18 (color online). ISHE based transistor. (a) Schematics of the spin-injection Hall effect measurement setup with optically injected spin-polarized electrical current propagating through the Hall bar and corresponding experimental Hall effect signals at crosses H1 and H2. The Hall resistances $R_H = V_H/I_{PH}$ for the two opposite helicities of the incident light are plotted as a function of the focused light spot position, i.e., of the position of the injection point. The optical current I_{PH} is independent of the helicity of the incident light and varies only weakly with the light spot position. (b) Same as (a) for the ISHE measurement geometry in which electrical current is closed before the first detecting Hall cross H1. (c) Schematics of the setup of the spin Hall transistor and experimental Hall signals as a function of the gate voltage at a Hall cross placed behind the gate electrode for two light spot positions with a relative shift of 1 μm. From Wunderlich *et al.*, 2010.

polarization of the light, rendering the device an electrical polarimeter (Wunderlich *et al.*, 2009). The electrical signals were observable over a wide temperature range with spin Hall angles of 10^{-3}–10^{-2}. The measured 2DEG was in the weak spin-orbit coupling regime, $\Delta_{so}\tau/\hbar \sim 10^{-1}$, and the measured data were consistent with the extrinsic mechanism (Wunderlich *et al.*, 2009).

3. All-optical generation and detection

The SHE and ISHE were also observed using two-color optical coherence control techniques in intrinsic GaAs at 80 K with polarized 70 fs, 715 and 1430 nm pulses (Zhao *et al.*, 2006). When the pulses were orthogonally polarized, a pure spin source current was generated that yielded a transverse Hall pure charge current via the ISHE. When the pulses were parallel polarized, a pure charge source current was generated that yielded a pure spin current via the SHE. By varying the relative phase or polarization of the incident pulses, the type, magnitude, and direction of both the source and transverse currents were tuned without applying electric or magnetic fields. In contrast to the previous steady-state experiments, where drift currents are generated by electric fields, the injected currents are ballistic with electrons traveling initially at ∼1000 km/s.

The generation of spin and charge currents results from the quantum interference between absorption pathways for one- and two-photon absorption connecting the same initial and final states as illustrated in Fig. 19(a). For a spin current, a coherent pulse centered at frequency ω with phase φ_ω is normally incident along $\hat{z}$ and linearly polarized along the $\hat{x}$ direction which can be arbitrary with respect to crystal axes since the effects are not strongly sensitive to crystal orientation. A copropagating 2ω pulse with phase $\varphi_{2\omega}$ is linearly polarized along the orthogonal $\hat{y}$ direction. Excited spin-up

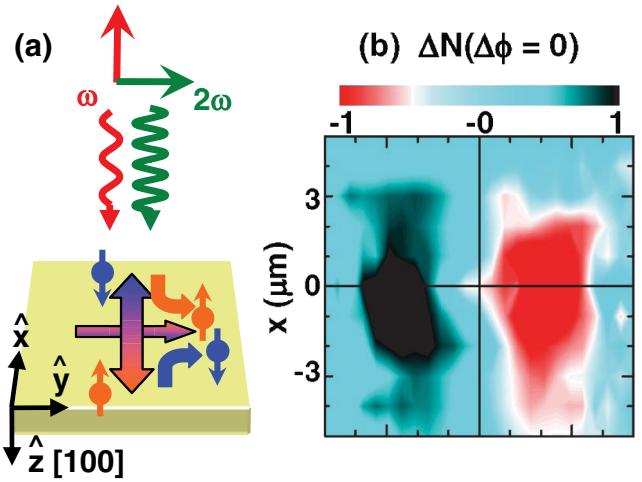

FIG. 19 (color online). Observation of the ISHE using the two-color optical pump-and-probe technique. (a) Illustration of orthogonally polarized ω and 2ω pulses producing a pure spin current (double headed straight arrow) along the ω beam polarization direction ($\hat{x}$). The charge current due to the ISHE (curved arrows) along $\hat{y}$ leads to electron accumulation near one edge of the illuminated region. (b) Measured charge accumulation due to the ISHE. From Zhao *et al.*, 2006.

electrons are polarized along $\hat{z}$ and move preferentially in one direction along $\hat{x}$, while spin-down electrons move in the opposite direction. Together they generate a spin current proportional to $\cos(\Delta\varphi)$ where $\Delta\varphi = 2\varphi_\omega - \varphi_{2\omega}$. The spin current is dominated by electrons as holes lose their spin in <100 fs. Because of the ISHE, a charge current is generated [Fig. 19(a)] that has the same cosine dependence as the spin-current source. Consistent with the ISHE phenomenology, the excess charge on one side and the deficit on the other side of the sample, shown in Fig. 19(b), was observed along the direction perpendicular to the driving spin current.

The ballistic nature of transport in these experiments was fully exploited in fs time-resolved measurements (Werake, Ruzicka, and Zhao, 2011). They allowed one to infer the momentum scattering time $\tau \approx 0.45$ ps and with a much shorter time delay of the probe pulses to observe in real time the transverse charge current. The measurements showed that the charge current was generated well before the first scattering event, providing a direct demonstration of the intrinsic ISHE.

4. Electrical manipulation

A distinct feature of the ISHE experiments in the 2DEG is the observed spin precession due to internal Rashba and Dresselhaus spin-orbit fields (Wunderlich *et al.*, 2009, 2010). Since the spin-diffusion length scales approximately as $\sim L_{so}^2/w$ (Wunderlich *et al.*, 2010), it was possible to observe a few spin precessions in channels of a width $w = 1$ μm for $L_{so} \sim 1$ μm of the studied 2DEG. The corresponding oscillations of the spin Hall voltages were consistently observed by measuring at different Hall crosses along the channel or by shifting the laser spot, i.e., the spin-injection point (Fig. 18). The lateral ISHE channels also allow one to place top gate electrodes in between the Hall crosses as shown in Fig. 18(c). (The gates are formed by unetched regions of the wafer.) The strength of the Rashba and Dresselhaus spin-orbit fields and, therefore, also the spin precession can be manipulated electrically in the device shown in Fig. 18(c). To demonstrate an AND logic functionality, two gates were fabricated on top of the channel and the Hall electrical signal was measured at a cross placed behind both gates. Intermediate gate voltages on both gates represented the input value 1 and gave the largest electrical ISHE signal, representing the output value 1. When a large reverse gate voltage was applied to any of the two gates, representing input 0, the electrical ISHE signal disappeared, i.e., the output was 0.

A different approach to achieve the control of spin currents is by directly modifying the spin-orbit coupling strength on a given material, which in turn determines the spin Hall angle. The electronic band structure and impurity states are weakly dependent on an external electric field and therefore cannot be used to change the spin-orbit strength. However, Okamoto *et al.* (2014) noted that the electric field can induce a carrier redistribution within a band or multiple bands. Therefore, if the electrons generating the SHE can be controlled by populating different areas (valleys) of the electronic structure, the spin-orbit interaction (and the spin Hall angle) can be tuned directly within a single sample. Okamoto *et al.* (2014) reported such a tuning in bulk GaAs at room temperature by means of an electrical intervalley transition induced in the conduction band. The spin Hall angle was determined by measuring an electromotive force driven by photoexcited spin-polarized electrons drifting through n-GaAs Hall bars. By controlling electron populations in the Γ and L valleys with an applied electric field (part of the p character in the L valley provides a larger effective spin-orbit interaction), the spin Hall angle was changed by a factor of 40, from 0.0005 to 0.02 for moderate electric fields beyond 100 kV m^{-1}. Thus the highest spin Hall angle achieved is comparable to that of Pt.

C. Transport experiments

Hirsch (1999) and Zhang (2000) discussed specific concepts for the experimental detection of the SHE and ISHE using dc transport techniques. Hirsch (1999) proposed a device that consists of a metallic slab in which spin accumulation is generated by an electrical current via the SHE, as described in Sec. II (see Fig. 2). A transverse strip connects the edges of the slab, allowing the spin current to flow through it. Because of the ISHE, a voltage is generated that can be measured with a voltmeter. In an alternative approach, Zhang (2000) proposed to detect the spin accumulation electrically using a FM probe. The concept borrows from techniques for spin injection and detection in NM implemented in nonlocal spin devices (Silsbee, 1980; Johnson and Silsbee, 1985).

Shortly after the optical SHE detection in semiconductors (Kato *et al.*, 2004a; Wunderlich *et al.*, 2004, 2005), Valenzuela and Tinkham (2006) reported an observation of the voltage generated by the ISHE. Instead of generating the spin current by the SHE, which would render a second-order voltage in the spin Hall angle, they used electrical spin injection from a FM in combination with a Hall cross patterned in the ISHE paramagnet. Independently, Saitoh *et al.* (2006) observed the voltage generated by the ISHE in a setup where the spin injection from the FM to the NM was achieved using the SP techniques. Kimura *et al.* (2007) combined the concept of the spin Hall cross and the proposal by Zhang (2000) to detect both the SHE and ISHE in the same device. It took a few more years to demonstrate the idea of Hirsch of simultaneously exploiting both the SHE and the ISHE in an electrical device. It was first attempted by Mihajlovic *et al.* (2009) using a gold H-bar device (Hankiewicz *et al.*, 2004), but they did not succeed in observing a spin Hall related signal. Eventually, this was achieved by Brüne *et al.* (2010), who performed the experiment in a ballistic semiconductor H-bar device. The transport SHE and ISHE experiments are described in detail in Secs. IV.C.1–IV.C.5.

More recently, the SHE was also detected via the manipulation of magnetization in FMs (Liu *et al.*, 2011; Miron, Garello *et al.*, 2011). Spin currents generated by the SHE were shown to be sufficiently large to induce magnetization dynamics, drive domain walls, or switch magnetization in the FM, demonstrating the potential of the SHE for applications (Miron, Garello *et al.*, 2011; Miron *et al.*, 2011; Liu, Pai, Li *et al.*, 2012; Emori *et al.*, 2013; Ryu *et al.*, 2013). These SHE experiments together with the ISHE measurements via SP are discussed in Sec. IV.D.

1. Concepts of nonlocal spin transport: Electrical injection and detection

Johnson and Silsbee (1985) reported the injection and detection of nonequilibrium spins using a device that consisted of a NM (N), with two attached FM electrodes (F1, F2), illustrated in Fig. 20. In this device, spin-polarized electrons are injected from F1 into N by applying a current I from F1 that results in spin accumulation in N. The population of, say, spin-up electrons in N increases by shifting the electrochemical potential by $\delta\mu_N$, while the population of spin-down electrons decreases by a similar shift of $-\delta\mu_N$. Overall, this corresponds to a spin-accumulation splitting of $2\delta\mu_N$. The spin accumulation diffuses away from the injection point and reaches the F2 detector, which measures its local magnitude.

As first suggested by Silsbee (1980), the spin accumulation in N can be probed by the voltage V_{NL}, which is induced at F2. Silsbee noted that the polarization density in N, or equivalently the nonequilibrium magnetization, acts as the source of the spin electromotive force that produces V_{NL}. The magnitude of V_{NL} is associated with $\delta\mu_N$, while its sign is determined by the relative magnetization orientation of F1 and F2.

Because the current is drained to the left of N, there is no charge current toward the right, where the detector F2 lies [Fig. 20(a)]. For this reason, the spin detection is said to be implemented nonlocally, where no charge current circulates by the detection point, and thus V_{NL} is sensitive to the spin degree of freedom only. Accordingly, nonlocal measurements eliminate the presence of spurious effects associated to charge transport, such as anisotropic magnetoresistance (AMR) or the ordinary HE that could mask subtle signals related to spin injection. Typically, nonlocal devices exhibit a small output background allowing sensitive spin-detection experiments. This approach has been widely used in recent years to characterize the spin transport in metals, semimetals, semiconductors, superconductors, carbon nanotubes, and graphene. It has also been used to study the spin-transfer properties of FM-NM material interfaces.

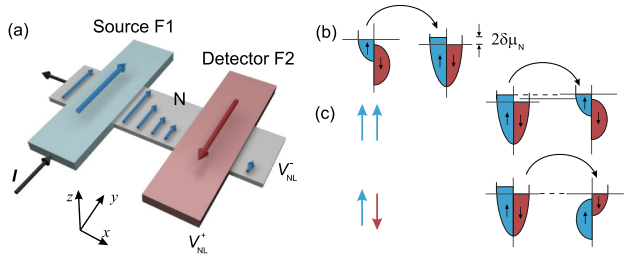

FIG. 20 (color online). Nonlocal spin detection and spin accumulation. (a) Schematic illustrations of the device layout. An injected current I on the source (F1) generates spin accumulation in the NM (N) which is quantified by the detector (F2) voltage V_{NL}. (b) Schematic representation of the spin splitting in the electrochemical potential induced by spin injection. The splitting decays over characteristic lengths λ_{sd} over the N side. (c) Detector behavior for an idealized Stoner FM with a full spin subband for the parallel magnetization orientation (top) and for the antiparallel magnetization orientation (bottom).

2. Nonlocal detection of inverse spin Hall effect with lateral spin current

Valenzuela and Tinkham (2006, 2007) adapted the nonlocal detection techniques to study the ISHE. Their device is schematically shown in Fig. 21(a). By using a FM electrode, a spin-polarized current is injected in a NM strip (N). It propagates to both sides away from the injection point and decays within the spin-diffusion length λ_{sd}. A laterally induced voltage V_{SH}, which results from the conversion of the injected spin current into charge imbalance owing to the ISHE, is then measured using a Hall-cross structure. The magnitude of V_{SH} is proportional to the anomalous Hall operator $\sigma_{\mathrm{SH}}\boldsymbol{\sigma}\times\mathbf{E}^s$, where σ_{SH} denotes the spin Hall conductivity, $\boldsymbol{\sigma}$ is the direction of the spin polarization injected from the FM electrode, and $\mathbf{E}^s$ is an effective spin-dependent "electric" field, which follows from the spin-dependent electrochemical potential μ^s along the NM strip, i.e., $\mathbf{E}^s(\mathbf{r}) = -\nabla\mu^s(\mathbf{r})$.

In the device of Fig. 21(b), the injector FM electrode (F1) is made of CoFe, while the NM strip material is Al of thickness t_{Al}. The entire structure is fabricated without breaking vacuum using electron-beam evaporation and shadow evaporation techniques. An Al_2O_3 tunnel barrier is used for spin-current injection. The purpose of the barrier is twofold. First, it enhances the polarization of the injected electrons and, second, it assures a uniform current injection. The latter is essential because it suppresses the flow of charge current toward the Hall cross, preserving the nonlocal character of the measurements and eliminating the previously mentioned spurious effects.

The FM electrode is magnetized in-plane at zero magnetic field due to shape anisotropy and thus an out-of-plane magnetic field $B_\perp$ is used to generate a perpendicularly polarized spin current at the Hall cross [Fig. 21(b)]. Spin imbalance in the Al film occurs with a defined spin direction given by the magnetization orientation of the F1 electrode. Consequently, V_{SH} is expected to vary when $B_\perp$ is applied and the magnetization $\mathbf{M}$ of the electrode is tilted out of the substrate plane. Defining θ as the angle between $\mathbf{M}$ and the electrode axis, it follows from the cross product in the anomalous Hall operator that V_{SH} is proportional to $\sin\theta$, correlating with the component of $\mathbf{M}$ normal to the substrate [Fig. 21(b)].

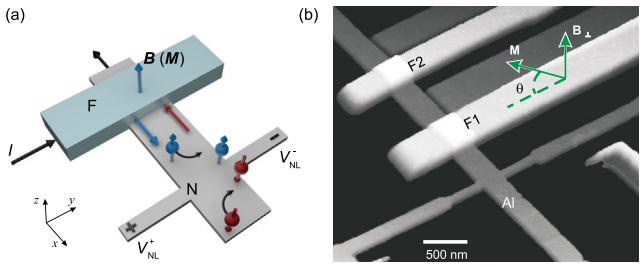

FIG. 21 (color online). (a) Spin-current-induced Hall effect or inverse spin Hall effect. Schematic representation of an actual device where the pure spin current is generated by spin injection through a FM (F) with out-of-plane magnetization. (a) Device fabricated with CoFe electrodes (light gray) and an Al channel (dark gray). Adapted from Valenzuela and Tinkham, 2006.

The device layout in Fig. 21(b) is more sophisticated than the schematics in Fig. 21(a), where only F1 is required. The second FM electrode (F2) together with the injection FM electrode (F1) and the NM strip form a spin injection and detection device [Fig. 22(a)] for calibration purposes. Calibration procedures are necessary to demonstrate consistency with standard nonlocal methods. Explicitly, this device can be utilized to measure the spin accumulation in the NM and then determine its associated spin-diffusion length λ_{sd}, the amplitude of the spin polarization of the injected electrons P, and the magnetization orientation of the FM electrodes θ in the presence of an external magnetic field (perpendicular to the substrate). For this purpose, batches of samples are commonly used where the distance between the two FMs L_F is modified and the spin-precession signal acquired [Fig. 22(b)]. The distance of F1 relative to the Hall cross L_{SH} is also modified in order to test the consistency of the spin-diffusion results. Subsequent measurements [Fig. 22(d)] in the configuration of Fig. 22(c), performed in Al of different t_{Al}, and thus different λ_{sd}, yielded $\sigma_{SH} \sim 20 - 40\ \Omega\,\mathrm{cm}^{-1}$ and $\alpha_{SH} \sim (1\text{–}3) \times 10^{-4}$, which compares well with theoretical estimates based on extrinsic mechanisms (Shchelushkin and Brataas, 2005).

Olejník *et al.* (2012) used the same geometry to detect the ISHE in *n*-GaAs using epitaxial ultrathin Fe/GaAs injection contacts with strong in-plane magnetic anisotropy. Hybrid semiconductor–metal FM structures suffered for a long time from the resistance mismatch problem (Schmidt *et al.*, 2000). Since the spin transport relies on different conductivities for spin-up and spin-down electrons and is governed by the least conductive part of the device, the effects are weak in devices in which the nonmagnetic semiconductor with equal spin-up and spin-down conductivities dominates the resistance of the device (Rasbha, 2000). The introduction of a highly resistive tunnel barrier between the FM metal electrode and the semiconductor channel solved the problem (Rasbha, 2000; Lou *et al.*, 2007).

The device of Olejník *et al.* (2012), shown in Fig. 23(a), comprised the *n*-GaAs channel, a Hall cross, and two ferromagnetic (Fe) electrodes [as described in Fig. 21(a)] with Fe Schottky injection contact. The Fe/*n*-GaAs heterostructure was grown epitaxially in a single molecular-beam epitaxy chamber without breaking ultrahigh vacuum. The heterostructure contained 250 nm of low Si-doped GaAs (5×10^{16} cm^{-3}), 15 nm of GaAs with graded doping, and 15 nm of highly Si-doped GaAs (5×10^{18} cm^{-3}). The purpose of the doping profile was to create a narrow tunnel Schottky barrier between GaAs and Fe favorable for spin injection or detection. It was then possible to simultaneously detect the spin current in *n*-GaAs generated by nonlocal injection from a Fe contact by using the ISHE and the spin accumulation by using the additional Fe contact [Figs. 23(b) and 23(c)]. The spins were manipulated by spin precession with an external magnetic field combined with drift using an external bias (Huang, Monsma, and Appelbaum, 2007). In this case, the magnetic field was applied in-plane (x direction) to precess the spin accumulation into the out-of-plane direction, so that it could be detected by the ISHE. The signal first increases at low fields but then is suppressed due to spin dephasing [Fig. 23(c)].

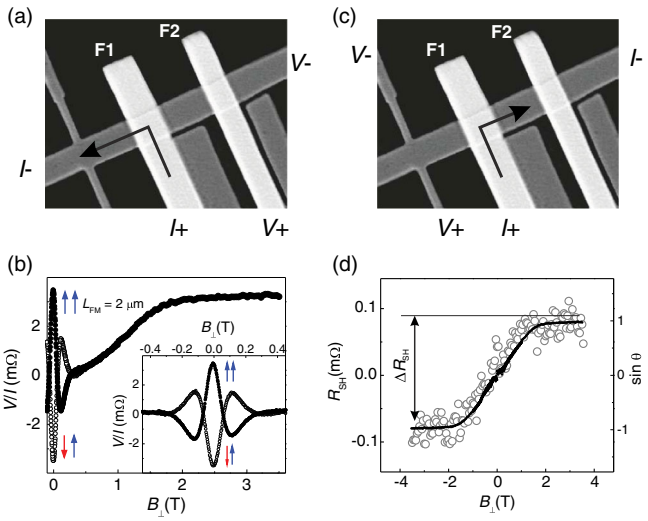

FIG. 22 (color online). Observation of the ISHE (right) in a metal device with an electrical spin injection from a FM, compared with the spin detection by the nonlocal spin valve effect (left). The light gray FM electrodes in the micrographs are made of a CoFe alloy. The dark gray Hall cross is made of Al. (a) and (c) represent the measurement configurations; (b) and (d) show typical spin precession and ISHE signals, respectively. From Valenzuela and Tinkham, 2006.

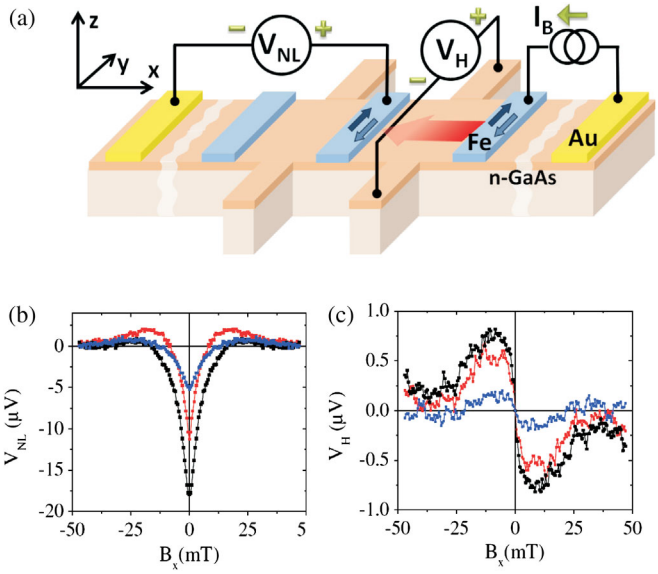

FIG. 23 (color online). (a) Schematic of the device used to detect the ISHE in *n*-GaAs. Current is injected on the Fe electrode on the right, the voltage generated by ISHE and by spin accumulation are detected simultaneously with the Hall cross and the Fe electrode on the left, respectively. The spin transport can be further modified by a drift current applied between the outermost Au electrodes. (b),(c) The experimental symmetrized nonlocal spin injection or detection signal and the antisymmetrized ISHE signal in the in-plane hard-axis field for constant spin-injection bias current (300 μA) and for three different drift currents. From Olejník *et al.*, 2012.

The devices described required the application of a magnetic field for observing the ISHE. Seki *et al.* (2008) used a FM (FePt) with an out-of-plane anisotropy, which enabled them to investigate the ISHE in Au without magnetic fields. The device was fabricated with the geometry in Fig. 21 using Ohmic contacts. The measurements presented a rather large background voltage, which is likely due to the flow of charge current at the position of the Hall cross (Mihajlovic *et al.*, 2009). The use of Ohmic contacts, as opposed to tunnel barriers, results in inhomogeneous in-plane current injection. Because the width of the Au wire and the distance of the Hall cross were comparable, some current reached the Hall cross contributing to the background; therefore the experimental artifacts discussed previously cannot be ruled out completely. By considering that the voltage was independent of the magnetization of the injector electrodes, Seki *et al.* deduced $\alpha_{SH} = 0.113$ for Au at 295 K, which was weakly dependent on temperature. This large α_{SH} was first attributed to resonant scattering in the orbital-dependent Kondo effect of Fe impurities in the Au host metal (Guo, 2009). In the follow-up work, Sugai, Mitani, and Takanashi (2010) found that $\alpha_{SH} \sim 0.07$ was approximately independent of the Fe concentration. Seki *et al.* (2010) further observed a reduction of α_{SH} from 0.1 to 0.03 when the Au thickness was increased from 10 to 20 nm. Additionally, Gu *et al.* (2010) obtained similar results in Pt-doped Au by codeposition of Pt and Au with magnetron sputtering (1.4% Pt). These results in combination with *ab initio* and quantum Monte Carlo calculations for the skew scattering due to a Pt impurity led to the proposal of a much larger α_{SH} in the surface of Au than in the bulk (Gu *et al.*, 2010).

3. Nonlocal detection of spin Hall effects with vertical spin current

The approach described in the previous section enables proper quantification of the spin Hall angle because of the direct measurements of the spin-diffusion length and the fact that no additional interfaces are required. However, it is suitable for materials that have spin-diffusion lengths beyond tens of nanometers. For smaller spin-diffusion lengths, Kimura *et al.* (2007) used a similar approach with the device structure shown in Fig. 24(a). The structure comprises a Hall cross where the material of the transverse arm is the large spin-orbit coupling NM with short λ_{sd}, which acts as a spin-current absorber that induces V_{SH} via the ISHE. The longitudinal arm (N1), on the other hand, is made of a NM with long spin-diffusion length and fulfils the purpose of transporting spin information between the FM electrode (F) and N2.

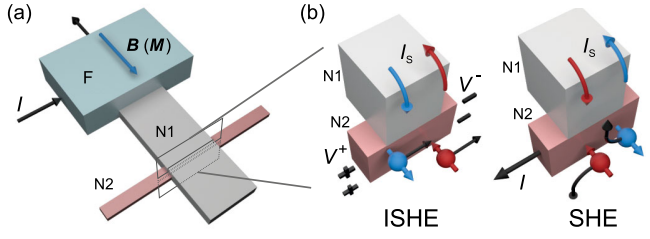

FIG. 24 (color online). (a) Schematic illustration of a nonlocal device to measure the direct and inverse spin Hall effect in materials (N2) with short spin relaxation length λ_{sd}^{N2}. (b) Schematic illustration of the charge accumulation process in N2 (left) due to the ISHE when a spin current is injected from F as in (a). Schematic illustration of the charge to spin-current conversion due to the SHE when a current is applied to N2. This process generates spin accumulation that is detected by measuring the voltage at which F floats. See Kimura *et al.* (2007). Adapted from Valenzuela and Kimura, 2012.

The way the measurements are performed is sketched in Fig. 24(b) (left). A charge current is injected from F into N1 that induces a spin current toward N2 polarized in-plane in the direction parallel to the N1 arm. When the distance between F and the cross is smaller than the spin-diffusion length in N1, the spin current is preferably absorbed into the transverse arm N2 because of the strong spin relaxation in N2. The injected vertical spin current into N2 vanishes in a short distance from the N1-N2 interface because of the short spin-diffusion length of N2 and generates a transverse voltage via the ISHE.

Owing to the broken inversion symmetry at the N1-N2 interface, the crystal field can induce an interface contribution to the spin-orbit coupling (Linder and Yokoyama, 2011) and therefore an additional source of SHE as well as a contribution of the spin to charge conversion from SGE (Rojas-Sánchez *et al.*, 2013b; Zhang *et al.*, 2015). In the following discussion, the SGE is not invoked to explain the results when using the device in Fig. 24. This is rooted in the fact that the relevance of SGE-ISGE in metals was brought to the attention of the community in the recent SOT studies, only after most of the SHE experiments discussed here were carried out. Future experiments might require a more careful analysis to determine the relative weight of the ISHE and SGE in the measurements.

The device shown in Fig. 24 can be also used to measure the SHE (or the ISGE). The bias configuration is modified as shown in Fig. 24(b) (right). Here N2 acts as a spin-current source, which induces a spin accumulation in N1 that is detected with the FM electrode F, as originally proposed by Zhang (2000).

Kimura *et al.* (2007) used permalloy (Py) as the FM source, and Cu and Pt as N1 and N2, respectively (see Fig. 25). The

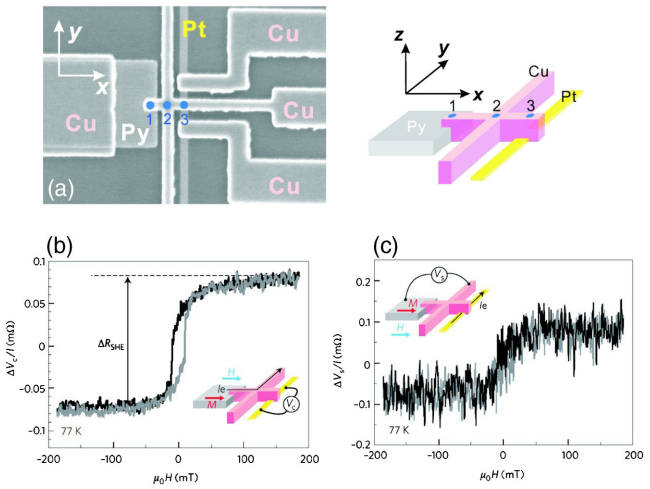

FIG. 25 (color online). (a) Scanning electron microscope (SEM) image of the fabricated spin Hall device to measure the SHE in Pt together with a schematic illustration of the fabricated device. (b) Signal due to the ISHE at 77 K. The black and grey curves show measurements for the two opposite sweeps of the magnetic field. Spin-accumulation signal generated by SHE at 77 K. Insets: measurement setup. NiFe, Cu, and Pt are in different colors. From Kimura *et al.*, 2007.

materials were deposited by electron-beam evaporation. The devices were fabricated with transparent interfaces between Py and Cu and between Pt and Cu. Ar ion beam etching was done prior to depositing Cu in order to clean the surfaces of Py and Pt, a method that has been repeated in the other studies described below. The long spin-diffusion length of Cu (about 500 nm) assured that the spin current reached Pt, which was 4 nm thick. The measurements were interpreted with a one-dimensional model by assuming that the induced spin current at the Cu-Pt interface was completely absorbed by the Pt and was uniform along the vertical direction. The spin relaxation length for Py was assumed (not measured) to be 3 nm. Kimura *et al.* (2007) then obtained that $\sigma_{SH} \sim 2.4 \times 10^2\ \Omega\,\mathrm{cm}^{-1}$ and $\alpha_{SH} = 3.7 \times 10^{-3}$.

Over the last few years some of the initial simplifications that are mentioned have been removed, leading to more reliable quantitative interpretations of the experimental results. Vila, Kimura, and Otani (2007) noted that the absorption efficiency of the spin current may depend on the device geometry and temperature. They modified the design of Fig. 25 to a conventional nonlocal spin injection or detection structure where a Pt electrode was inserted between the FM Py electrodes (see Fig. 26). This change enabled them to determine explicitly the magnitude of the absorbed spin current. By comparing with reference devices without the Pt insertion, they observed that the ratio between the spin signal with and without Pt varied from 0.35 at 5 K to 0.2 at room temperature, irrespective of the Pt thickness. They then performed systematic spin-absorption studies as a function of the Pt thickness, obtaining that λ_{sd} for Pt was 10 and 14 nm at room temperature and at 5 K, respectively.

The Pt thickness dependence of the ISHE signal resulted in somewhat lower λ_{sd} for Pt of 7 and 8 nm at room temperature and at 5 K, respectively. The obtained value of $\sigma_{SH} \sim 3.5 \times 10^2\ \Omega\,\mathrm{cm}^{-1}$ was larger than that in the Kimura *et al.* (2007) experiment; this is because the assumption of the complete spin-current absorption into the Pt wire led to underestimating the spin Hall conductivity.

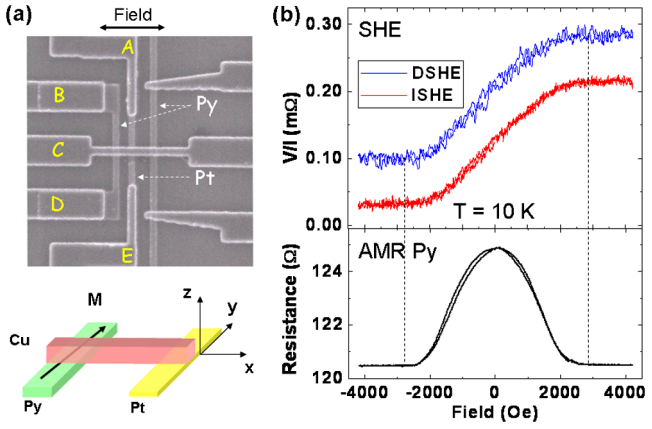

FIG. 26 (color online). (a) SEM image of the typical device for SHE measurements and an illustration of the device. (b) Direct and inverse SHE (SHE and ISHE) recorded at $T = 10$ K using a device with a Pt thickness of 20 nm, altogether with the AMR from the Py wire measured on the same condition. SHE measurement corresponds to V_{BC}/I_{AE}, and ISHE to V_{EA}/I_{BC}; with V the voltage, I the applied current; A, B, C, and E are the contact leads as denoted in the SEM image. From Vila, Kimura, and Otani, 2007.

Additionally, Vila, Kimura, and Otani (2007) found that the spin Hall conductivity was nearly constant as a function of temperature, indicating that the spin Hall resistivity likely evolves in a quadratic form with the Pt resistivity in the analyzed temperature range, which was initially associated to a side-jump origin of the SHE. However, this resistivity dependence can also be associated with the intrinsic mechanism (Tanaka *et al.*, 2008; Kontani *et al.*, 2009).

Niimi *et al.* (2011) further included a correction factor $0 < x < 1$ that accounted for the fact that the transverse charge current induced by the ISHE is partially shunted by the wire N1 above the N1-N2 interface or, conversely, that the charge current that induces the spin current via the SHE does not only flow through N2 but also leaks into N1 [see also Liu *et al.* (2011)]. In order to determine x experimentally, they measured the voltage drop of two identical N2 nanowires with and without shunting N1 bridges. Within a one-dimensional circuit model, the current flowing into the N2 wire I_0 was assumed to divide into two components at the N1-N2 interface: xI_0 for the N2 wire and $(1-x)I_0$ for the N1 bridge. With this, x was estimated to be 0.36 ± 0.08 for Cu (N1), when using a number of transition metals and alloys as N2 (Morota *et al.*, 2011; Niimi *et al.*, 2011), therefore appearing to be rather insensitive to the resistivity of N2. Because of this correction, former reports underestimated σ_{SH} by a factor $x^{-1} \sim 2.8$. Such large correction is to be expected given that the N1 wire (usually Cu or Ag) is highly conductive [conductivity $\sim(3-5) \times 10^7\ \Omega\,\mathrm{m}^{-1}$) and thick ($\sim$100 nm), when comparing with N2 ($\sim 10^5 - 10^7\ \Omega\,\mathrm{m}^{-1}$ and $\sim$10 nm).

In addition, Morota *et al.* (2011) and Niimi *et al.* (2011) pointed out that the spin currents injected in N2 should dilute when its thickness t_{N2} is larger than the spin-diffusion length in N2 leading to smaller spin Hall signals. To correct for this effect, they obtained an aggregate spin current in N2 by integrating over t_{N2}, which was then divided by t_{N2}; they also forced the spin current to be zero at the bottom surface of N2.

Niimi *et al.* (2011) reported $\alpha_{SH} = 0.021 \pm 0.006$ for the skew scattering off Ir in a Cu matrix, which is consistent with experimental work relying on spin-polarized currents generated by dilute Mn impurities, for which $\alpha_{SH} = 0.026$ (Fert, Friederich, and Hamzic, 1981; Fert and Levy, 2011). The spin Hall angle was extracted with CuIr wires that were prepared with different Ir concentrations (0%, 1%, 3%, 6%, 9%, and 12%) using magnetron sputtering. They measured ρ^H of CuIr as a function of the resistivity induced by the Ir impurities, defined as $\rho_{imp} = \rho_{CuIr} - \rho_{Cu}$, finding a simple linear dependence up to Ir concentration of 12%. This was presented as a proof that the dominant mechanism of the extrinsic SHE induced by the Ir impurities is the skew scattering, with $\alpha_{SH} = \rho^H/\rho_{imp}$.

Morota *et al.* (2011) investigated the ISHE and SHE in $4d$ and $5d$ transition metals, Nb, Ta, Mo, Pd, and Pt. Nb, Ta, and Mo wires were deposited by magnetron sputtering while Pd and Pt wires were grown by electron-beam evaporation. In particular, for Pt, they obtained a spin Hall angle $\sigma_{SH} = 0.021 \pm 0.005$ that was roughly 6× larger than that in Kimura *et al.* (2007). Such a difference can be explained with the

above corrections. They also found that the sign of the spin Hall conductivity changes systematically depending on the number of d electrons, a tendency that is in good agreement with theoretical calculations based on the intrinsic SHE (Kontani *et al.*, 2009).

More recently, Niimi *et al.* (2012) studied the ISHE and SHE by introducing a small amount of Bi impurities in Cu. The alloys of $Cu_{1-x}Bi_x$ were deposited by magnetron sputtering from Bi-sintered Cu targets with different Bi concentrations (0%, 0.3%, 0.5%, 1%, 3%, and 6%). The spin Hall resistivity was derived by 1D and 3D calculations as a function of the resistivity induced by the Bi impurities. As for the case with Ir impurities, the experimental results follow the linear variation of the spin Hall resistivity, characteristic of skew scattering by dilute impurities but only at the lowest concentrations (<1%). At larger concentrations, inhomogeneous distribution on Bi results in the departure from the dilute impurity regime. From the slope $\rho^H/\rho_{\rm imp}$ in the linear regime, $\alpha_{\rm SH}$ was estimated with the standard 1D analysis above, and with more accurate 3D calculations, resulting in $\alpha_{\rm SH}(1{\rm D}) = -(0.12 \pm 0.04)$ and $\alpha_{\rm SH}(3{\rm D}) = -(0.24 \pm 0.09)$ at 10 K.

The 3D calculations yield a larger $\alpha_{\rm SH}$ because spin accumulation is observed to spread at the side edges of the CuBi/Cu junction, which is not taken into account in the 1D model. For the calculations with the 1D model, the spin current is considered to flow vertically into the CuBi wire, therefore, they cannot take into account the spin escape by lateral spreading. In general, the correction is observed to become important when the spin-diffusion length in N2 is longer than t_{N2}. For the cases of CuIr or Pt, it produces a small additional error because the spin-diffusion length in N2 is usually shorter than t_{N2}. For Pt, $\alpha_{\rm SH}$ was estimated to increase from 0.021 (1D model) to 0.024 (3D model).

Nonlocal methods have been used to estimate spin Hall angles in a number of other materials, including IrO_2 (Fujiwara *et al.*, 2013) and Bi (Fan and Eom, 2008). It was also applied to determine the sign of the spin-injection polarization of FMs by using materials with a well-established spin Hall angle, which is not possible with standard nonlocal spin injection and detection methods using the same FM material for the two electrodes. This procedure was demonstrated for the Heusler alloy Co_2FeSi (Oki *et al.*, 2012). The ISHE in nonlocal geometries was also used as a probe of spin fluctuations in weak FM NiPd alloys (Wei *et al.*, 2012). An anomaly near the Curie temperature was explained by the fluctuation contributions to skew scattering via spin-orbit interactions; the total magnetic moment involved in the experiment was extremely small (less than 10^{-14} emu), highlighting the very high sensitivity of the technique.

4. Direct detection of the spin Hall induced spin accumulation

As discussed in Sec. II.C, Zhang (2000) proposed to detect the spin accumulation induced by the SHE via a FM probe directly attached in the side of a thin conductor. The magnetization of the FM points to the direction perpendicular to the plane of the film. The method is based on measuring the voltage at which the FM floats depending on the direction of its magnetization, which gives direct information of the spin accumulation at the edge of the conductor (see Sec. IV.C.1). The implementation of the method took several years because of the local currents that circulate nearby the FM, which result in spurious signals that are avoided by the nonlocal methods, as described above.

Garlid *et al.* (2010) implemented devices based on epitaxial $Fe/In_xGa_{1-x}As$ heterostructures (Fig. 27). The active layers consisted of a 2.5-μm-thick Si-doped $[(3-5)\times10^{16}\,{\rm cm}^{-3}]$ channel, a highly doped Schottky tunnel barrier (5×10^{18} cm^{-3}), and a 5-nm-thick Fe layer. Heterostructures with In concentrations 0, 0.03, 0.05, and 0.06 were processed using lithographic and etching techniques into devices with 30-μm-wide channels oriented along the [110] direction, which is the x direction in Fig. 27.

It is technically difficult to fabricate a thin film with a FM attached at its edge with the magnetization orientation proposed by Zhang (2000). To circumvent this obstacle, Garlid *et al.* (2010) patterned pairs of Fe electrodes so that the centers of the contacts in each pair are 2, 6, or 10 μm from the edges of the channel. However, since the contacts are magnetized along x, and the spin polarization generated by the SHE is oriented along z, a magnetic field along y was applied to precess the spin accumulation into the x direction so that it could be detected. The spin accumulation is identified through

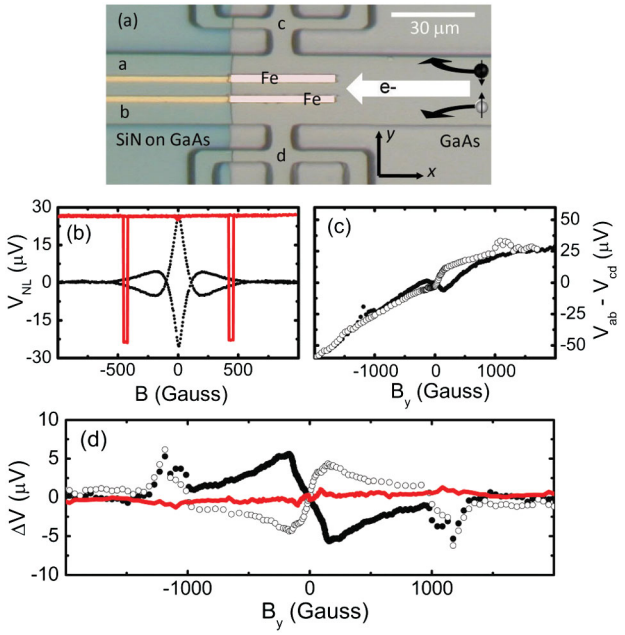

FIG. 27 (color online). (a) Micrograph of a spin Hall device with Fe contacts located 10 μm from the edges of the GaAs channel. The contact pairs ab and cd are used to measure the spin accumulation. (b) Nonlocal spin valve (colored lines) and Hanle effect (black dots) data obtained on a GaAs device at $T = 60$ K for injection current 8.2×10^2 A/cm^2. (c) Measured voltage $V_{ab} - V_{cd}$ for a GaAs device with Fe contacts 2 μm from the edges at $T = 30$ K for a channel current 5.7×10^3 A/cm^2. An offset voltage of 13.2 mV has been subtracted from the data. In (b) and (c), data are shown for both parallel and antiparallel states of injector and detector. (d) Spin Hall signal for both positive (full circle) and negative (open circle) currents, after removing background and extracting antisymmetric signal. The spin Hall signal in the antiparallel state is shown as the solid red line. From Garlid *et al.*, 2010.

the observation of the Hanle effect in the voltage measured between the pairs of FM contacts. The voltage first increases at low fields but then is suppressed due to spin dephasing in large fields.

The local character of the measurement causes a large background signal due to (i) imperfect cancellation of the background HE voltage induced by the applied magnetic field, (ii) local HEs due to fringe fields generated by the FM contacts, and (iii) because a small fraction of the channel current is shunted through the Fe contacts. The HE voltages were eliminated by using the expected symmetries of the signal, while the shunting effect was reduced by subtracting the voltages for the two current directions.

The results showed that the magnitude of the spin Hall conductivity was in agreement with models of the extrinsic SHE due to ionized impurity scattering. The bias and temperature dependences of the SHE indicated that both skew and side-jump scattering contribute to the total spin Hall conductivity. By analyzing the dependence of the SHE on channel conductivity, which was modified with the In content, Garlid *et al.* (2010) determined the relative magnitudes of the skew and side-jump contributions to the total spin Hall conductivity.

Ehlert *et al.* (2012, 2014) reported measurements of the SHE using a similar structure based on *n*-GaAs layers with relatively low carrier concentration (5×10^{16} cm^{-3}) and corresponding low conductivity. The FM voltage probes were implemented with (Ga,Mn)As/GaAs Esaki diode structures. The heterostructures were grown by molecular-beam epitaxy and consisted of a 1-μm-thick *n*-type transport channel, a 15-nm-thick $n \rightarrow n^+$ GaAs transition layer (5×10^{18} cm^{-3}), a 2.2-nm $Al_{0.36}Ga_{0.64}As$ diffusion barrier, and a 15-nm-thick layer of $Ga_{0.95}Mn_{0.05}As$. The highly doped (Ga,Mn)As/GaAs *p*-*n* junction forms an Esaki diode. This structure was covered on the top by 2 nm of Fe and 4 nm of Au. The purpose of Fe was to make the contacts harder magnetically, which helped to keep the magnetization aligned along their long axes during Hanle measurements. The values of spin Hall conductivities that were extracted are consistent with those calculated by Engel, Halperin, and Rashba (2005) but smaller than those observed by Garlid *et al.* (2010). Ehlert *et al.* (2012, 2014) observed that the combined results of these two experiments show that both the skew and side-jump contributions to the spin Hall conductivity cannot be treated as fully independent of the conductivity of the channel.

5. Spin Hall injection and detection without ferromagnets

Spin injection by the SHE combined with spin detection by the ISHE in one device (Hirsch, 1999) was successfully implemented by using a device geometry proposed by Hankiewicz *et al.* (2004). The original Hirsch (1999) proposal required a transverse strip connecting the edges of a slab on which spin accumulation was generated due to the SHE. A spin current would circulate in the transverse strip which would then generate a measurable voltage transverse to it [see also Sec. II and Fig. 2(c)]. The fabrication of such structure is challenging, albeit not impossible. Hankiewicz *et al.* (2004) considered the same concept but on a planar structure shaped as an H, which is much simpler to fabricate. The device and measurement principle is shown in Fig. 28 [see also Sec. II and Fig. 2(b)]. An electric current is applied in one of the legs of the H-shaped structure and generates a transverse spin current owing to the SHE. The spin current propagates toward the other leg through the connecting part and produces a measurable voltage via the ISHE. This nonlocal voltage in the second leg dominates local contributions if the separation between the legs is large enough. The structure was implemented experimentally by Mihajlovic *et al.* (2009) in Au; although no spin Hall signal was observed, the experiment set an upper bound for the spin Hall angle in this material. The first results associated with spin Hall signals were reported a year later by Brüne *et al.* (2010).

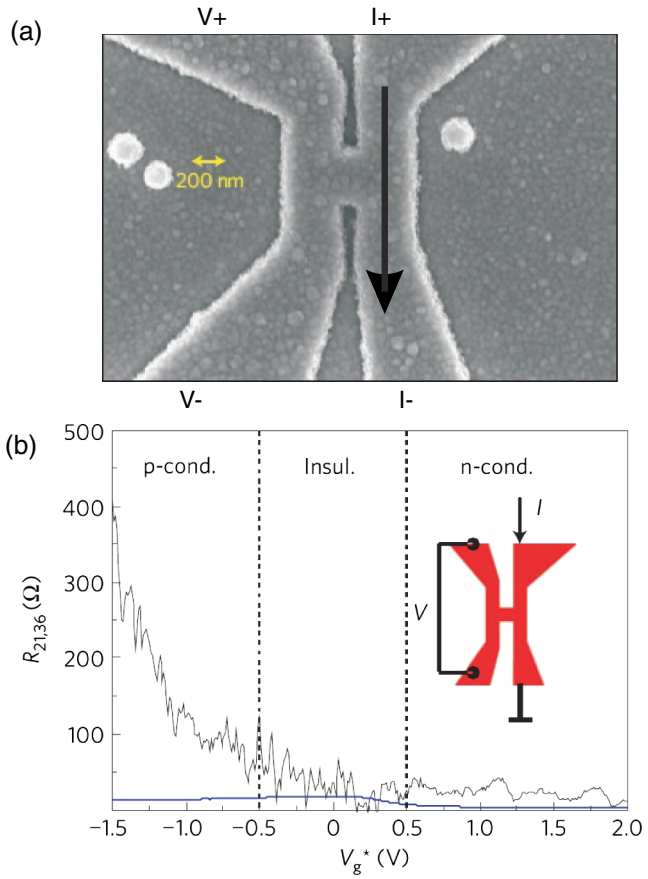

FIG. 28 (color online). (a) Scanning electron micrograph of an H-shape device and probe configuration for spin injection via SHE and spin detection via ISHE. (b) The inset indicates the measurement configuration for current injection (arrows) and voltage probes. The black curve in the main panel shows the nonlocal ISHE resistance signal. The solid curve indicates the residual voltage owing to current spreading. From Brüne *et al.*, 2010.

Brüne *et al.* (2010) used devices based on high-mobility HgTe/(Hg,Cd)Te quantum wells with a top gate electrode. The H structures consisted of legs 1 μm long and 200 nm wide, with the connecting part being 200 nm wide and 200 nm long. The estimated mean free path in the system was $\geq$2.5 μm, i.e., the samples were well within the quasiballistic regime. Sweeping the gate voltage in the sample allowed one to vary the strength of the Rashba spin-orbit coupling by a variation of both the electrical field across the quantum well and the Fermi level in the quantum well. In the sample it was possible to

electrically tune the carrier density from strongly *n*-type, through insulating, down to a *p*-type regime. This resulted in a strong modulation of the ISHE voltage, as shown in Fig. 28. In the *p* regime, where the spin-orbit coupling is strong, the signal is at least 1 order of magnitude larger than in the weakly spin-orbit-coupled *n* regime. Detailed numerical calculations confirmed that the observed spin Hall signals had the ballistic intrinsic origin (Brüne *et al.*, 2010).

An H-bar structure was also used in graphene devices (Abanin *et al.*, 2011). Here a large Hall response was observed near the graphene neutrality point in the presence of an external magnetic field. The results were ascribed to spin currents that resulted from the imbalance of the Hall resistivity for the spin-up and spin-down carriers induced by the Zeeman interaction; a process that does not involve a spin-orbit interaction, i.e., is not of the SHE origin, and that is largest in the cleanest graphene samples (Abanin *et al.*, 2011). More recently, the controlled addition of small amounts of covalently bonded hydrogen atoms has been reported to induce an enhancement of the spin-orbit interaction by 3 orders of magnitude in graphene (Castro Neto and Guinea, 2009; Balakrishnan *et al.*, 2013). Such large enhancement was estimated from nonlocal signals of up to 100 Ω, which are observed at zero external magnetic fields and at room temperature. From the magnetic field and the length dependence of the nonlocal signal, a spin-orbit strength of 2.5 meV was extracted for samples with 0.05% hydrogenation. Similar results were observed by Balakrishnan *et al.* (2014) in graphene grown using chemical vapor deposition (CVD). Estimations of a spin-orbit coupling as high as 20 meV and spin Hall angle ∼0.2 were reported. They argued that the observations are due to the presence of copper contamination in CVD graphene, which act as local spin-obit scattering centers in the resonant limit. This hypothesis is tested independently by introducing metallic adatoms, such as copper, silver, and gold on exfoliated graphene samples. Even though the nonlocal signal is absent in exfoliated graphene, it is clearly observed once any of the previous adatoms is introduced, resulting in calculated spin Hall angles ∼0.2 in all cases, rivaling the largest values observed in metals.

6. Spin Hall magnetoresistance

In bilayer FM-NM systems, a new type of magnetoresistance has been recently discovered which is directly associated with the SHE (Huang *et al.*, 2012; Weiler *et al.*, 2012). The observed magnetoresistance is given by

$$\rho = \rho_0 + \rho_1[\hat{m}\cdot(\hat{j}\times\hat{z})]^2, \tag{4.1}$$

where ρ_0 is the normal resistance, ρ_1 is the anisotropic resistance amplitude, and $\hat{j}$, $\hat{m}$, and $\hat{z}$ are the directional vectors of the current, the magnetization, and the normal to the interface. This means that the magnetoresistance depends on the in-plane component of the magnetization perpendicular to the current. In contrast, the conventional noncrystalline AMR (McGuire and Potter, 1975) has the form of

$$\rho = \rho_0 + \rho_1(\hat{j}\cdot\hat{m})^2, \tag{4.2}$$

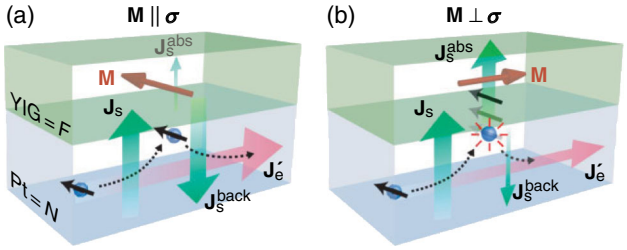

FIG. 29 (color online). Illustration of the SHE magnetoresistance. (a) When the magnetization aligns with the polarization of the SHE spin current, its backflow reflection generates an ISHE current that contributes to the longitudinal current. (b) When the magnetization is perpendicular to polarization of the SHE spin current, the spin current is absorbed and no ISHE current affects the longitudinal current. From Nakayama *et al.*, 2013.

with $\hat{j}\cdot\hat{m} = \cos(\theta_{j-m})$, where θ_{j-m} is the angle between the current and the magnetization.

This phenomenon has been termed the spin Hall magnetoreristance (SHMR) (Weiler *et al.*, 2012; Chen, Matsukura, and Ohno, 2013; Hahn *et al.*, 2013; Nakayama *et al.*, 2013; Vlietstra *et al.*, 2013; Isasa *et al.*, 2014). Its origin is illustrated in Fig. 29. When a current flows parallel to the FM-NM interface, a SHE spin current is generated in the NM directed to the interface. If the magnetization is parallel to the polarization of the spin current generated by the SHE, it gets reflected at the interface and a spin current back flows, as shown in Fig. 29(a). This backflow spin current then gets transformed into a charge current via the ISHE in the direction of the longitudinal current. If the magnetization is instead perpendicular to the polarization of the spin current generated by the SHE, it can enter the FM and dephase, as shown in Fig. 29(b). In this case there is no spin-current backflow and no contribution via the ISHE to the longitudinal current in the NM.

The typical experimental results are illustrated in Fig. 30, where the bilayer system was YIG/Pt. The magnetoresistance traces are measured as a function of the magnetization angle in the *x*-*y* plane parallel to the interface, and in the *z*-*y* and *z*-*x* planes that are perpendicular to the interface. The measured angular dependencies are consistent with the SHMR phenomenology described by Eq. (4.1) and are inconsistent with the AMR expression (4.2). The theory of the effect was derived by Chen, Matsukura, and Ohno (2013) based on the scattering formalism and the spin-charge drift-diffusion equations.

D. Spin Hall effect coupled to magnetization dynamics

When the SHE is studied by coupling to magnetization dynamics three different FMR-based techniques can be found: (i) ferromagnetic resonance-spin pumping (FMR-SP), (ii) modulation of damping (MOD) experiments, and (iii) spin Hall effect-spin-transfer torque (SHE-STT). The general underlying principle for the three methods is similar. In a bilayer NM-FM structure, the FM is used to inject or absorb a dynamic spin current into or from the NM. Note that these studies have been also extended to replacing the SHE-ISHE generating NM with another FM (Freimuth, Blügel, and

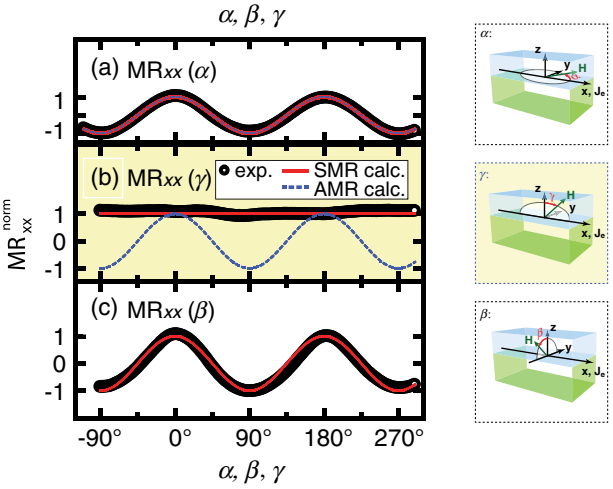

FIG. 30 (color online). Magnetoresistance curves as a function of the angles (a) α, (b) γ, and (c) β, illustrated in the right panel. The key contrast to conventional AMR is the trace in (b), where no dependence is observed, while conventional AMR would give the sinusoidal form illustrated in the dashed line. From Nakayama *et al.* (2013).

Mokrousov, 2010; Miao *et al.*, 2013; Azevedo *et al.*, 2014; Mendes *et al.*, 2014) or antiferromagnet (Zhang *et al.*, 2014).

In FMR-SP, a spin current is injected from the FM into the NM. The injected spin current is a pure ac spin current which is not accompanied by a charge current but which nevertheless can be detected electrically since it is converted into a charge current by means of the ISHE in the NM (Saitoh *et al.*, 2006). The efficiency of the conversion process can be quantified by the spin Hall angle. Since in the process of spin injection angular momentum is lost in the FM, the FMR-SP leads to a broadening of the FMR line (Mizukami, Ando, and Miyazaki, 2001; Urban, Woltersdorf, and Heinrich, 2001; Heinrich *et al.*, 2003), whereas the backflow of spin current into the ferromagnet generates a dc voltage that can also be used to detect SP (Wang *et al.*, 2006) as was experimentally demonstrated by Costache, Watts, Sladko, van der Wal (2006) and Miao *et al.* (2013). Note that an additional contribution that might have to be taken into account in special cases arises from the SGE as has recently been demonstrated for the Ag/Bi interface (Rojas-Sánchez, Vila *et al.*, 2013; Zhang *et al.*, 2015) and in FM-topological insulator surface state system (Fan *et al.*, 2014; Mellnik *et al.*, 2014).

In MOD experiments, the direct SHE induced in the NM by a dc electrical current is used to modify the damping in the FM which is concomitantly driven into FMR by the application of an rf magnetic field. In this approach, the dc spin current generated by the SHE and injected across the NM-FM interface leads to a damping or anti-damping-like torque acting on the precessing magnetization of the FM. Modulation of the damping is observed as a function of the applied dc charge current and a detailed line-width analysis allows extraction of the spin Hall angle (Saitoh and Ando, 2012). Note that the pure dc spin current is generated in the bulk of the NM and that in order to quantitatively determine the spin Hall angle it is important to know the transmissibility of the NM-FM interface for the pure spin current.

In the SHE-STT, a spin current is used to transfer spin angular momentum and thus to exert a torque on the magnetic moments. In these experiments an ac current sent along the NM-FM interface can create an rf excitation of the magnetization of the FM via the SHE-STT. In conventional STT junctions, an electrical current is sent perpendicular to a stack with two FM electrodes to transfer angular momentum from one FM to the other FM (Ralph and Stiles, 2008). SHE-STT experiments, on the other hand, exploit the use of a perpendicular pure spin current generated by an in-plane electrical current in the attached NM via the SHE.

In both the MOD experiments and the SHE-STT, the torques in the FM that are generated by the SHE in the NM would be in addition to the ISGE-related SOTs present at the inversion asymmetric FM-NM interface (Garello *et al.*, 2013; Freimuth, Blügel, and Mokrousov, 2014; Kurebayashi *et al.*, 2014). Hence, in these experiments the spin Hall angle is in reality a parametrization of the total torques generated by the currents and therefore it should be considered instead as the effective spin Hall angle for the specific bilayer system. As mentioned above, similarly spin pumping and detection of the spin Hall angle via the ISHE may be affected by the SGE arising from the specific bilayer interface.

In the rest of the section we expand on the details and recent results of each of these FMR-based techniques. FMR-SP is the more widely used technique to measure the effective spin Hall angle thus we detail this technique more extensively.

1. Ferromagnetic resonance spin pumping

As described in the theory section (Sec. III.D), Tserkovnyak, Brataas, and Bauer (2002a) and Tserkovnyak, Brataas, and Halperin (2005) showed that the precessing magnetization in a FM generates a spin current strictly at the FM-NM interface, as sketched in Fig. 31. The spin current generated at the interface propagates into the NM and consequently decays on a length scale connected to the effective spin-diffusion length λ_{sd} of the NM. As mentioned in the theory section, we note that the term effective is used

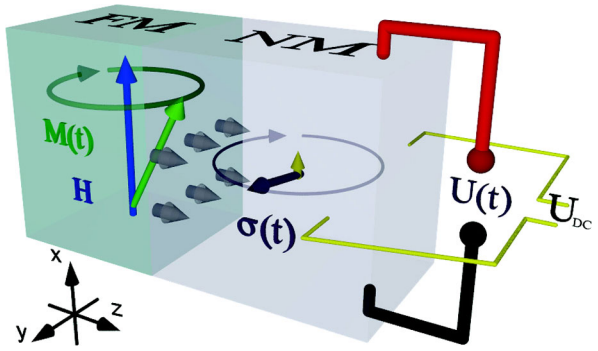

FIG. 31 (color online). A spin current is generated by SP at the FM-NM interface (gray arrows). The time-dependent spin polarization of this current (indicated as a dark gray arrow) rotates almost entirely in the y-z plane. The small time-averaged dc component (small upward arrow) appears along the x axis. Both components lead to charge currents in NM and can be converted into ac and dc voltages by placing probes along the x and the y direction, respectively. From Wei *et al.*, 2014.

here, since the determination of the spin-diffusion length for a NM interfaced with a FM may also be connected to spin memory loss and proximity polarization at the interface. In the case of Pt and Pd in contact with a FM metal, proximity effects are well known from x-ray magnetic circular dichroism experiments.

The direction of the injected pure spin current points from the FM to the NM and its polarization is time dependent. Its projection onto the static magnetization direction of the FM leads to a small dc component of the injected spin current into the NM. Performing time averaging one obtains a net dc spin current given by Eq. (3.26) from Sec. III.D,

$$j_{s,\mathrm{dc}} = \frac{\hbar\omega}{4\pi}\tilde{A}_r \sin^2\Theta,$$

where ω is the driving rf and Θ is the cone angle of precession. Here $\tilde{A}_\mathrm{r}$ is the effective SP conductance. If the thickness of the NM is smaller than the spin-diffusion length, the build-up of spin accumulation will yield a backflow spin current which will reduce the total spin current into the NM. The SP conductance $\tilde{A}_r$ is proportional to the real part of the mixing conductance, discussed in Sec. III.D, and is reduced by this backflow. The reduction depends on the ratio $\tau_{\mathrm{tr}}/\tau_{\mathrm{sf}}$, the reduction being strongest as this ratio increases. Hence, the effective spin-mixing conductance may become small even though a pure spin current is efficiently transferred across the FM-NM interface. Recently, spin-flip scattering near the FM-NM interface has been divided up into a spin memory loss occurring directly at the interface (interface scattering) and the decay of the spin polarization as described above (Rojas-Sánchez *et al.*, 2014).

The ISHE is used to electrically detect pure spin currents generated by the SP (Saitoh *et al.*, 2006), as shown Fig. 32. In spin-orbit-coupled NMs like Pt or Pd, the ISHE converts the pure spin current into a detectable charge current given by Eq. (3.34), Sec. III.D,

$$\mathbf{j}_c = \alpha_{\mathrm{SH}}\frac{2e}{\hbar}\mathbf{j}_s \times \boldsymbol{\sigma}(t).$$

Here the vector of the spin-current density $\mathbf{j}_\mathrm{s}$ points perpendicular to the NM-FM interface into the NM. Note that the vector of the spin-current polarization $\boldsymbol{\sigma}(t)$ is a time varying quantity, which we do not average here, since it has now been demonstrated that the ac component is also measurable (Wei *et al.*, 2014; Weiler *et al.*, 2014). In Fig. 32, only the dc component of the spin-current polarization is depicted.

To measure the effect of the injected spin current via ISHE, i.e., to measure the generated charge current, contact electrodes have to be attached to the sample. If the coordinate system of Fig. 31 is considered, placing electrodes along the y direction allows detecting the small dc component of the SP-induced ISHE. In contrast, if the contact electrodes are attached along the x direction, the much larger ac component in the GHz frequency range can be detected when high frequency lines are used.

In case of dc detection the time-averaged dc component of the injected spin current pointing along the x direction

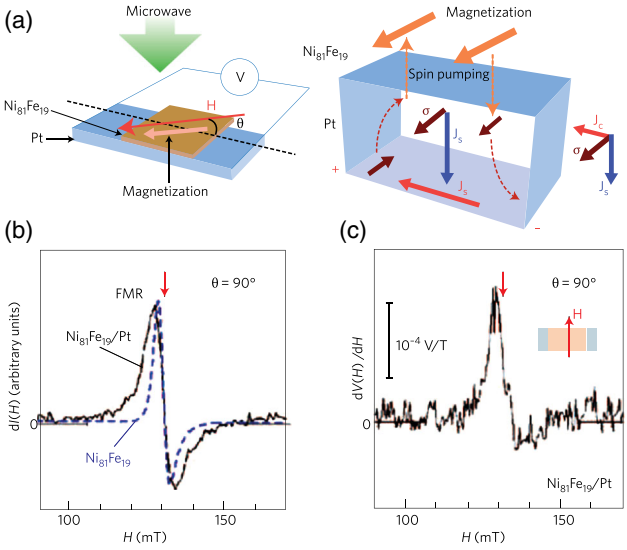

FIG. 32 (color online). Observation of the ISHE in a metal device with spin injection from a FM by FMR-SP. (a) Schematic illustration of the NiFe/Pt sample system used in the study and of the SP effect and the ISHE. (b) Magnetic-field dependence of the FMR signal for the NiFe/Pt bilayer film and a bare NiFe film. I denotes the microwave absorption intensity. (c) Magnetic-field dependence of $dV(H)/dH$ for the NiFe/Pt sample. V denotes the electric-potential difference between the electrodes on the Pt layer. From Saitoh *et al.*, 2006.

(arrow in Fig. 31) leads to a charge current which is converted to a potential drop across the resistance of the NM and can be measured as a voltage signal. When performing FMR-SP experiments not only voltages due to ISHE are generated, but also due to the AMR or the AHE. Thus, great care has to be taken to disentangle these contributions.

In the geometry sketched in Fig. 31 the propagation direction of the spin current is along z and its polarization is along the x direction. Equation (3.35) is then used to convert between this spin current and the measured voltage.

In the original experiments by Saitoh *et al.* (2006), the bilayer is placed in a FMR cavity in which the magnetic-field component of the microwave mode with frequency 9.45 GHz is maximized while the electric-field component is minimized. The voltage probes are placed on the sides of the millimeter-sized sample (see Fig. 32). A similar setup was used by Azevedo *et al.* (2011). Here the sample is rotatable in the cavity and the cavity (i.e. the direction of the rf excitation field) is kept fixed with respect to the dc external magnetic field. This experimental geometry has advantages and disadvantages. The main advantage is that it is possible to find an in-plane angle between excitation rf field and angular position of the voltage probes where the AMR contribution to the signal vanishes exactly while ISHE is detectable. Second, in the in-plane excitation geometry typically used, the sensitivity is large due to the large in-plane susceptibility at FMR. A major disadvantage is that it is not easy to perform frequency dependent measurements and that due to the use of a cavity the exact amplitude of the excitation field, and thus the cone angle of precession which enters Eq. (3.26) in Sec. III.D, is usually not well known. Finally, since typically large, millimeter-sized samples are used in the experiments, spurious rf electric fields

may lead to additional contributions due to the AHE. It is therefore not straightforward to obtain an exact quantitative value of the spin Hall angle from cavity FMR-type measurements.

In the experiments shown in Fig. 32, the measured FMR spectrum of the NiFe/Pt sample is compared to a reference NiFe sample [see Fig. 32(b)]. The FMR linewidth of the NiFe/Pt sample is larger than that of the reference NiFe film which demonstrates the presence of the SP effect in the NiFe/Pt. The induced voltage signal measured simultaneously across the sample along an axis parallel to the NiFe/Pt interface is shown in Fig. 32(c). Saitoh *et al.* (2006) and Ando *et al.* (2008) demonstrated that the signal is present only when the spin-polarization vector of the injected spin current has a component perpendicular to the measured electric field across the sample, consistent with the ISHE.

Ando *et al.* (2009) reported electrical detection of a spin wave resonance in nanostructured NiFe/Pt samples. Electrical tuning of the spin signal in a semiconductor has been recently demonstrated also by Ando, Takahashi, Ieda, Kurebayashi *et al.* (2011). In the experiment, spins were injected from NiFe into GaAs through a Schottky contact using the FMR-SP. Tuning of the SP efficiency was achieved by applying a bias voltage across the NiFe/GaAs Schottky barrier and interpreted as a consequence of a suppressed or enhanced spin coupling across the interface. The FM-semiconductor SP experiments in Ando, Takahashi, Ieda, Kurebayashi *et al.* (2011) were performed also on samples with an Ohmic contact between NiFe and GaAs. The measurements indicate that the resistance mismatch problem in Ohmic metal-semiconductor spin-injection devices can be circumvented by using the FMR-SP technique. Similar experiments have recently been performed also for spin injection into Si (Ando *et al.*, 2010), Ge (Jain *et al.*, 2012) and organic semiconductors (Watanabe *et al.*, 2014). The latter one shows a surprisingly long spin coherence in the hopping regime and opens new possibilities in organic spintronics.

A second possibility to quantify the spin Hall angle has been pioneered by Mosendz, Pearson *et al.* (2010). They used a microstructured coplanar wave guide (CPW) with integrated bilayer structure on top of the center wave guide. This geometry allows excitation of FMR in the FM layer over a wide frequency range while the driving rf field is in the plane of the bilayer at 90° to the long axis of the several hundred micrometer long device (see Fig. 34). The use of a wave guide structure allows precise knowledge of the amplitude of the rf fields and thus the cone angle of the precessing magnetization. Voltage pickup at the ends of the wire are used, perpendicular to the direction of the rf driving field. Mosendz, Pearson *et al.* (2010) applied the external magnetic bias field at an angle of 45° to the long axis of the wave guide. In this experimental geometry both ISHE and AMR signals are detected at the voltage probes as can be seen directly in the recorded voltage traces (see Fig. 33).

AMR leads to a parasitic dc voltage signal at FMR due to the mixing of the time-dependent resistivity (AMR and precessing magnetization) with a capacitively or inductively coupled microwave current $I(t)$ in the bilayer. The AMR of the bilayer can be taken into account by considering the orientation of the magnetization with respect to the current

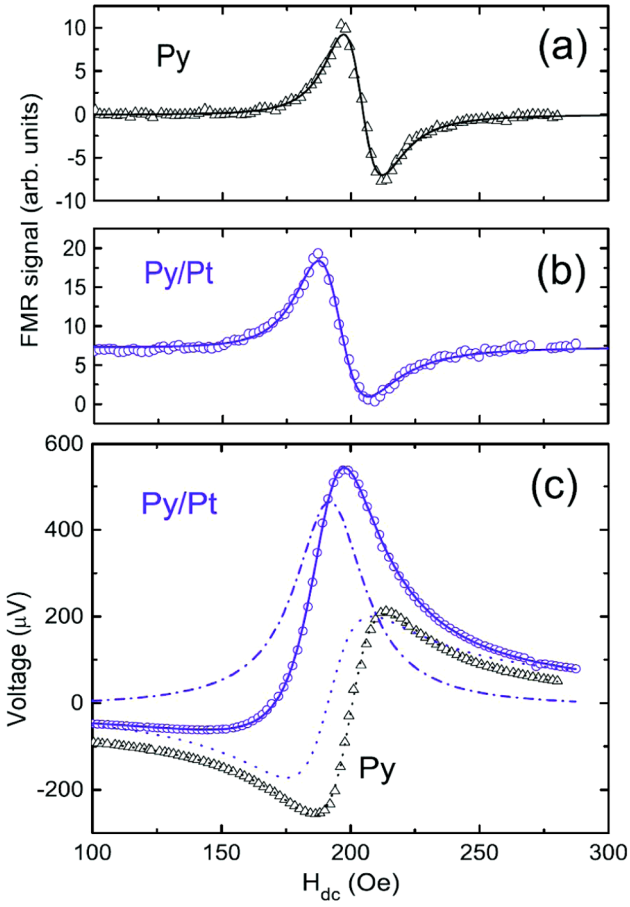

FIG. 33 (color online). (a),(b) Derivative of FMR spectra for Py/Pt (open circles) and Py (black triangles). The solid lines are fits to a Lorentzian FMR absorption function. (c) Voltage along the samples vs field dc magnetic field (Py/Pt: open circles; Py: black triangles). Dotted and dashed lines show the decomposition of the spectrum into a symmetric (ISHE) and antisymmetric (AMR) contribution. The solid line shows the combined fit for the Py/Pt sample. From Mosendz *et al.*, 2010a.

direction: $R_A = R_\parallel - R_\perp$. The general formula describing the parasitic voltage pick-up due to the AMR is given by $\langle V(t)\rangle = \langle I(t) R_A \alpha_{ip}(t) \sin(2\varphi_H)\rangle$, (Costache, Sladko, Watts, van der Wal *et al.*, 2006; Mecking, Gui, and Hu, 2007; Obstbaum *et al.*, 2014) and it follows that this time-averaged dc voltage is to first order proportional to the in-plane dynamic cone angle of the magnetization $\alpha_{ip}(t)$. The cone angle of precession can easily be calculated from the simultaneously measured susceptibility at FMR in the exactly known geometry of the CPW structure. The angle φ_H is defined in Fig. 34. Note that according to Bai *et al.* (2013), spurious effects due to the AMR can be excluded by carefully analyzing the high frequency characteristics of the CPWs used in the experiments with in-plane excitation, leading to a quantitative determination of the spin Hall angles.

Another possibility is to place the bilayer in the gap of the CPW (see Fig. 34). Now the in-plane dynamic cone angle relevant for the AMR is given by $\alpha_{ip}(t) = \chi_{y'y'} h_x(t) \sin(\varphi_H) + \chi_{y'z} h_z(t)$. The formula contains both in-plane and out-of-plane magnetic fields, together with the corresponding tensor elements of the susceptibility (χ_{ij}). Since the out-of-plane

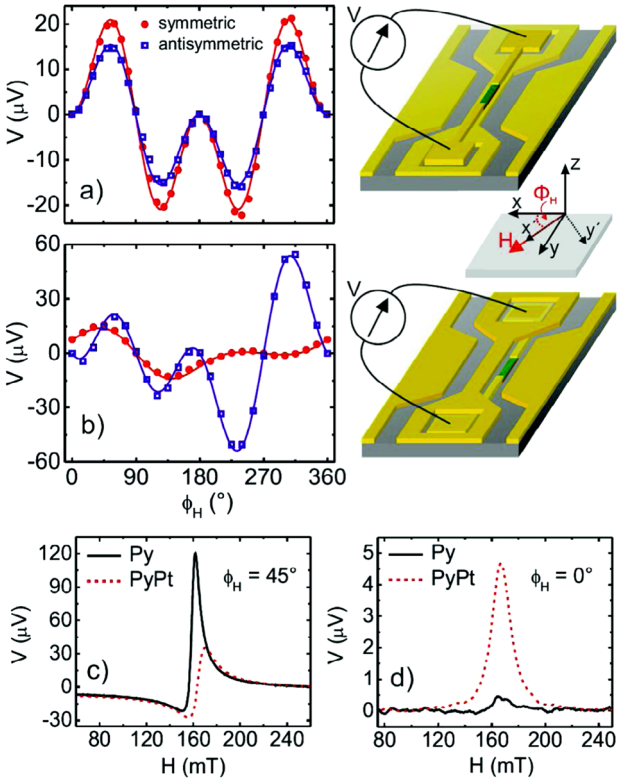

FIG. 34 (color online). Symmetric (dots) and antisymmetric (open squares) voltage signals amplitudes at FMR (at 12 GHz) for a Py/Pt bilayer as a function of angle φ_H. In (a) the magnetic excitation field is in-plane placing a Py/NM bilayer on top of the signal line of a CPW. Both symmetric and antisymmetric amplitudes obey a $\sin(\varphi_H)\sin(2\varphi_H)$ behavior. (b) The magnetic excitation field generated by the CPW is out-of-plane with respect to the Py/Pt layers. The amplitudes of the antisymmetric part follow a $[a\sin(\varphi_H)+b]\sin(2\varphi_H)$ behavior. The symmetric part obeys $[c\sin(\varphi_H)+d]\sin(2\varphi_H)+e\cos(\varphi_H)$, which reflects the fact that the symmetric part is due to AMR and ISHE. (c) Voltage at FMR for $\varphi_H = 45°$, and (d) $\varphi_H = 0°$ for a single Py layer and a Py/Pt bilayer. From Obstbaum *et al.*, 2014.

field produced by the CPW is about 3 orders of magnitude larger than its in-plane component, one is tempted to simply neglect the terms arising form the in-plane field. This approach is justified as long as only a single layer is studied. However, as soon as a FM-NM bilayer with a highly conductive NM is used, the inductively or capacitively coupled microwave current largely flows in the NM and therefore generates an in-plane Oersted field of the same frequency and phase and with an amplitude comparable to the rf field generated by the CPW. Hence the rf current distribution in the bilayer has a significant effect on the magnetization dynamics in the FM layer and can even be the dominating source of dc voltage generation by the AMR (Obstbaum *et al.*, 2014). Using standard electromagnetic wave simulation codes, the rf magnetic-field contribution can be calculated rather accurately.

When performing angular-dependent measurements, the symmetric and antisymmetric contributions due to the ISHE and the AMR can be traced [see Figs. 34(a) and 3(b)]. While for in-plane excitation the signal shows the same angular dependence, for the out-of-plane excitation case the antisymmetric contribution can be suppressed completely at an angle of $\varphi_H = 0$ [see Fig. 34(d)]. The voltage contribution at this angle is thought to arise from ISHE exclusively and allows quantitative determination of the spin Hall angle. Note that in these measurements both symmetric and antisymmetric contributions can be observed in a bare FM layer when the angle is set to $\varphi_H = 45°$ [see Fig. 34(c)].

2. Spin Hall effect modulation of magnetization damping

A MOD experiment that is the inverse of the FMR-SP was proposed by Ando *et al.* (2008). In the MOD described in Fig. 35, a FM-NM bilayer (in this case Py/Pt) is placed in a microwave cavity (frequency 9.4 GHz) and subjected to an rf driving field. By adjusting the external field, the bilayer can be brought into FMR. A typical FMR trace $dI(H)/dH$ is shown in Fig. 35(b). The direction of the external magnetic field encloses an angle θ with the direction of current flow. Since the mm-sized sample consists of 10 nm NiFe and 10 nm Pt, the effect of SP which contributes to the relaxation of the precessing magnetization can be observed as a linewidth broadening when comparing to the data obtained for a plain NiFe film. Figure 35(c) illustrates the effect of a dc current sent through the bilayer sample due to the combined action of the SHE and STT. Because of the SHE a spin current is generated in the Pt layer and enters the NiFe film. Its flow direction is perpendicular to the interface and its polarization direction $\boldsymbol{\sigma}$ depends on the direction of the current flow. The

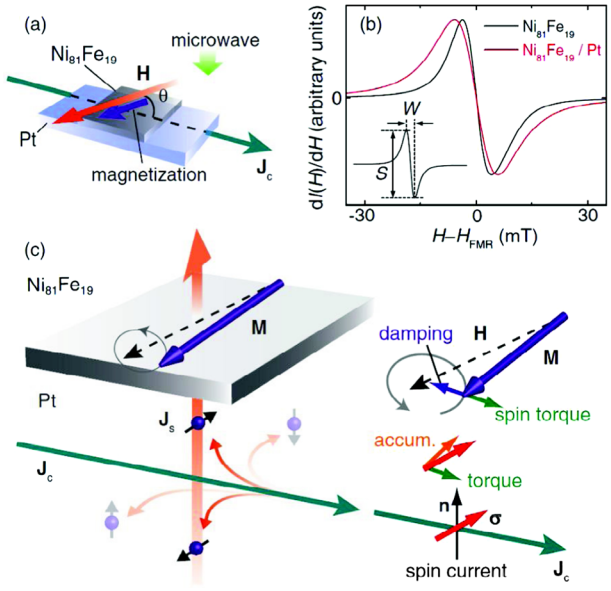

FIG. 35 (color online). (a) A schematic illustration of the MOD experiment to determine the spin Hall angle. H is the external magnetic field, and J_c represents the applied electric current density. (b) Magnetic-field dependence of the FMR signal for a NiFe/Pt bilayer film and a pure NiFe film. Note the linewidth broadening for NiFe/Pt due to SP. (c) Schematic illustration of the spin Hall and the spin torque effects. $\mathbf{M}$, $\mathbf{J}_s$, and σ denote the magnetization, the flow direction of the spin-current density, and the spin-polarization vector of the spin current, respectively. From Ando *et al.*, 2008.

spin current exerts a torque on the precessing magnetization which either adds to the damping torque or opposes it. The effect is maximized when the external magnetic field points perpendicular to the direction of current flow. For the situation sketched here, the spin-current density can be written as $\mathbf{j}_s = \alpha_{\mathrm{SH}}(\hbar/2e)|\mathbf{j}_c|\boldsymbol{\sigma}$. The effect of the injected spin current on the precessing magnetization can be modeled in terms of an additional STT contribution to the Landau-Lifshitz Gilbert equation (Ando *et al.*, 2008; Liu *et al.*, 2011) that has to be added on top of the SP contribution,

$$\tau_{\mathrm{STT}} = -\mu_0\gamma\alpha_{\mathrm{SH}}\eta\frac{\hbar}{2e}\frac{j_c}{\mu_0 M_s^2 d_{\mathrm{Py}}}\mathbf{M}\times(\mathbf{M}\times\boldsymbol{\sigma}). \quad (4.3)$$

Here d_{Py} is the thickness of the Py layer. For simplicity, the factor

$$\kappa = \alpha_{\mathrm{SH}}\eta\frac{\hbar}{2e}\frac{j_c}{\mu_0 M_s^2 d_{\mathrm{Py}}} \quad (4.4)$$

is introduced. Note that this factor is dimensionless and $\kappa < 0$ for $j_c > 0$ due to the negative electron charge. The parameter η defines the so-called injection efficiency and contains the effects of spin-current losses near the interface. There is no consensus on the exact ingredients for this parameter, so it could be useful to use $\eta \times \alpha_{\mathrm{SH}}$ as an effective quantity parametrizing the STT efficiency.

Figure 36 shows the MOD experimental findings. When a current flows through the FM-NM bilayer, the STT generated by the spin current traversing the NM-FM interface due to the SHE alters the FMR linewidth when the current flow direction and the external magnetic-field direction enclose an angle of 90° while no effect is observed for collinear orientation, consistent with the theoretical expectation.

Similar experiments have been performed by Demidov, Urazhdin, Edwards, Demokritov (2011) and Demidov, Urazhdin, Edwards, Stiles *et al.* (2011) using Brillouin light scattering methods. The key finding in these experiments is the control of the FMR linewidth of the FM film by employing the SHE which generates a pure spin current in the adjacent NM. Ultimately, in suitable nanostructured materials, the application of a large enough charge current density should lead to the generation of coherent auto-oscillations in the FM nano object due to a dc charge current (Demidov *et al.*, 2012; Liu, Pai, Ralph, Buhrman, 2012b; Liu, Lim, and Urazhdin, 2013; Duan *et al.*, 2014; Hamadeh *et al.*, 2014). These magnetization induced nano-oscillators are of particular interest in the research of tunable microwave sources.

3. Spin Hall effect: Spin-transfer torque

Finally, a third FMR technique has been employed that allows accessing the spin Hall angle experimentally. Liu *et al.* (2011) applied a microwave frequency charge current in the plane of a NiFe/Pt sample and observed the FMR in NiFe. Because of the action of the SHE a transverse spin current is generated in the NM, in this case Pt, which is injected into the FM layer. Consequently, an oscillatory STT acts on the magnetic moments in the FM, inducing precession of the magnetization (see Fig. 37). The oscillatory magnetization in the FM leads to an oscillatory AMR which in turn leads to an oscillatory resistance. This high frequency resistance mixes with the rf current and leads to a detectable dc voltage across the device which can be picked up using a bias tee [Fig. 37(c)].

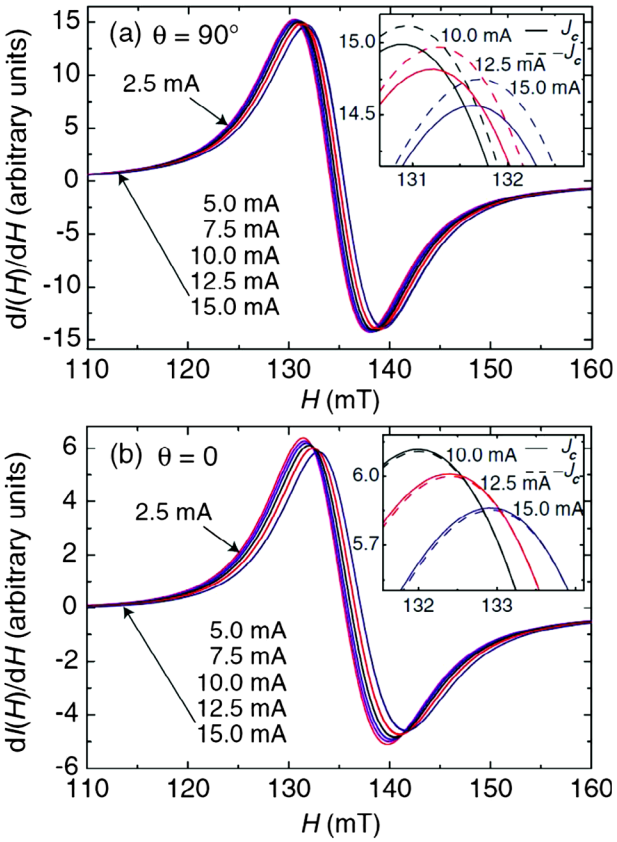

FIG. 36 (color online). FMR spectra for the NiFe/Pt bilayer measured at various electric current density values J_c when the magnetic-field direction is (a) 90° and (b) 0°. The inset shows magnified views around the peaks of the spectra, where the solid and dashed curves are the FMR spectra measured with electric current densities J_c and $-J_c$, respectively. From Ando *et al.*, 2008.

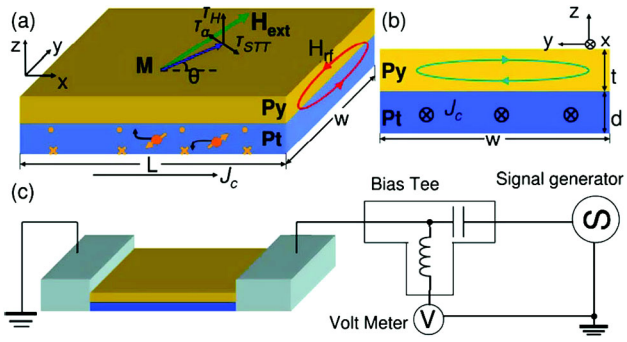

FIG. 37 (color online). (a) Schematic of Pt/Py bilayer thin film illustrating the STT induced by the SHE rising from the rf current through NM as well as the damping torque and the torque due to the Oersted field when the magnetization of FM is aligned in an external magnetic field. (b) The dimensions of the sample and the Oersted field due to a current flowing through FM. (c) The electrical measurement scheme. From Liu *et al.*, 2011.

In these experiments the external magnetic field is typically fixed at an angle of 45° and swept in the plane of the films to achieve the FMR condition. In the setup, different torques act on the magnetization of the FM which is aligned along the magnetic-field direction as depicted in Fig. 37(a). The torques include all the STTs due to the SHE in the NM, the torque induced by the Oersted field due to the rf current through the device, and the torque already modified by SP. We also emphasize that the torques generated by the SHE in the NM would be in addition to the ISGE-related SOTs present in the FM near the interface (Garello *et al.*, 2013; Freimuth, Blügel, and Mokrousov, 2014; Kurebayashi *et al.*, 2014).

Landau-Lifshitz-Gilbert equations including all relevant torques can be used to model the dc voltage response of the bilayer device and the result shows that the mixing voltage contains the contributions of symmetric and antisymmetric Lorentzian lines (Liu *et al.*, 2011). According to Liu *et al.* (2011), the detailed analysis of the resonance properties of this voltage enables a quantitative measure of the spin current absorbed by the FM and of the spin Hall angle. Liu *et al.* (2011) showed that the ratio of the symmetric to antisymmetric components of the resonance curve, when scaled properly by material parameters like the saturation magnetization, thickness and width of the FM, and the external magnetic field, is linked to the ratio of spin and charge currents and thus to the spin Hall angle. They emphasized that the measurement method is (in a reasonable thickness regime of the FM and the NM) self-calibrating since the strength of the torque from the spin current is measured relative to the torque from the rf magnetic field, which can be calculated from the geometry of the sample. The same method has been applied to various combinations of FMs and NMs (Liu *et al.*, 2011; Liu, Pai, Li *et al.*, 2012; Pai *et al.*, 2012).

Also in these types of experiments the tunability of the effective damping parameter has been demonstrated by Liu *et al.* (2011) and Kasai *et al.* (2014). An example is illustrated in Fig. 38 for the case of Py/Pt where the effective damping parameter is shown to be tunable as a function of the current direction and amplitude (Liu *et al.*, 2011).

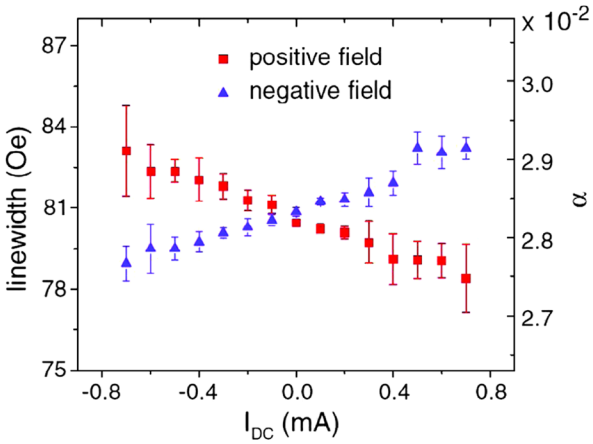

FIG. 38 (color online). Effective damping as a function of current density through the Pt layer in a Py(4 nm)/Pt(6 nm) bilayer. From Liu *et al.*, 2011.

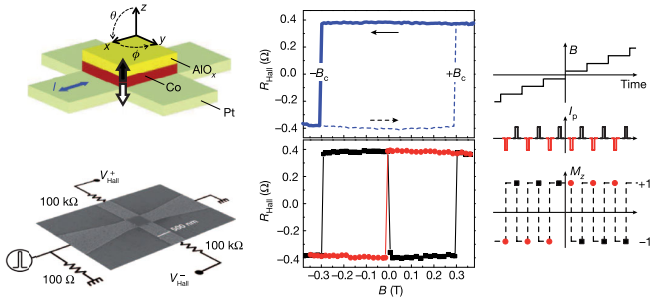

FIG. 39 (color online). Top left: device schematic and current-induced switching. Hall-cross geometry. Black and white arrows indicate the up and down equilibrium magnetization states of the Co layer, respectively. Bottom left: scanning electron micrograph of the sample and electric circuitry used in the measurements. Shown are the terminals for the Hall voltage measurements as well as the current line where a pulsed current is applied for the switching experiments. Middle: the state of the perpendicular magnetization is measured via the anomalous Hall resistance as a function of applied field B. After injection of positive (squares) and negative (circles) current pulses of amplitude $I_p = 52.58$ mA the Hall resistance is measured. The data are reported during a single sweep of B. Right: the measurement schematics and pulse sequence. From Miron, Garello *et al.*, 2011.

4. Spin Hall effect induced switching of the magnetization

For sufficiently large current densities pushed through the NM and large spin Hall angles, it is possible to even reverse the magnetization in a FM nanoelement placed on top of the NM current carrying line, as has been demonstrated by Miron, Garello *et al.* (2011) and Liu, Pai, Li *et al.* (2012) (see Figs. 39 and 40). In these experiments it is important to use a NM-FM combination where, when placing the NM in contact with the FM, the induced damping due to SP remains negligible. This is the case for CoFeB/Ta (Fig. 40). On the one hand, β-Ta shows a giant spin Hall angle (Liu, Pai, Li *et al.*, 2012), on the other hand, enhancement of damping due to SP is not observed in the CoFeB layer. Furthermore, due to the large resistivity of the CoFeB layer a large portion of the applied current is pushed through the Ta layer where it produces the pure spin current due to the SHE. Another important feature is that the bilayer is capped with MgO to induce a large perpendicular anisotropy in CoFeB. The thin layer of MgO (1.6 nm) is used as a tunnel barrier between the thin CoFeB free layer (1.6 nm) and the thicker CoFeB reference layer (3.8 nm) so that the tunneling magnetoresistance (TMR) effect can be used to determine the relative orientation of their magnetization.

In earlier experiments using ultrathin FM layers, Miron *et al.* (2010) and Miron, Garello *et al.* (2011) demonstrated similar results. Their devices are based on the Pt/Co/AlO_x system with ultrathin Co layers of a thickness of only 0.6 nm sandwiched between Pt (3 nm) and AlO_x (1.6 nm). The use of ultrathin Co in contact with Pt leads to a strong perpendicular anisotropy. When a current is driven through the Pt layer, switching of the Co magnetization can be observed by monitoring the AHE of the device (see Fig. 39). In the original interpretation the driving force for the observed switching was thought to arise mostly from the Rashba symmetry ISGE due to the broken inversion symmetry along the growth direction of the layer stack.

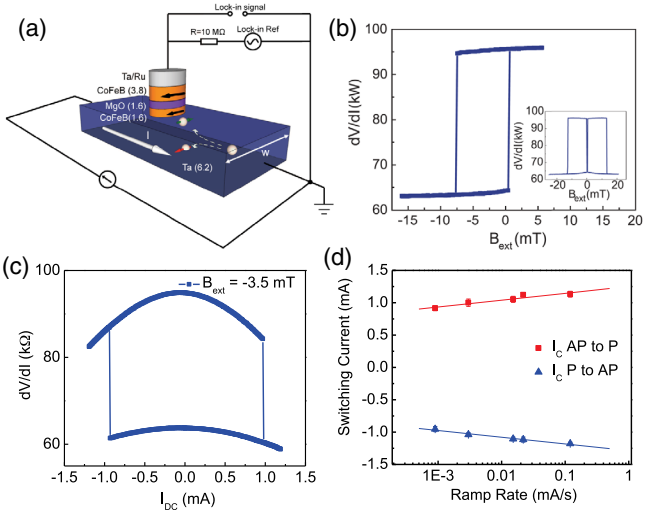

FIG. 40 (color online). SHE-induced switching for an in-plane magnetized nanomagnet at room temperature. (a) Schematic of the three-terminal SHE devices and the circuit for measurements. (b) TMR minor loop of the magnetic tunnel junction as a function of the external applied field B_{ext} applied in-plane along the long axis of the sample. Inset: TMR major loop of the device. (c) TMR of the device as a function of applied dc current I_{dc}. An in-plane external field of -3.5 mT is applied to set the device at the center of the minor loop. (d) Switching currents as a function of the ramp rate for sweeping current. Squares indicate switching from antiparallel (AP) to parallel (P) magnetizations; triangles indicate switching from P to AP. Solid lines represent linear fits of switching current versus log (ramp rate). Error bars are smaller than the symbol size. From Liu, Pai, Li *et al.*, 2012.

However, detailed analysis in later three-dimensional vector measurement (Garello *et al.*, 2013) point toward significant contributions from the SHE.

The results of these experiments may be viewed as a paradigm change in the mechanism for switching magnetic nanoelements in spintronic devices since here switching is driven by a purely in-plane electrical current and not via a current perpendicular to the layer stack. Similar results have been obtained for W/CoFeB layers (Pai *et al.*, 2012). One should note that, while the exact value for the spin Hall angle extracted from these experiments is still under debate, the fact that switching can be achieved for these devices underpins not only the technological relevance, but also that a sizeable SHE (possibly in combination with other ISGE-related SOTs) must be generated in these structures.

Similarly, the interpretation of the results of current-driven domain-wall motion experiments in the same type of layer stacks has to be revisited (Miron *et al.*, 2011). Current and even field-induced domain-wall motion experiments in layer stacks where ISGE, SHE, and proximity polarization of the NM can contribute are complicated for interpretation, and disentangling the relative strength of these contributions is not straightforward. Experimentally, however, it has been observed that the inclusion of relativistic torques, of either the SHE or ISGE origin, leads to a large increase of domain-wall velocities for optimally tuned materials which is potentially of technological interest (Emori *et al.*, 2013; Ryu *et al.*, 2013).

Spin-orbit coupling together with broken inversion symmetry introduces yet another important aspect into the physics of these systems. To fully understand the underlying mechanisms in these experiments one needs to take into account also the fact that these domain walls are chiral due to the Dzyaloshinski-Moriya interaction present at the FM-NM interface. This opens a new field connecting spintronics with the skyrmion physics.

We conclude by discussing in more detail that in the NM-FM bilayer systems the relativistic torques inducing magnetization dynamics are, in general, not only due to the SHE but the ISGE-induced SOTs may also contribute (Chernyshov *et al.*, 2009; Manchon and Zhang, 2009; Miron *et al.*, 2010; Fang *et al.*, 2011). The ISGE originate from spin-orbit coupling which, combined with broken inversion symmetry in the crystal, can produce spin polarization when electrical current is driven through a NM. In combination with FMs, the ISGE and the SHE can drive magnetization dynamics in devices with similar geometries. Disentangling these contributions in NM-FM bilayer systems and engineering them for maximal effect is at present a highly active field in spintronics.

However, the discrimination of the SHE and ISGE-based microscopic mechanisms between the field-like and the anti-damping-like torque components is difficult to achieve for several conceptual reasons. The original theoretical proposals (Aronov and Lyanda-Geller, 1989; Edelstein, 1990; Malâshukov and Chao, 2002) and experimental observations (Ganichev *et al.*, 2004; Kato *et al.*, 2004b; Silov *et al.*, 2004; Wunderlich *et al.*, 2004, 2005) of the ISGE were made in NMs with no FM component in the structure. The corresponding nonequilibrium spin density, generated in the ISGE by inversion-asymmetry terms in the relativistic Hamiltonian, has naturally no dependence on magnetization. Hence, in the context of magnetic semiconductors (Bernevig and Vafek, 2005; Chernyshov *et al.*, 2009; Endo, Matsukura, and Ohno, 2010; Fang *et al.*, 2011) or FM-NM structures (Manchon *et al.*, 2008; Miron *et al.*, 2010; Pi *et al.*, 2010; Miron, Garello *et al.*, 2011; Suzuki *et al.*, 2011), the ISGE may be expected to yield only the field-like component of the torque $\sim \mathbf{M} \times \boldsymbol{\zeta}$, where the vector $\boldsymbol{\zeta}$ is independent of the magnetization vector $\mathbf{M}$. However, when carriers experience both the spin-orbit coupling and magnetic exchange coupling, the inversion asymmetry can generate a nonequilibrium spin-density component of extrinsic, scattering-related (Pesin and MacDonald, 2012; Wang and Manchon, 2012) or intrinsic, Berry-curvature (Garate and MacDonald, 2009; Freimuth, Blügel, and Mokrousov, 2014; Kurebayashi *et al.*, 2014) origin which is magnetization dependent and yields an anti-damping-like torque $\sim \mathbf{M} \times (\mathbf{M} \times \boldsymbol{\zeta})$. Experiments in (Ga,Mn)As confirmed the presence of the ISGE-based mechanism (Chernyshov *et al.*, 2009; Endo, Matsukura, and Ohno, 2010; Fang *et al.*, 2011) and demonstrated that the field-like and the Berry-curvature anti-damping-like SOT components can have comparable magnitudes (Kurebayashi *et al.*, 2014).

The STT is dominated by the anti-damping-like component (Ralph and Stiles, 2008) in weakly spin-orbit-coupled FMs with $\tau_{\text{ex}} \ll \tau_s$, where τ_{ex} is the precession time of the carrier spins in the exchange field of the FM and τ_s is the spin lifetime in the FM. This, in principle, applies also to the case when the spin current is injected to the FM from a NM via the SHE.

TABLE III. Experimental spin Hall angles and related parameters. SP = spin pumping, NL = nonlocal, STT + SHE = spin transfer torque combined with spin Hall effect, LSA = local spin accumulation, MR = magnetic resonance, KRM = Kerr rotation microscopy. Values marked with * are not measured but taken from the literature.

	T (K)	λ_{sd} (nm)	σ_{NM} (10^6 S/m)	α_{SH} (%)	Comment	Reference
Al	4.2	455 ± 15	10.5	0.032 ± 0.006	NL (12-nm-thick films)	Valenzuela and Tinkham (2006, 2007)
	4.2	705 ± 30	17	0.016 ± 0.004	NL (25-nm-thick films)	Valenzuela and Tinkham (2006, 2007)
Au	295	86 ± 10	37	11.3	NL (10-nm-thick films)	Seki *et al.* (2008, 2010)
	295	83	37	3	NL (20-nm-thick films)	Seki *et al.* (2010)
	4.5	65*	48.3	<2.3	NL (SHE-ISHE)	Mihajlovic *et al.* (2009)
	295	36*	25.7	<2.7	NL (SHE-ISHE)	Mihajlovic *et al.* (2009)
	295	35 ± 4	28	7.0 ± 0.1	NL	Sugai, Mitani, and Takanashi (2010)
	295	27 ± 3	14	7.0 ± 0.3	NL (0.95 at. % Fe)	Sugai, Mitani, and Takanashi (2010)
	295	25 ± 3	14.5	12 ± 4	NL (1.4 at. % Pt, 10-nm-thick films)	Gu *et al.* (2010)
	295	50 ± 8	16.7	0.8 ± 0.2	NL (1.4 at. % Pt, 20-nm-thick films)	Gu *et al.* (2010)
	<10	40 ± 16	25	1.4 ± 0.4	NL	Niimi *et al.* (2014)
	295	35 ± 3*	25.2	0.35 ± 0.03	SP	Mosendz, Pearson *et al.* (2010)
	295	35	20	0.25 ± 0.1	SP	Vlaminck *et al.* (2013)
	295	35 ± 3*	5.25	1.6 ± 0.1	SP	Hung *et al.* (2013)
	295	35 ± 3*	7	0.335 ± 0.006	SP	Hung *et al.* (2013)
	295	35*		1.1 ± 0.3	SP	Obstbaum *et al.* (2014)
	295	60	20.4	8.4 ± 0.7	SP	Wang, Pauyac, and Manchon (2014)
AuW	295	1.9	1.75	>10	NL and SP (7 at. % W concentration in Au host, 10 K)	Laczkowski *et al.* (2014)
Ag	295	700	15	0.7 ± 0.1	SP	Wang, Pauyac, and Manchon (2014)
Bi	3	0.3 ± 0.1	-	>0.3	Local, signal decreases with ρ_N	Fan and Eom (2008)
	295	-	2.4 ± 0.3(I) 50 ± 12(V)	$-(7.1 \pm 0.8)$(I) 1.9 ± 0.2(V)	SP as a function of Bi thickness Volume (V) and interfacial (I) parameter	Hou *et al.* (2012)
Cu	295	500	16	0.32 ± 0.03	SP	Wang, Pauyac, and Manchon (2014)
CuIr	10	5–30		2.1 ± 0.6	NL (Ir concentrations from 0% to 12%)	Niimi *et al.* (2011)
$CuMn_xT_y$				0.7(Ta); 2.6(Ir) 1.35(Au); 1.15(Sb) −1.2(Lu)	T = Lu, Ta, Ir, Au, Sb [$y \sim (1\text{–}20) \times 10^{-4}$] Mn [$x \sim (1\text{–}2) \times 10^{-4}$] creates I_s Note a factor of 2 in the definition of α_{SH}^{skew}	Fert, Friederich, and Hamzic (1981) Ref. [15] in Fert and Levy (2011)
CuBi	10	~100; ~30 ~10; ~7		−11	NL (Bi = 0.3%; 0.5%), $\alpha_{SH}^{skew} = -(24 \pm 9)$ on Bi Similar in AgBi (Niimi *et al.*, 2014)	Niimi *et al.* (2012)
n-GaAs	4.2	2200	0.0056	0.15	NL, $n \approx 10^{17}$ cm^{-3}	Olejník *et al.* (2012)
	4.2	8500	0.00137	0.08	LSA, $n \approx 10^{16}$ cm^{-3}	Ehlert *et al.* (2012)
	30		0.0036	0.08	LSA, $n \approx 3\text{–}5 \times 10^{16}$ cm^{-3}	Garlid *et al.* (2010)
	2			≈ -0.001	MR, α_{SH} T-dependent, sign change at ≈ 10 K	Chazalviel (1975)
	295		0.027	0.00044; 0.001	SP, not annealed and annealed values; *n*-type	Rojas-Sánchez *et al.* (2013a)
n-InGaAs	30	~3000	~0.002	≈ 0.02	KRM, $x = 0.07$, $n \approx 3 \times 10^{16}$ cm^{-3}	Kato *et al.* (2004a)
(Si doped)	30		0.003–0.005	≈ 0.1; ≈ 0.25; ≈ 0.38	LSA, $x = 0.03, 0.05, 0.06$, $n \approx (3\text{–}5) \times 10^{16}$ cm^{-3}	Garlid *et al.* (2010)
InSb	1.3			-0.026 ± 0.005	MR, $n \approx 10^{14}$ cm^{-3}, $\mu \approx 2.2 \times 10^4$ cm^2/Vs	Chazalviel and Solomon (1972)
	1.3			0.003	MR $n \approx 10^{14}$ cm^{-3}, $\mu \approx 4 \times 10^4$ cm^2/Vs	Chazalviel and Solomon (1972)
IrO_2	300	3.8(P)	0.5(P); 0.18(A)	4(P); 6.5(A)	NL, polycrystalline (P), amorphous (A)	Fujiwara *et al.* (2013)

(Table continued)

TABLE III. (*Continued*)

	T (K)	λ_{sd} (nm)	σ_{NM} (10^6 S/m)	α_{SH} (%)	Comment	Reference
Mo	10	10	3.03	−0.20	NL	Morota *et al.* (2009)
	10	10	0.667	−0.075	NL	Morota *et al.* (2009)
	10	8.6 ± 1.3	2.8	$-(0.8 \pm 0.18)$	NL	Morota *et al.* (2011)
	295	$35 \pm 3^*$	4.66	$-(0.05 \pm 0.01)$	SP	Mosendz, Pearson *et al.* (2010)
Nb	10	5.9 ± 0.3	1.1	$-(0.87 \pm 0.20)$	NL	Morota *et al.* (2011)
Pd	10	13 ± 2	2.2	1.2 ± 0.4	NL	Morota *et al.* (2011)
	295	9^*	1.97	1.0	SP	Ando *et al.* (2010)
	295	$15 \pm 4^*$	4.0	0.64 ± 0.10	SP	Mosendz, Pearson *et al.* (2010)
	295	5.5 ± 0.5	5	1.2 ± 0.3	SP	Vlaminck *et al.* (2013)
	295	2.0 ± 0.1	3.7	0.8 ± 0.20	STT + SHE	Kondou *et al.* (2012)
Pt	295		6.41	0.37	NL	Kimura *et al.* (2007)
	5	8	8.0	0.44	NL ($\lambda_N = 14$ nm from spin absorption)	Vila, Kimura, and Otani (2007)
	295	7	5.56	0.9	NL ($\lambda_N = 10$ nm from spin absorption)	Vila, Kimura, and Otani (2007)
	10	11 ± 2	8.1	2.1 ± 0.5	NL	Morota *et al.* (2011)
	10	∼10	8.1	2.4	NL [3D corrected (Morota *et al.*, 2011)]	Niimi *et al.* (2012)
	295	7^*	6.4	8.0	SP	Ando *et al.* (2008)
	295	$10 \pm 2^*$	2.4	1.3 ± 0.2	SP	Mosendz, Pearson *et al.* (2010)
	295	10^*	2	4.0	SP	Ando, Takahashi, Ieda, Kajiwara (2011)
	295	3.7 ± 0.2	2.42	8 ± 1	SP	Azevedo *et al.* (2011)
	295	8.3 ± 0.9	4.3 ± 0.2	1.2 ± 0.2	SP	Feng *et al.* (2012)
	295	7.7 ± 0.7	1.3 ± 0.1	1.3 ± 0.1	SP	Nakayama *et al.* (2012)
	295	$1.5 - 10^*$	2.45 ± 0.1	$3^{+4}_{-1.5}$	SP, spin Hall magnetoresistance	Hahn *et al.* (2013)
	295	4	4	2.7 ± 0.5	SP	Vlaminck *et al.* (2013)
	295	$8 \pm 1^*$	1.02	2.012 ± 0.003	SP	Hung *et al.* (2013)
	295	1.3^*	2.4	2.1 ± 1.5	SP	Bai *et al.* (2013)
	295	1.2		8.6 ± 0.5	SP	Zhang *et al.* (2013)
	295	1.4^*		12 ± 4	SP	Obstbaum *et al.* (2014)
	295	3.4 ± 0.4	6.0	5.6 ± 0.1	SP	Rojas-Sánchez *et al.* (2014)
	295	7.3	2.1	10 ± 1	SP	Wang, Pauyac, and Manchon (2014)
	295	1.2 ± 0.1	3.6	2.2 ± 0.4	STT + SHE	Kondou *et al.* (2012)
	295	3(<6)	5.0	$7.6^{+8.4}_{-2.0}$	STT + SHE	Liu *et al.* (2011)
	295	2.1 ± 0.2	3.6	2.2 ± 0.8	STT + SHE	Ganguly *et al.* (2014)
	295	2.1 ± 0.2	3.6	8.5 ± 0.9	STT + SHE, modulation of damping	Ganguly *et al.* (2014)
	295	2.4^*	1.2	∼4	Spin Hall magnetoresistance	Nakayama *et al.* (2013)
	295	1.5 ± 0.5	0.5–3	11 ± 8	Spin Hall magnetoresistance (variable Pt thickness)	Althammer *et al.* (2013)
p-Si	295			≈ 0.01	SP, $\tau_s \sim 10$ ps $n \approx 2 \times 10^{19}$ cm^{-3}	Ando and Saitoh (2012)
Ta	10	2.7 ± 0.4	0.3	$-(0.37 \pm 0.11)$	NL	Morota *et al.* (2011)
	295	1.9	0.34	-7.1 ± 0.6	SP	Wang, Pauyac, and Manchon (2014)
	295	1.8 ± 0.7	0.08–0.75	$-(2^{+0.8}_{-1.5})$	SP, spin Hall magnetoresistance (variable Ta thickness)	Hahn *et al.* (2013)
	295		0.53	$-(12 \pm 4)$	STT + SHE (β-Ta)	Liu *et al.* (2012a)
	295	1.5 ± 0.5	0.5	$-(3 \pm 1)$	SP (β-Ta)	Gómez *et al.* (2014)
W	295	2.1	0.55	-14 ± 1	SP	Wang, Pauyac, and Manchon (2014)
	295		0.38 ± 0.06	$-(33 \pm 6)$	STT + SHE (β-W, lower in α-W α_{SH})	Pai *et al.* (2012)

However, at finite τ_s, the STT also acquires a field-like component (Ralph and Stiles, 2008). Experiments in W/Hf/CoFeB structures confirmed the presence of the SHE-based mechanism in the observed torques and showed that the SHE-STT can have both anti-damping-like and field-like components of comparable magnitudes (Pai *et al.*, 2014).

In the commonly studied polycrystalline transition-metal-FM-NM samples, the dependence of the torques on the angle of the driving in-plane current also does not provide the direct means to disentangle the two microscopic origins. The lowest order inversion-asymmetry spin-orbit terms in the Hamiltonian have the Rashba form for which the vector $\boldsymbol{\zeta}$ is in the plane parallel to the interface and perpendicular to the current, independent of the current direction. The same applies to the spin polarization of the SHE spin current propagating from the NM to the FM. The $\mathbf{M}$ and $\boldsymbol{\zeta}$ functional form of the field-like and anti-damping-like SHE-STTs is the same as of the corresponding ISGE-SOT components. In the observed lowest order torque terms in Pt/Co and Ta/CoFeB structures (Garello *et al.*, 2013) the ISGE-based and the SHE-based mechanism remained, therefore, indistinguishable. The simultaneous observation of higher order torque terms in these samples pointed to SOTs due to structural inversion-asymmetry terms beyond the basic Rashba model. From the Ta thickness dependence measurements in the Ta/CoFeB structure it was concluded that in these samples both the ISGE-based and the SHE-based mechanisms contributed to both the field-like and the anti-damping-like torques (Kim *et al.*, 2013). In another experiment, the effective spin-orbit field was found to be diminished with increasing the ferromagnetic layer thickness and to persist even with the insertion of a copper spacer (Fan *et al.*, 2013), suggesting that the spin torque does not rely in the studied structure on the heavy-NM-FM interface.

To separate the two model microscopic origins, experiments were performed in epitaxial Fe/(Ga,Mn)As bilayers (Skinner *et al.*, 2015). The structures allowed one to simultaneously observe ISGE-based and SHE-based torques of comparable amplitudes. Designed magnetization-angle and current-angle symmetries of the Fe/(Ga,Mn)As single-crystal structure with Dresselhaus-like inversion asymmetry allowed one to split the two microscopic origins between the ISGE dominated field-like torque and the SHE dominated anti-damping-like torque.

E. Spin Hall angles

In this section, we present in Table III experimental measurements of the SHE in different materials. The list, in such an active and evolving field, is by no means exhaustive. As discussed in this experimental section, as more things are learned about the techniques and systematic errors are better understood and corrected, the measurements begin to converge for several materials, particularly for the transition metals.

In Table III we show the material, the temperature the measurement was taken at, the spin-diffusion length either measured or used in the analysis, the conductivity, the spin Hall angle, the reference of the work, and the type of technique as well as relevant comments.

V. FUTURE DIRECTIONS AND REMAINING CHALLENGES

We conclude this review with our personal view of possible interesting directions and remaining challenges. As such, reflects our own preference and intuition. We apologize for any omissions of the many interesting possibilities that others may consider. We only know for certain that such future outlook is bound to always fail in a field that continues to bring surprises.

Transition metals have traditionally played a dominant role in spintronics both in basic research and, in particular, in applications. It is therefore not surprising that the SHE field has gained new momentum when bringing nonmagnetic transition metals in the game. And they have played their role particularly well. When brought out of equilibrium by an applied electric field, the SHE (or ISGE) in some nonmagnetic transition metals can generate sufficient flux of spin angular momentum to reorient magnetization in an adjacent transition metal FM. Entirely new concepts for writing information in magnetic tunnel junctions or domain-wall based spintronic devices have emerged from this discovered large strength of the SHE in this common, and technologically relevant, family of materials.

Ta, W, Ir, and Pt are examples among the nonmagnetic transition metals with large SHE. The strength of the effect is derived from the large spin-orbit coupling in these heavy elements. Apart from the new opportunities for applications, this brings also new challenges for the basic research of the SHE in transition metals. We have mentioned in the review the pitfalls in attempting to microscopically describe the SHE in structures comprising heavy transition metals from theories of spin transport in weakly spin-orbit-coupled systems. The proper description and microscopic understanding of the SHE structures in the strong spin-orbit coupling regime is among the key remaining challenges in the SHE field.

The flurry of recent SHE studies in transition metals may give an impression that the field is forgetting its semiconductor roots. Robust FMs are typically dense-moment systems and their switching requires comparably large electrical current densities generating the SHE spin current. Highly conductive transition metals are clearly favorable from this perspective when compared to semiconductors. Moreover, the reported spin Hall angles in semiconductors do not reach the record values in transition metals.

We nevertheless foresee semiconductors playing a vital role in future SHE research, in particular, when considering spintronics concepts without FMs. In the transition metal context, the SHE is used as an efficient spin-current generator or detector but these studies rarely consider spin manipulation in the nonmagnetic SHE system. Especially in the strongly spin-orbit-coupled heavy metals, the spin-diffusion length is of the order of nanometers, too short for implementing any spin manipulation tools along the nonmagnetic transport channel. For semiconductors, on the other hand, we have mentioned in the review several examples of electrical manipulation of the output SHE signal. A gate electrode can be used to control coherent spin precession along the channel, additional drift current was shown to modify the spin-current profile along the channel, and nonlinear

intervalley transport can strongly enhance the spin Hall angles bringing the values close to their heavy metal counterparts.

The physics is, however, no different in principle between metals and semiconductors. Large SHE requires large spin-orbit coupling which, on the other hand, tends to suppress spin coherence or diffusion length. Semiconductors with their simpler electronic structure and model spin-orbit fields offer unique ways how to get around this problem. As demonstrated, a proper tuning of the Rashba and Dresselhaus spin-orbit fields can significantly enhance spin coherence in the presence of strong spin-orbit coupling. Experiments outside the SHE field have recently made major progress in controlling these two canonical spin-orbit fields in common semiconductor structures and we envisage new developments in semiconductor SHE devices utilizing the coherent spin-manipulation techniques.

Combining optical selection rules with SHE makes semiconductors also favorable materials for exploring new concepts in optospintronics. These may include optical spin-torque structures, electrical polarimeters, spin-photovoltaic cells, switches, invertors, and interconnects. The optospintronic subfield of the SHE research is still at its infancy and we expect growing activity in this direction in the future.

The fascinating feature of the SHE is that it can generate a large spin current, and a resulting large spin accumulation by bringing weakly out of equilibrium a nonmagnetic system. It is, therefore, natural that nonmagnetic materials have been traditionally at the center of the SHE research. However, limiting ourselves to paramagnetic or diamagnetic materials, whether metallic or semiconducting, is not necessary when considering the spin Hall phenomena. Recently, several transition-metal FMs and antiferromagnets were demonstrated to act as efficient ISHE spin-current detectors, which opens a new broad area of future materials research in the SHE.

It also brings us back to the opening paragraphs of this section, where we mentioned SHE-induced spin torques in NM-FM heterostructures. Since in strongly spin-orbit-coupled systems these torques are limited to a few atomic layers around the NM-FM interface, and considering the likely material intermixing at the interface, it is not meaningful to speak strictly about a nonmagnetic layer SHE in these structures. The difference then becomes blurred whether including magnetism via intermixing or proximity polarization at heterointerfaces, or directly considering the SHE in bulk FM or antiferromagnetic materials. Within this notion, an important challenge arises not only for the normal-metal–magnet interfaces but also for monolayer magnets to identify the microscopic origin of the observed spin torques. It remains an open question whether the current-induced torques in the magnet are better linked to a SHE-induced spin-current origin or to one of the variants of the ISGE-induced nonequilibrium spin polarization. Resolving these contributions is an important academic exercise with potentially large implications for the utility of these spin-orbit-coupling phenomena in spintronic information technologies.

We conclude by emphasizing that the field of SHE does not live in a vacuum. Its interconnections to other emerging fields, e.g., graphene and other 2D systems, topological insulators, and spin caloritronics, make its growth and possibilities very difficult to predict. Many things that we have discussed here and that have emerged from its link to these fields were not known or expected a few years ago. It is a rapidly evolving field that produces discoveries at a neck-breaking speed and we all look forward to its exciting future.

LIST OF SYMBOLS AND ABBREVIATIONS

2DEG	Two-dimensional electron gas
2DHG	Two-dimensional hole gas
ac	Alternating current
AHE	Anomalous Hall effect
AMR	Anistropic magnetoresistance
CPW	Coplanar wave guide
dc	Direct current
FM	Ferromagnet
FMR	Ferromagnetic resonance
HE	Hall effect
ISGE	Inverse spin galvanic effect
MOD	Modulation of damping
MRAM	Magnetic random access memory
NM	Nonmagnetic material
QHE	Quantum Hall effect
QSHE	Quantum spin Hall effect
rf	Radio frequency
SGE	Spin galvanic effect
SHE	Spin Hall effect
SOT	Spin-orbit torque
SP	Spin pumping
STT	Spin-transfer torque
TMR	Tunneling magnetoresistance

ACKNOWLEDGMENTS

We thank all colleagues who have given us the permission to show their results in this review. We also thank all our colleagues within the spintronics community that engaged us in many fruitful interactions and spirited discussions. J. S. acknowledges partial support by the Alexander von Humboldt Foundation, the European Research Council (ERC) Synergy Grant No. 610115, and the German Research Foundation (DFG) through Program No. SPP 1538. S. O. V. acknowledges partial support from the European Research Council under Grant Agreement No. 308023 SPINBOUND and from the Spanish Ministry of Economy and Competitiveness (MINECO) under Contract No. MAT2013-46785-P and Severo Ochoa Program No. SEV-2013-0295. J. W. acknowledges partial support from the European Metrology Research Programme Joint Research Project (EMRP JRP) IND08 MetMags and the ERC Synergy Grant No. 610115. C. B. acknowledges partial support from the DFG through Programs No. SFB 689 and No. SPP 1538 and from the European Research Council (ERC) through starting Grant No. 280048 ECOMAGICS. T. J. acknowledges partial support from the ERC Advanced Grant No. 268066; the Ministry of Education of the Czech Republic, Grant No. LM2011026; the Grant Agency of the Czech Republic, Grant No. 14-37427G.

REFERENCES

Abanin, D. A., R. V. Gorbachev, K. S. Novoselov, A. K. Geim, and L. S. Levitov, 2011, Phys. Rev. Lett. **107**, 096601.

Adagideli, I., and G. E. W. Bauer, 2005, Phys. Rev. Lett. **95**, 256602.

Adagideli, I., G. E. W. Bauer, and B. I. Halperin, 2006, Phys. Rev. Lett. **97**, 256601.

Althammer, M., *et al.*, 2013, Phys. Rev. B **87**, 224401.

Ando, K., J. Ieda, K. Sasage, S. Takahashi, S. Maekawa, and E. Saitoh, 2009, Appl. Phys. Lett. **94**, 262505.

Ando, K., M. Morikawa, T. Trypiniotis, Y. Fujikawa, C. H. W. Barnes, and E. Saitoh, 2010, Appl. Phys. Lett. **96**, 082502.

Ando, K., and E. Saitoh, 2010, J. Appl. Phys. **108**, 113925.

Ando, K., and E. Saitoh, 2012, Phys. Rev. Lett. **109**, 026602.

Ando, K., S. Takahashi, K. Harii, K. Sasage, J. Ieda, S. Maekawa, and E. Saitoh, 2008, Phys. Rev. Lett. **101**, 036601.

Ando, K., S. Takahashi, J. Ieda, H. Kurebayashi, T. Trypiniotis, C. H. W. Barnes, S. Maekawa, and E. Saitoh, 2011, Nat. Mater. **10**, 655.

Ando, K., *et al.*, 2011, J. Appl. Phys. **109**, 103913.

Aronov, A. G., and Y. B. Lyanda-Geller, 1989, JETP Lett. **50**, 431 [http://www.jetpletters.ac.ru/ps/1132/article_17140.pdf].

Avsar, A., *et al.*, 2014, Nat. Commun. **5**, 4875.

Azevedo, A., O. Alves Santos, G. A. Fonseca Guerra, R. O. Cunha, R. Rodríguez-Suárez, and S. M. Rezende, 2014, Appl. Phys. Lett. **104**, 052402.

Azevedo, A., L. H. Vilela Leão, R. L. Rodriguez-Suarez, A. B. Oliveira, and S. M. Rezende, 2005, J. Appl. Phys. **97**, 10C715.

Azevedo, A., L. H. Vilela-Leão, R. L. Rodríguez-Suárez, A. F. Lacerda Santos, and S. M. Rezende, 2011, Phys. Rev. B **83**, 144402.

Bader, S. D., and S. Parkin, 2010, Annu. Rev. Condens. Matter Phys. **1**, 71.

Bai, L., P. Hyde, Y. S. Gui, C.-M. Hu, V. Vlaminck, J. E. Pearson, S. D. Bader, and A. Hoffmann, 2013, Phys. Rev. Lett. **111**, 217602.

Bakun, A., B. Zakharchenya, A. Rogachev, M. Tkachuk, and V. Fleisher, 1984, Pis'ma Zh. Eksp. Teor. Fiz. **40**, 464 [http://www.jetpletters.ac.ru/ps/1262/article_19087.pdf].

Balakrishnan, J., G. Kok Wai Koon, M. Jaiswal, A. H. Castro Neto, and B. Özyilmaz, 2013, Nat. Phys. **9**, 284.

Balakrishnan, J., *et al.*, 2014, Nat. Commun. **5**, 4748.

Bauer, G. E. W., A. H. MacDonald, and S. Maekawa, 2010, Solid State Commun. **150**, 459.

Bauer, G. E. W., E. Saitoh, and B. J. van Wees, 2012, Nat. Mater. **11**, 391.

Belkov, V. V., and S. D. Ganichev, 2008, Semicond. Sci. Technol. **23**, 114003.

Berger, L., 1964, Physica (Utrecht) **30**, 1141.

Berger, L., 1970, Phys. Rev. B **2**, 4559.

Bernevig, B. A., T. L. Hughes, and S.-C. Zhang, 2006, Science **314**, 1757.

Bernevig, B. A., and O. Vafek, 2005, Phys. Rev. B **72**, 033203.

Brouwer, P. W., 1998, Phys. Rev. B **58**, R10135.

Brüne, C., A. Roth, E. G. Novik, M. König, H. Buhmann, E. M. Hankiewicz, W. Hanke, J. Sinova, and L. W. Molenkamp, 2010, Nat. Phys. **6**, 448.

Büttiker, M., 2009, Science **325**, 278.

Büttiker, M., H. Thomas, and A. Prêtre, 1993, Phys. Rev. Lett. **70**, 4114.

Carva, K., and I. Turek, 2007, Phys. Rev. B **76**, 104409.

Castro Neto, A. H., and F. Guinea, 2009, Phys. Rev. Lett. **103**, 026804.

Chang, H., T. Chen, J. Chen, W. Hong, W. Tsai, Y. Chen, and G. Guo, 2007, Phys. Rev. Lett. **98**, 136403.

Chazalviel, J. N., 1975, Phys. Rev. B **11**, 3918.

Chazalviel, J. N., and I. Solomon, 1972, Phys. Rev. Lett. **29**, 1676.

Chen, L., F. Matsukura, and H. Ohno, 2013, Nat. Commun. **4**, 2055.

Chernyshov, A., M. Overby, X. Liu, J. K. Furdyna, Y. Lyanda-Geller, and L. P. Rokhinson, 2009, Nat. Phys. **5**, 656.

Chudnovsky, E., 2007, Phys. Rev. Lett. **99**, 206601.

Chudnovsky, E., 2009, Phys. Rev. B **80**, 153105.

Ciccarelli, C., K. M. D. Hals, A. Irvine, V. Novak, Y. Tserkovnyak, H. Kurebayashi, A. Brataas, and A. Ferguson, 2014, Nat. Nanotechnol. **10**, 50.

Costache, M. V., M. Sladkov, C. H. van der Wal, and B. J. van Wees, 2006, Appl. Phys. Lett. **89**, 192506.

Costache, M. V., M. Sladkov, S. Watts, C. van der Wal, and B. van Wees, 2006, Phys. Rev. Lett. **97**, 216603.

Costache, M. V., S. M. Watts, M. Sladkov, C. H. van der Wal, and B. J. van Wees, 2006, Appl. Phys. Lett. **89**, 232115.

Crépieux, A., and P. Bruno, 2001, Phys. Rev. B **64**, 014416.

Culcer, D., 2009, in *Encyclopedia of Complexity and Systems Science*, edited by R. A. Meyer (Springer, New York).

Culcer, D., J. Sinova, N. A. Sinitsyn, T. Jungwirth, A. H. MacDonald, and Q. Niu, 2004, Phys. Rev. Lett. **93**, 046602.

Czaja, P., F. Freimuth, J. Weischenberg, S. Blügel, and Y. Mokrousov, 2014, Phys. Rev. B **89**, 014411.

Czeschka, F. D., *et al.*, 2011, Phys. Rev. Lett. **107**, 046601.

Day, C., 2005, Phys. Today **58**, No. 2, 17.

Demidov, V. E., S. Urazhdin, E. R. J. Edwards, and S. O. Demokritov, 2011a, Appl. Phys. Lett. **99**, 172501.

Demidov, V. E., S. Urazhdin, E. R. J. Edwards, M. D. Stiles, R. D. McMichael, and S. O. Demokritov, 2011b, Phys. Rev. Lett. **107**, 107204.

Demidov, V. E., S. Urazhdin, H. Ulrichs, V. Tiberkevich, A. Slavin, D. Baither, G. Schmitz, and S. O. Demokritov, 2012, Nat. Mater. **11**, 1028.

Dimitrova, O. V., 2005, Phys. Rev. B **71**, 245327.

Dirac, P. A. M., 1928, Proc. R. Soc. A **117**, 610.

Duan, Z., A. Smith, L. Yang, B. Youngblood, J. Lindner, V. E. Demidov, S. O. Demokritov, and I. N. Krivorotov, 2014, Nat. Commun. **5**, 5616.

Dugaev, V. K., M. Inglot, E. Y. Sherman, and J. Barnaś, 2010, Phys. Rev. B **82**, 121310.

Dyakonov, M., and A. G. Khaetskii, 2008, in *Spin Physics in Semiconductors* (Springer, New York), p. 211.

Dyakonov, M., and V. I. Perel, 1971a, Phys. Lett. **35A**, 459.

Dyakonov, M., and V. I. Perel, 1971b, Zh. Eksp. Teor. Fiz. **13**, 657.

Edelstein, V. M., 1990, Solid State Commun. **73**, 233.

Ehlert, M., C. Song, M. Ciorga, T. Hupfauer, J. Shiogai, M. Utz, D. Schuh, D. Bougeard, and D. Weiss, 2014, Phys. Status Solidi (b) **251**, 1725.

Ehlert, M., C. Song, M. Ciorga, M. Utz, D. Schuh, D. Bougeard, and D. Weiss, 2012, Phys. Rev. B **86**, 205204.

Emori, S., U. Bauer, S.-M. Ahn, E. Martinez, and G. S. D. Beach, 2013, Nat. Mater. **12**, 611.

Endo, M., F. Matsukura, and H. Ohno, 2010, Appl. Phys. Lett. **97**, 222501.

Engel, H.-A., B. Halperin, and E. Rashba, 2005, Phys. Rev. Lett. **95**, 166605.

Engel, H.-A., E. I. Rasbha, and B. I. Halperin, 2006, in *Handbook of Magnetism and Advanced Magnetic Materials*, edited by H. Kronmüller, and S. Parkin (John Wiley and Sons, New York), p. 2828.

Fan, J., and J. Eom, 2008, Appl. Phys. Lett. **92**, 142101.

Fan, X., J. Wu, Y. Chen, M. J. Jerry, H. Zhang, and J. Q. Xiao, 2013, Nat. Commun. **4**, 1799.

Fan, Y., *et al.*, 2014, Nat. Mater. **13**, 699.

Fang, D., H. Kurebayashi, J. Wunderlich, K. Výborný, L. P. Zârbo, R. P. Campion, A. Casiraghi, B. L. Gallagher, T. Jungwirth, and A. J. Ferguson, 2011, Nat. Nanotechnol. **6**, 413.
Feng, Z., *et al.*, 2012, Phys. Rev. B **85**, 214423.
Fert, A., A. Friederich, and A. Hamzic, 1981, J. Magn. Magn. Mater. **24**, 231.
Fert, A., and P. M. Levy, 2011, Phys. Rev. Lett. **106**, 157208.
Freimuth, F., S. Blügel, and Y. Mokrousov, 2010, Phys. Rev. Lett. **105**, 246602.
Freimuth, F., S. Blügel, and Y. Mokrousov, 2014, Phys. Rev. B **90**, 174423.
Fujiwara, K., Y. Fukuma, J. Matsuno, H. Idzuchi, Y. Niimi, Y. Otani, and H. Takagi, 2013, Nat. Commun. **4**, 2893.
Ganguly, A., K. Kondou, H. Sukegawa, S. Mitani, S. Kasai, Y. Niimi, Y. Otani, and A. Barman, 2014, Appl. Phys. Lett. **104**, 072405.
Ganichev, S. D., S. N. Danilov, P. Schneider, V. V. Bel'kov, L. E. Golub, W. Wegscheider, D. Weiss, and W. Prettl, 2004, cond-mat/0403641.
Ganichev, S. D., E. L. Ivchenko, V. V. Bel'kov, S. A. Tarasenko, M. Sollinger, D. Weiss, W. Wegscheider, and W. Prettl, 2002, Nature (London) **417**, 153.
Garate, I., and A. H. MacDonald, 2009, Phys. Rev. B **80**, 134403.
Garello, K., I. M. Miron, C. O. Avci, F. Freimuth, Y. Mokrousov, S. Blügel, S. Auffret, O. Boulle, G. Gaudin, and P. Gambardella, 2013, Nat. Nanotechnol. **8**, 587.
Garlid, E. S., Q. Hu, M. Chan, C. Palmstrom, and P. A. Crowell, 2010, Phys. Rev. Lett. **105**, 156602.
Gay, T. J., and F. B. Dunning, 1992, Rev. Sci. Instrum. **63**, 1635.
Gómez, J. E., B. Zerai Tedlla, N. R. Álvarez, G. Alejandro, E. Goovaerts, and A. Butera, 2014, Phys. Rev. B **90**, 184401.
Gradhand, M., D. V. Fedorov, F. Pientka, P. Zahn, I. Mertig, and B. L. Györffy, 2012, J. Phys. Condens. Matter **24**, 213202.
Gradhand, M., D. V. Fedorov, P. Zahn, and I. Mertig, 2010, Phys. Rev. B **81**, 245109.
Gu, B., I. Sugai, T. Ziman, G. Y. Guo, N. Nagaosa, T. Seki, K. Takanashi, and S. Maekawa, 2010, Phys. Rev. Lett. **105**, 216401.
Guo, G., S. Murakami, T.-W. Chen, and N. Nagaosa, 2008, Phys. Rev. Lett. **100**, 096401.
Guo, G. Y., 2009, J. Appl. Phys. **105**, 07C701.
Haazen, P. P. J., E. Murè, J. H. Franken, R. Lavrijsen, H. J. M. Swagten, and B. Koopmans, 2013, Nat. Mater. **12**, 299.
Hahn, C., G. de Loubens, O. Klein, M. Viret, V. V. Naletov, and J. Ben Youssef, 2013, Phys. Rev. B **87**, 174417.
Hall, E., 1881, Philos. Mag. **12**, 157.
Hamadeh, A., *et al.*, 2014, Phys. Rev. Lett. **113**, 197203.
Hankiewicz, E. M., L. W. Molenkamp, T. Jungwirth, and J. Sinova, 2004, Phys. Rev. B **70**, 241301.
Hankiewicz, E. M., and G. Vignale, 2009, J. Phys. Condens. Matter **21**, 253202.
Hasan, M. Z., and C. Kane, 2010, Rev. Mod. Phys. **82**, 3045.
Heinrich, B., Y. Tserkovnyak, G. Woltersdorf, A. Brataas, R. Urban, and G. E. W. Bauer, 2003, Phys. Rev. Lett. **90**, 187601.
Hirsch, J., 1999, Phys. Rev. Lett. **83**, 1834.
Hoffmann, A., 2013a, Physics **6**, 39.
Hoffmann, A., 2013b, IEEE Trans. Magn. **49**, 5172.
Hou, D., *et al.*, 2012, Appl. Phys. Lett. **101**, 042403.
Huang, B., D. J. Monsma, and I. Appelbaum, 2007, Appl. Phys. Lett. **91**, 072501.
Huang, S., X. Fan, D. Qu, Y. Chen, W. Wang, J. Wu, T. Chen, J. Xiao, and C. Chien, 2012, Phys. Rev. Lett. **109**, 107204.
Hung, H. Y., G. Y. Luo, Y. C. Chiu, P. Chang, W. C. Lee, J. G. Lin, S. F. Lee, M. Hong, and J. Kwo, 2013, J. Appl. Phys. **113**, 17C507.
Inoue, J.-I., G. E. W. Bauer, and L. Molenkamp, 2004, Phys. Rev. B **70**, 041303.
Inoue, J.-I., G. E. W. Bauer, and L. W. Molenkamp, 2003, Phys. Rev. B **67**, 033104.
Isasa, M., A. Bedoya-Pinto, S. Vélez, F. Golmar, F. Sánchez, L. E. Hueso, J. Fontcuberta, and F. Casanova, 2014, Appl. Phys. Lett. **105**, 142402.
Ivchenko, E. L., and S. D. Ganichev, 2008, in *Spin Physics in Semiconductors*, edited by M. Dyakonov (Springer, New York), p. 245.
Ivchenko, E. L., Y. B. Lyanda-Geller, and G. E. Pikus, 1989, JETP Lett. **50**, 175 [http://www.jetpletters.ac.ru/ps/1126/article_17072.pdf].
Ivchenko, E. L., and G. E. Pikus, 1978, JETP Lett. **27**, 604.
Jain, A., *et al.*, 2012, Phys. Rev. Lett. **109**, 106603.
Jaworski, C. M., J. Yang, S. Mack, D. D. Awschalom, J. P. Heremans, and S. Mährlein, 2010, Nat. Mater. **9**, 898.
Jiao, H., and G. E. W. Bauer, 2013, Phys. Rev. Lett. **110**, 217602.
Johnson, M., and R. H. Silsbee, 1985, Phys. Rev. Lett. **55**, 1790.
Johnson, M., and R. H. Silsbee, 1987, Phys. Rev. B **35**, 4959.
Jungwirth, T., Q. Niu, and A. H. MacDonald, 2002, Phys. Rev. Lett. **88**, 207208.
Jungwirth, T., J. Wunderlich, and K. Olejník, 2012, Nat. Mater. **11**, 382.
Kampfrath, T., *et al.*, 2013, Nat. Nanotechnol. **8**, 256.
Kane, C. L., and E. J. Mele, 2005, Phys. Rev. Lett. **95**, 146802.
Karplus, R., and J. M. Luttinger, 1954, Phys. Rev. **95**, 1154.
Kasai, S., K. Kondou, H. Sukegawa, S. Mitani, K. Tsukagoshi, and Y. Otani, 2014, Appl. Phys. Lett. **104**, 092408.
Kato, Y. K., R. C. Myers, A. C. Gossard, and D. D. Awschalom, 2004a, Science **306**, 1910.
Kato, Y. K., R. Myers, A. Gossard, and D. D. Awschalom, 2004b, Phys. Rev. Lett. **93**, 176601.
Kim, J., J. Sinha, M. Hayashi, M. Yamanouchi, S. Fukami, T. Suzuki, S. Mitani, and H. Ohno, 2013, Nat. Mater. **12**, 240.
Kimura, T., Y. Otani, T. Sato, S. Takahashi, and S. Maekawa, 2007, Phys. Rev. Lett. **98**, 156601.
Kondou, K., H. Sukegawa, S. Mitani, K. Tsukagoshi, and S. Kasai, 2012, Appl. Phys. Express **5**, 073002.
König, M., S. Wiedmann, C. Brüne, A. Roth, H. Buhmann, L. W. Molenkamp, X.-L. Qi, and S.-C. Zhang, 2007, Science **318**, 766.
Kontani, H., T. Tanaka, D. Hirashima, K. Yamada, and J. Inoue, 2009, Phys. Rev. Lett. **102**, 016601.
Kovalev, A., J. Sinova, and Y. Tserkovnyak, 2010, Phys. Rev. Lett. **105**, 036601.
Kravchenko, V., 2008, Phys. Rev. Lett. **100**, 199703.
Kurebayashi, H., *et al.*, 2014, Nat. Nanotechnol. **9**, 211.
Laczkowski, P., *et al.*, 2014, Appl. Phys. Lett. **104**, 142403.
Linder, J., and T. Yokoyama, 2011, Phys. Rev. Lett. **106**, 237201.
Liu, L., T. Moriyama, D. C. Ralph, and R. A. Buhrman, 2011, Phys. Rev. Lett. **106**, 036601.
Liu, L., C.-F. Pai, Y. Li, H. W. Tseng, D. C. Ralph, and R. A. Buhrman, 2012a, Science **336**, 555.
Liu, L., C.-F. Pai, D. C. Ralph, and R. A. Buhrman, 2012b, Phys. Rev. Lett. **109**, 186602.
Liu, R., W. Lim, and S. Urazhdin, 2013, Phys. Rev. Lett. **110**, 147601.
Long, N. H., P. Mavropoulos, B. Zimmermann, D. S. G. Bauer, S. Blügel, and Y. Mokrousov, 2014, Phys. Rev. B **90**, 064406.
Lou, X., C. Adelmann, S. A. Crooker, E. S. Garlid, J. Zhang, K. S. M. Reddy, S. D. Flexner, C. J. Palmstrøm, and P. A. Crowell, 2007, Nat. Phys. **3**, 197.
Lowitzer, S., M. Gradhand, D. Ködderitzsch, D. V. Fedorov, I. Mertig, and H. Ebert, 2011, Phys. Rev. Lett. **106**, 056601.

Lowitzer, S., D. Ködderitzsch, and H. Ebert, 2010, Phys. Rev. Lett. **105**, 266604.
Maekawa, S., and S. Takahashi, 2012, in *Spin Current*, edited by S. Maekawa, S. O. Valenzuela, E. Saitoh, and T. Kimura (Oxford University, New York), pp. 194–226.
Mahan, G. D., 2000, *Many-Particle Physics*, 3rd ed. (Plenum, New York).
Malâshukov, A. G., and K. A. Chao, 2002, Phys. Rev. B **65**, 241308.
Manchon, A., and S. Zhang, 2009, Phys. Rev. B **79**, 094422.
Manchon, A., *et al.*, 2008, J. Appl. Phys. **104**, 043914.
Matsuzaka, S., Y. Ohno, and H. Ohno, 2009, Phys. Rev. B **80**, 241305.
McGuire, T., and R. Potter, 1975, IEEE Trans. Magn. **11**, 1018.
Mecking, N., Y. Gui, and C.-M. Hu, 2007, Phys. Rev. B **76**, 224430.
Meier, F., and B. P. Zakharchenya, 1984, *Optical Orientation and Femtosecond Relaxation of Spin-Polarized Holes in GaAs* (North Holland, New York).
Mellnik, A. R., *et al.*, 2014, Nature (London) **511**, 449.
Mendes, J. B. S., R. O. Cunha, O. Alves Santos, P. R. T. Ribeiro, F. L. A. Machado, R. L. Rodríguez-Suárez, A. Azevedo, and S. M. Rezende, 2014, Phys. Rev. B **89**, 140406.
Miah, M. I., 2007, J. Phys. D **40**, 1659.
Miao, B. F., S. Y. Huang, D. Qu, and C. L. Chien, 2013, Phys. Rev. Lett. **111**, 066602.
Mihajlovic, G., J. E. Pearson, M. A. Garcia, S. D. Bader, and A. Hoffmann, 2009, Phys. Rev. Lett. **103**, 166601.
Miron, I. M., K. Garello, G. Gaudin, P.-J. Zermatten, M. V. Costache, S. Auffret, S. Bandiera, B. Rodmacq, A. Schuhl, and P. Gambardella, 2011, Nature (London) **476**, 189.
Miron, I. M., G. Gaudin, S. Auffret, B. Rodmacq, A. Schuhl, S. Pizzini, J. Vogel, and P. Gambardella, 2010, Nat. Mater. **9**, 230.
Miron, I. M., *et al.*, 2011, Nat. Mater. **10**, 419.
Mizukami, S., Y. Ando, and T. Miyazaki, 2001, J. Magn. Magn. Mater. **226–230**, 1640.
Mizukami, S., Y. Ando, and T. Miyazaki, 2002, Phys. Rev. B **66**, 104413.
Moore, J. E., 2010, Nature (London) **464**, 194.
Morota, M., Y. Niimi, K. Ohnishi, D. H. Wei, T. Tanaka, H. Kontani, T. Kimura, and Y. Otani, 2011, Phys. Rev. B **83**, 174405.
Morota, M., K. Ohnishi, T. Kimura, and Y. Otani, 2009, J. Appl. Phys. **105**, 07C712.
Mosendz, O., J. E. Pearson, F. Y. Fradin, G. E. W. Bauer, S. D. Bader, and A. Hoffmann, 2010, Phys. Rev. Lett. **104**, 046601.
Mosendz, O., V. Vlaminck, J. E. Pearson, F. Y. Fradin, G. E. W. Bauer, S. D. Bader, and A. Hoffmann, 2010, Phys. Rev. B **82**, 214403.
Mott, N. F., 1929, Proc. R. Soc. A **124**, 425.
Mott, N. F., 1932, Proc. R. Soc. A **135**, 429.
Murakami, S., 2006, Adv. Solid State Phys. **45**, 197.
Murakami, S., N. Nagaosa, and S.-C. Zhang, 2003, Science **301**, 1348.
Murakami, S., N. Nagaosa, and S.-C. Zhang, 2004, Phys. Rev. Lett. **93**, 156804.
Nagaosa, N., J. Sinova, S. Onoda, A. H. MacDonald, and N. P. Ong, 2010, Rev. Mod. Phys. **82**, 1539.
Nakayama, H., K. Ando, K. Harii, T. Yoshino, R. Takahashi, Y. Kajiwara, K. Uchida, Y. Fujikawa, and E. Saitoh, 2012, Phys. Rev. B **85**, 144408.
Nakayama, H., *et al.*, 2013, Phys. Rev. Lett. **110**, 206601.
Niimi, Y., Y. Kawanishi, D. H. Wei, C. Deranlot, H. X. Yang, M. Chshiev, T. Valet, A. Fert, and Y. Otani, 2012, Phys. Rev. Lett. **109**, 156602.
Niimi, Y., M. Morota, D. H. Wei, C. Deranlot, M. Basletic, A. Hamzic, A. Fert, and Y. Otani, 2011, Phys. Rev. Lett. **106**, 126601.
Niimi, Y., H. Suzuki, Y. Kawanishi, Y. Omori, T. Valet, A. Fert, and Y. Otani, 2014, Phys. Rev. B **89**, 054401.
Nomura, K., J. Wunderlich, J. Sinova, B. Kaestner, A. H. MacDonald, and T. Jungwirth, 2005, Phys. Rev. B **72**, 245330.
Nozieres, P., and C. Lewiner, 1973, J. Phys. (Paris) **34**, 901.
Obstbaum, M., M. Härtinger, H. G. Bauer, T. Meier, F. Swientek, C. H. Back, and G. Woltersdorf, 2014, Phys. Rev. B **89**, 060407.
Okamoto, N., H. Kurebayashi, T. Trypiniotis, I. Farrer, D. A. Ritchie, E. Saitoh, J. Sinova, J. Mašek, T. Jungwirth, and C. H. W. Barnes, 2014, Nat. Mater. **13**, 932.
Oki, S., K. Masaki, N. Hashimoto, S. Yamada, M. Miyata, M. Miyao, T. Kimura, and K. Hamaya, 2012, Phys. Rev. B **86**, 174412.
Olejník, K., J. Wunderlich, A. Irvine, R. P. Campion, V. P. Amin, J. Sinova, and T. Jungwirth, 2012, Phys. Rev. Lett. **109**, 076601.
Onoda, M., and N. Nagaosa, 2002, J. Phys. Soc. Jpn. **71**, 19.
Pai, C.-F., L. Liu, Y. Li, H. W. Tseng, D. C. Ralph, and R. A. Buhrman, 2012, Appl. Phys. Lett. **101**, 122404.
Pai, C.-F., M.-H. Nguyen, C. Belvin, L. H. Vilela-Leão, D. C. Ralph, and R. A. Buhrman, 2014, Appl. Phys. Lett. **104**, 082407.
Pesin, D. A., and A. H. MacDonald, 2012, Phys. Rev. B **86**, 014416.
Pi, U. H., K. Won Kim, J. Y. Bae, S. C. Lee, Y. J. Cho, K. S. Kim, and S. Seo, 2010, Appl. Phys. Lett. **97**, 162507.
Qian, X., J. Liu, L. Fu, and J. Li, 2014, Science **346**, 1344.
Raimondi, R., P. Schwab, C. Gorini, and G. Vignale, 2012, Ann. Phys. (Berlin) **524**, 153.
Ralph, D., and M. Stiles, 2008, J. Magn. Magn. Mater. **320**, 1190.
Rasbha, E. I., 2000, Phys. Rev. B **62**, R16267.
Rojas-Sánchez, J. C., L. Vila, G. Desfonds, S. Gambarelli, J.-P. Attane, J. M. De Teresa, C. Magén, and A. Fert, 2013, Nat. Commun. **4**, 2944.
Rojas-Sánchez, J.-C. , N. Reyren, P. Laczkowski, W. Savero, J.-P. Attane, C. Deranlot, M. Jamet, J.-M. George, L. Vila, and H. Jaffrès, 2014, Phys. Rev. Lett. **112**, 106602.
Rojas-Sánchez, J.-C. , *et al.*, 2013, Phys. Rev. B **88**, 064403.
Roth, A., C. Brüne, H. Buhmann, L. W. Molenkamp, J. Maciejko, X.-L. Qi, and S.-C. Zhang, 2009, Science **325**, 294.
Ryu, K.-S., L. Thomas, S.-H. Yang, and S. Parkin, 2013, Nat. Nanotechnol. **8**, 527.
Saitoh, E., and K. Ando, 2012, *Spin Current*, edited by S. Maekawa, S. O. Valenzuela, E. Saitoh, and T. Kimura (Oxford University, New York).
Saitoh, E., M. Ueda, H. Miyajima, and G. Tatara, 2006, Appl. Phys. Lett. **88**, 182509.
Schliemann, J., 2006, Int. J. Mod. Phys. B **20**, 1015.
Schmidt, G., D. Ferrand, L. W. Molenkamp, A. Filip, and B. van Wees, 2000, Phys. Rev. B **62**, R4790.
Seki, T., Y. Hasegawa, S. Mitani, S. Takahashi, H. Imamura, S. Maekawa, J. Nitta, and K. Takanashi, 2008, Nat. Mater. **7**, 125.
Seki, T., I. Sugai, Y. Hasegawa, S. Mitani, and K. Takanashi, 2010, Solid State Commun. **150**, 496.
Shchelushkin, R., and A. Brataas, 2005, Phys. Rev. B **72**, 073110.
Shull, C., C. Chase, and F. Myers, 1943, Phys. Rev. **63**, 29.
Shytov, A., E. Mishchenko, H.-A. Engel, and B. I. Halperin, 2006, Phys. Rev. B **73**, 075316.
Sih, V., W. Lau, S. Mährlein, V. Horowitz, A. C. Gossard, and D. D. Awschalom, 2006, Phys. Rev. Lett. **97**, 096605.
Sih, V., R. C. Myers, Y. K. Kato, W. H. Lau, A. C. Gossard, and D. D. Awschalom, 2005, Nat. Phys. **1**, 31.
Silov, A. Y., P. A. Blajnov, J. H. Wolter, R. Hey, K. H. Ploog, and N. S. Averkiev, 2004, Appl. Phys. Lett. **85**, 5929.
Silsbee, R., 1980, Bull. Magn. Reson. **2**, 284.

Sinitsyn, N. A., 2008, J. Phys. Condens. Matter **20**, 023201.
Sinitsyn, N. A., A. H. MacDonald, T. Jungwirth, V. K. Dugaev, and J. Sinova, 2007, Phys. Rev. B **75**, 045315.
Sinova, J., D. Culcer, Q. Niu, N. A. Sinitsyn, T. Jungwirth, and A. H. MacDonald, 2004, Phys. Rev. Lett. **92**, 126603.
Sinova, J., and A. H. MacDonald, 2008, in *Spintronics*, Semiconductors and Semimetals Vol. 82, edited by T. Dietl, D. D. Awschalom, M. Kaminska, and H. Ohno (Elsevier, New York), pp. 1–522 [http://www.sciencedirect.com/science/bookseries/00808784/82].
Sinova, J., S. Murakami, S.-Q. Shen, and M.-S. Choi, 2006, Solid State Commun. **138**, 214.
Skinner, T. D., K. Olejnik, L. K. Cunningham, H. Kurebayashi, R. P. Campion, B. L. Gallagher, T. Jungwirth, and A. J. Ferguson, 2015, Nat. Commun. **6**, 6730.
Smit, J., 1955, Physica (Utrecht) **21**, 877.
Smit, J., 1958, Physica (Utrecht) **24**, 39.
Stern, N., S. Ghosh, G. Xiang, M. Zhu, N. Samarth, and D. D. Awschalom, 2006, Phys. Rev. Lett. **97**, 126603.
Stern, N. P., D. W. Steuerman, S. Mack, A. C. Gossard, and D. D. Awschalom, 2007, Appl. Phys. Lett. **91**, 062109.
Stern, N. P., D. W. Steuerman, S. Mack, A. C. Gossard, and D. D. Awschalom, 2008, Nat. Phys. **4**, 843.
Streda, P., 1982, J. Phys. C **15**, L717.
Sugai, I., S. Mitani, and K. Takanashi, 2010, IEEE Trans. Magn. **46**, 2559.
Sundaram, G., and Q. Niu, 1999, Phys. Rev. B **59**, 14915.
Suzuki, T., S. Fukami, N. Ishiwata, M. Yamanouchi, S. Ikeda, N. Kasai, and H. Ohno, 2011, Appl. Phys. Lett. **98**, 142505.
Tanaka, T., H. Kontani, M. Naito, T. Naito, D. Hirashima, K. Yamada, and J. Inoue, 2008, Phys. Rev. B **77**, 165117.
Tse, W.-K., and S. Das Sarma, 2006, Phys. Rev. B **74**, 245309.
Tserkovnyak, Y., A. Brataas, and G. E. W. Bauer, 2002a, Phys. Rev. Lett. **88**, 117601.
Tserkovnyak, Y., A. Brataas, and G. E. W. Bauer, 2002b, Phys. Rev. B **66**, 224403.
Tserkovnyak, Y., A. Brataas, and B. I. Halperin, 2005, Rev. Mod. Phys. **77**, 1375.
Uchida, K., S. Takahashi, K. Harii, J. Ieda, W. Koshibae, K. Ando, S. Maekawa, and E. Saitoh, 2008, Nature (London) **455**, 778.
Uchida, K., *et al.*, 2010, Nat. Mater. **9**, 894.
Uhlenbeck, G. E., and S. Goudsmit, 1925, Naturwissenschaften **13**, 953.
Urban, R., G. Woltersdorf, and B. Heinrich, 2001, Phys. Rev. Lett. **87**, 217204.
Valenzuela, S. O., and T. Kimura, 2012, in *Spin Current* (Oxford University Press, New York), pp. 227–243.
Valenzuela, S. O., and M. Tinkham, 2006, Nature (London) **442**, 176.
Valenzuela, S. O., and M. Tinkham, 2007, J. Appl. Phys. **101**, 09B103.
Vignale, G., 2010, J. Supercond. Novel Magn. **23**, 3.
Vila, L., T. Kimura, and Y. Otani, 2007, Phys. Rev. Lett. **99**, 226604.
Vlaminck, V., J. E. Pearson, S. D. Bader, and A. Hoffmann, 2013, Phys. Rev. B **88**, 064414.
Vlietstra, N., J. Shan, V. Castel, B. J. van Wees, and J. Ben Youssef, 2013, Phys. Rev. B **87**, 184421.
Wadley, P., *et al.*, 2015, arXiv:1503.03765v1.
Wang, X., G. E. W. Bauer, B. J. Van Wees, A. Brataas, and Y. Tserkovnyak, 2006, Phys. Rev. Lett. **97**, 216602.
Wang, X., and A. Manchon, 2012, Phys. Rev. Lett. **108**, 117201.
Wang, X., C. O. Pauyac, and A. Manchon, 2014, Phys. Rev. B **89**, 054405.
Watanabe, S., K. Ando, K. Kang, S. Mooser, Y. Vaynzof, H. Kurebayashi, E. Saitoh, and H. Sirringhaus, 2014, Nat. Phys. **10**, 308.
Wei, D., Y. Niimi, B. Gu, T. Ziman, S. Maekawa, and Y. Otani, 2012, Nat. Commun. **3**, 1058.
Wei, D., M. Obstbaum, M. Ribow, C. H. Back, and G. Woltersdorf, 2014, Nat. Commun. **5**, 3768.
Weiler, M., J. M. Shaw, H. T. Nembach, and T. J. Silva, 2014, Phys. Rev. Lett. **113**, 157204.
Weiler, M., *et al.*, 2012, Phys. Rev. Lett. **108**, 106602.
Weischenberg, J., F. Freimuth, J. Sinova, S. Blügel, and Y. Mokrousov, 2011, Phys. Rev. Lett. **107**, 106601.
Werake, L., B. Ruzicka, and H. Zhao, 2011, Phys. Rev. Lett. **106**, 107205.
Wolf, S. A., D. D. Awschalom, R. A. Buhrman, J. M. Daughton, S. von Molnár, M. L. Roukes, A. Y. Chtchelkanova, and D. M. Treger, 2001, Science **294**, 1488.
Wunderlich, J., A. Irvine, J. Sinova, B. G. Park, L. P. Zârbo, X. L. Xu, B. Kaestner, V. Novák, and T. Jungwirth, 2009, Nat. Phys. **5**, 675.
Wunderlich, J., B. Kaestner, J. Sinova, and T. Jungwirth, 2004, cond-mat/0410295.
Wunderlich, J., B. Kaestner, J. Sinova, and T. Jungwirth, 2005, Phys. Rev. Lett. **94**, 047204.
Wunderlich, J., B.-G. Park, A. Irvine, L. P. Zârbo, E. Rozkotová, P. Nemec, V. Novák, J. Sinova, and T. Jungwirth, 2010, Science **330**, 1801.
Xia, K., P. Kelly, G. E. W. Bauer, A. Brataas, and I. Turek, 2002, Phys. Rev. B **65**, 220401.
Xiao, J., G. E. W. Bauer, K. Uchida, E. Saitoh, and S. Maekawa, 2010, Phys. Rev. B **81**, 214418.
Xu, X., W. Yao, D. Xiao, and T. F. Heinz, 2014, Nat. Phys. **10**, 343.
Železný, J., H. Gao, K. Výborný, J. Zemen, J. Mašek, A. Manchon, J. Wunderlich, J. Sinova, and T. Jungwirth, 2014, Phys. Rev. Lett. **113**, 157201.
Zhang, S., 2000, Phys. Rev. Lett. **85**, 393.
Zhang, W., M. B. Jungfleisch, W. Jiang, J. E. Pearson, and A. Hoffmann, 2015, Appl. Phys. Lett. **117**, 17C727 [http://dx.doi.org/10.1063/1.4915479].
Zhang, W., M. B. Jungfleisch, W. Jiang, J. E. Pearson, A. Hoffmann, F. Freimuth, and Y. Mokrousov, 2014, Phys. Rev. Lett. **113**, 196602.
Zhang, W., V. Vlaminck, J. E. Pearson, R. Divan, S. D. Bader, and A. Hoffmann, 2013, Appl. Phys. Lett. **103**, 242414.
Zhao, H., E. Loren, H. van Driel, and A. Smirl, 2006, Phys. Rev. Lett. **96**, 246601.
Zimmermann, B., K. Chadova, K. Diemo, S. Bl, H. Ebert, and V. Dmitry, 2014, Phys. Rev. B **90**, 220403.
Zutic, I., J. Fabian, and S. D. Sarma, 2004, Rev. Mod. Phys. **76**, 323.
Zwierzycki, M., Y. Tserkovnyak, P. J. Kelly, A. Brataas, and G. E. W. Bauer, 2005, Phys. Rev. B **71**, 064420.